Voltage-Controlled Magnetic Anisotropy and Spin-Dependent Resonant Tunneling in Cr/Ultrathin-Fe/Oxide Quantum Wells

	Qingyi Xiang
year	2018
	Cr/Fe /
	(University of Tsukuba)
	2018
	12102 8809
URL	http://doi.org/10.15068/00153792

Voltage-Controlled Magnetic Anisotropy and Spin-Dependent Resonant Tunneling in Cr/Ultrathin-Fe/Oxide Quantum Wells

Qingyi Xiang

July 2018

Voltage-Controlled Magnetic Anisotropy and Spin-Dependent Resonant Tunneling in Cr/Ultrathin-Fe/Oxide Quantum Wells

Qingyi Xiang

Doctoral Program in Materials Science and Engineering

Submitted to the Graduate School of

Pure and Applied Sciences

in Partial Fulfillment of the Requirements

for the Degree of Doctor of Philosophy in

Engineering

at the

University of Tsukuba

Acknowledgement

Firstly, I would like to express my sincere gratitude to my supervisor, Prof. Seiji Mitani. When I was still a junior undergraduate student, his encouragement and guidance helped me to enroll the University of Tsukuba as a graduate student. For 5 years from the moment I arrived at Japan, his continuous kind teaching, support and guidance make me from a freshman who knows nothing about spintronics to a Ph.D. who can finish a thesis independent. His patience, motivation, knowledge and immense experience set up an example how an experimental physicist should be. Of courses, I also appreciate his funding support otherwise I couldn't finish those work in this thesis.

Besides, I would like to thank the rest of my thesis committee members: Prof. Kazuhiro Hono, Prof. Shinya Uji and Prof. Hideto Yanagihara, for their insightful comments and meaningful discussions. With this, the thesis could be more complete.

I would like also to thank to all my collaborators in Research Center for Magnetic and Spintronic Materials(CMSM) at National Institute for Materials Science(NIMS): Dr. Sukegawa, Dr. Kasai, Dr. Wen (now work in Tohoku University), Dr. Sakuraba, Dr. Takahashi, Dr. Miura, Dr. Belmoubarik, Dr. Almahadawi, Dr. Mandal, Dr. Masuda, Dr. Xu, and Dr. Scheike, and those in Tohoku University: Prof. Takanashi, Dr. Seki, and Dr. Kubota. I have no enough space to express my appreciation to each single thing but their kind help from various sides helped a lot during the Ph.D. pursuit.

I also thank my friends in the center: Dr. Hirayama (now work at Toho University), Mr. Iida, Dr. Li (now work at QST), Dr. Zhou and all the other members in our center.

Table of content

Chapter 1   Introduction

"spin", this word is old but also new. The old part comes from 900 year ago, to describe women making yarn. In 1764, the invent of "*Spinning Jenny*" claimed the start of *Industrial Revolution*. This is the first time the "*spin*" brought changes to our world. After the *Industrial Revolution*, the physic entered a new age with the developing a quantum mechanics. In 1925, the word "*spin*" was given a new meaning in physics: *Krnig* suggested *Pauli* to image the rotation of an electron about its own axis, the "*spin*", to explain the "two-valuedness" of an intrinsic electron quantum number in his "*exclusion principle*"[1]. *Pauli* disliked the idea of "*Spin*" since electron should not rotate, however the same year, *Uhlenbeck* and *Goudsmit* also hypothesized that the spin as an intrinsic property of the electron,[2] and in 1926 *Thomas* sealed the relativistic analysis based on this classic assumption: spinning electron.[3] From then, "*spin*", stated its journey in physics rather than just making yarn. Soon in 1928, *Dirac* successfully explained the "two-valuedness" in his relativistic quantum mechanics[4]: spin-1/2 particles. From then, the concept that the specific angular momentum of electrons, i.e. spin, has two components: $\pm\hbar/2$, which are also known as "spin-up" and "spin-down". The spin determined the magnetic properties of solid, e.g. when all the unpaired spins in solid pointing the same direction, it shows ferromagnetic.

However, at that moment, it was just an observation of the new intrinsic degree of freedom in electrons. No one knew how to utilize this new degree of freedom. Even in 1950s, IBM developed magnetic tape for their computer product, the utilization of spin is independent from the charge. Spin and charge, these two intrinsic degree of freedom in electron seems never want to play with each other, until 1988. This year is the birth year of "*spintronics*".

In 1988, *Grünberg* and *Fert* independently observed the electric resistance of thin metal multilayers greatly modified, up to 50%, by applying external magnetic field. This effect is called giant magnetoresistance, which is also well-known as GMR.[5,6] From then, scientist realized spin and charge do play with each other, and the researches to reveal how the spin affect on the conductance start to be a new subject, that is spintronics.

Since then, spintronics developed rapidly: observation of tunneling magnetoresistance(TMR) at room temperature,[7,8] prediction of spin transfer torque(STT)[9], commercialization of the first hard disk drives(HDDs) based on GMR, realization of STT switch[10], giant TMR at room temperature[11,12], commercialization of magnetic random access memory(MRAM) based on TMR, observation of spin-hall effect[13], spin seebeck effect[14], voltage-controlled magnetic anisotropy(VCMA)[15], large perpendicular anisotropy[16], spin-orbital torque(SOT)[17] switch and so on. The area of spintronics keeps exploring. Manipulating the most two fundamental properties of electrons, provides people infinity imagination for the future informatic society: high speed, high density, low power consumption and nonvolatile. In this section, a general introduction of spintronics will be described from both physics and application sides.

1.1 Magnetoresistance

1.1.1 Giant magnetoresistance

Magnetoresistance (MR) was first observed by *the lord Kelvin* in 1857[18]. Now we know it is anisotropic magnetoresistance (AMR), where the electric resistance is determined by the angle between the direction of electric current and direction of magnetization. The underneath physics of AMR is the s-d scattering probability modified by spin-orbit interaction[19], and the ratio is normally several percent. However, AMR is not directly related to spin, especially the two states: "spin up" and "spin down". In 1936, Mott proposed the "two-current model" to explain the features of electric resistance near Currie temperature in ferromagnetic metals.[20] This model is based on the fact .that in the band structure of ferromagnetic metal, the energies split in to majority spin(spin up) and "minority spin"(spin down) in density of states(DOS). Thus, the electrons at the Fermi level exhibits different conductive properties due to the different states: up or down. In this model, the conductance is combination of a set of parallel channels, one is spin up to spin up and another is spin down to spin down. This simplistic model didn't attract too much interests, until 1966, *Fert* and *Campbell* did a series work on the two-current model in ferromagnetic metals, and sealed this idea, which became the basis of spintronics in the future.
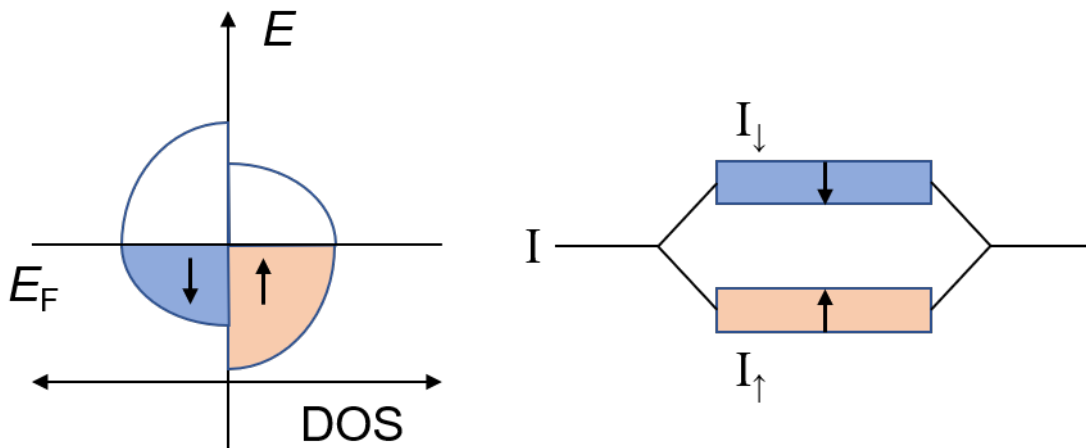
Figure 1.1 Typical DOS of a ferromagnetic materials and the corresponding two currents model.

In 1986, *Grünberg* et al found the antiferromagnetic interlayer exchange coupling(IEC) in Fe/Cr/Fe tri-layer structure, where magnetizations of two Fe layer aligned opposite to each other by the coupling exchange through Cr layer.[21] Following with this observation, In 1988, *Grünberg* found the MR in Fe/Cr/Fe is up to 1.5%, which was much larger than AMR in Fe single layer, as Figure 1.3.a shows.[6] The same year, *Fert* also found the Fe/Cr multilayer structure show large MR, exceeding 50% at low temperature and 17% at room temperature(Figure 1.2.b).[5] As Figure 1.3 shows, at zero field, due to the existence of antiferromagnetic IEC, the magnetizations of Fe layers were aliened antiparallel(AP). Thus, the passing electrons, no matter spin up or spin down, will be slowed down by the opposite magnetization due to the spin-dependent scattering, which leads to high resistivity. When the magnetic field applied, the magnetizations of Fe layers were aligned parallel(P), leading that half of the electrons passing freely, presenting as low resistivity.
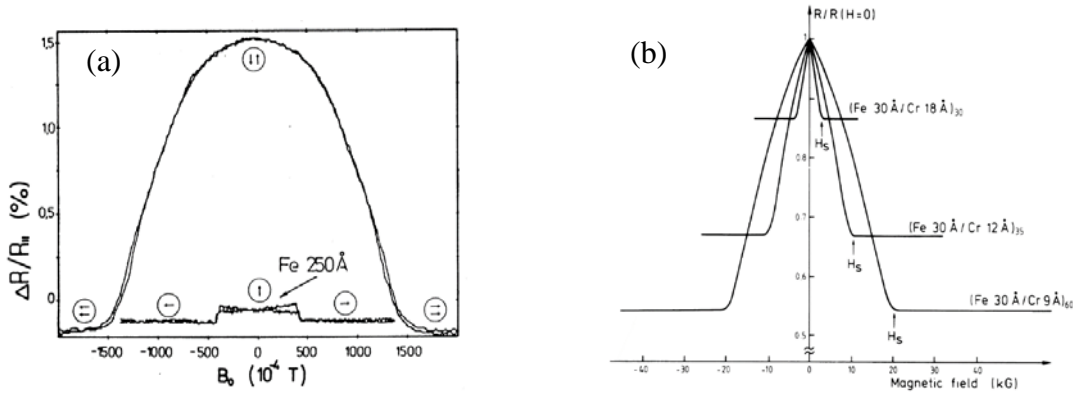
Figure 1.2 The first observation of giant magnetoresistance. (a) Reprinted with permission from [6] ©1989 by the American Physical Society. (b) . Reprinted with permission from [5] ©1988 by the American Physical Society.
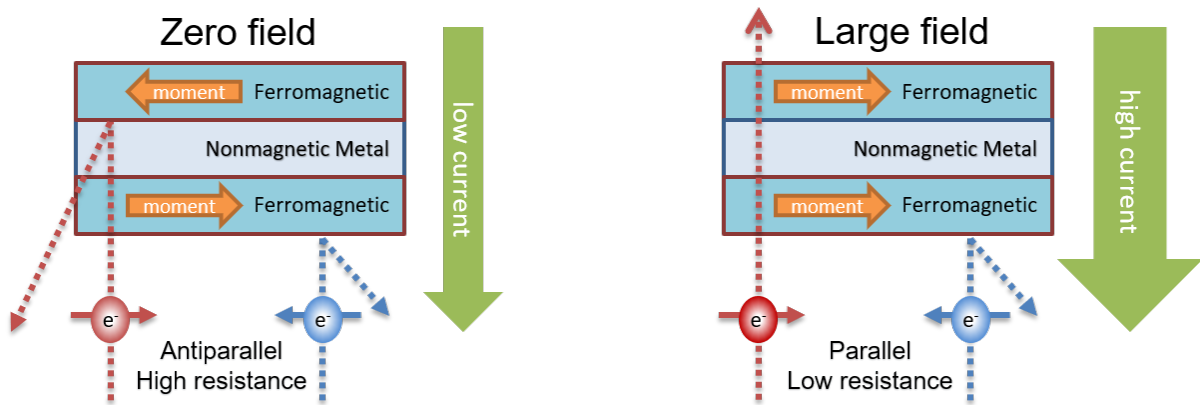
Figure 1.3 the concept of GMR.

Since then, the GMR became a very hot topic. In 1990, *Parkin* developed deposition technique of GMR multilayers by sputtering, with GMR found oscillated due to the oscillation of IEC on thickness of space layer .[22] And in 1991, the GMR ratio found in Co/Cu multilayers exceeded the value of 65%.[23]

However, it looked like difficult to utilize the GMR in applications at that moment, due to the realization of GMR is based on the antiferromagnetic IEC, where a large field was required to decouple the coupling. In fact, the GMR is arise from the antiparallel configuration instead of antiferromagnetic IEC itself. In 1991, the invention of spin valve[24] brought a bright future to applications based on GMR. In previous work, the antiparallel configuration was provided by the IEC. In spin valve, the antiparallel configuration is provided by a special designed tri-layer structure as figure x shows: magnetization of one of the ferromagnetic (FM) layer is pinned by the coupling with neighbor antiferromagnetic (AFM) layer, while the other ferromagnetic layer, spaced by a nonmagnetic(NM) layer, could be freely oriented by a small external field since it is soft magnet. The high sensitivity brought by soft ferromagnetic layer boosted the commercialization of HDD read head based on GMR effect. In 1997, IBM announced the first HDD with GMR head, and since then, the storage density increased rapidly.

Figure 1.4 (a) Typical spin valve using AFM to couple with FM. (b) **M-H** and MR for spin-valve structure, reprinted with permission from [24]. ©1991 by the American Physical Society.

1.1.2 Tunnel magnetoresistance

Inspired by the GMR, another important spin-dependent effect, re-entered the research society: tunnel magnetoresistance (TMR). The early observation of TMR in magnetic tunnel 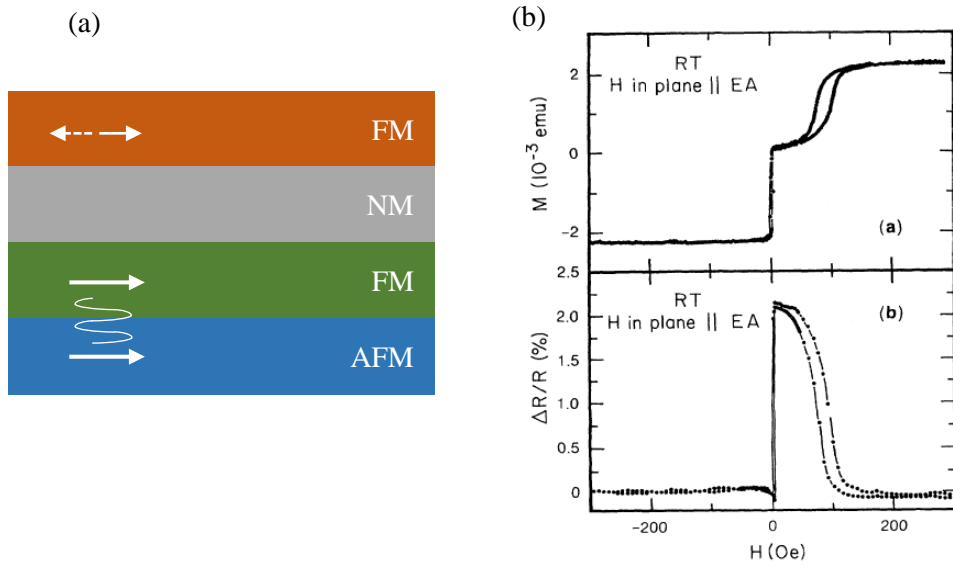junction(MTJ) was carried out by *Jullière* in 1975.[25] However, the TMR observed was very small and difficult to be reproduced. Though, a phenomenological model was proposed by *Jullière* which described the phenomenon by 2 assumptions: a. electron spin conserve during tunneling and b. the tunneling process, consisting of two independent channels, spin-up and -down, similar with "two-current model" in GMR mentioned above. To understand well about the TMR, it is better to understand the tunnel behavior of electrons first, as the basis of TMR.

The tunnel effect, more exactly, quantum mechanical tunnel effect, can be traced back to 1920s, as one of the "classic" quantum phenomena. In classic mechanics, it is impossible that particles can pass the insulating barrier, otherwise it cannot be called "barrier". However, in quantum mechanics, the tunnel effect is reasonable due to the "wave–particle duality". When the particles are regarded as wave, then, the tunnel effect can be simplified imaged as the incidence of electron wave to the barrier, where, some are reflected, and others are transmitted, if the potential barrier is thin enough, as Figure 1.6 shows in a metal/insulator/metal sandwich tri-layer. The population of transmitted electrons is determined by the tunnel probability (*T*), which can be described as follows in one dimensional free electron model:

$$T(E) \approx \exp\left(-2\int_0^t \sqrt{\frac{2m_e[U(x)-E]}{\hbar dx}}\right), \qquad\qquad 1.1$$

where *x* axis along perpendicular to the barrier interface, the *t* is thickness of barrier, *E* is the electron energy, m_e is the electron mass, and *U(x)* is the energy barrier. In a simpler description, $T \propto e^{-\kappa t}$, with κ the decay constant determined by [*U(x)* – *E*] reveals the tunnel effect dominated by electron side with the wave factor and barrier side with the decay constant.
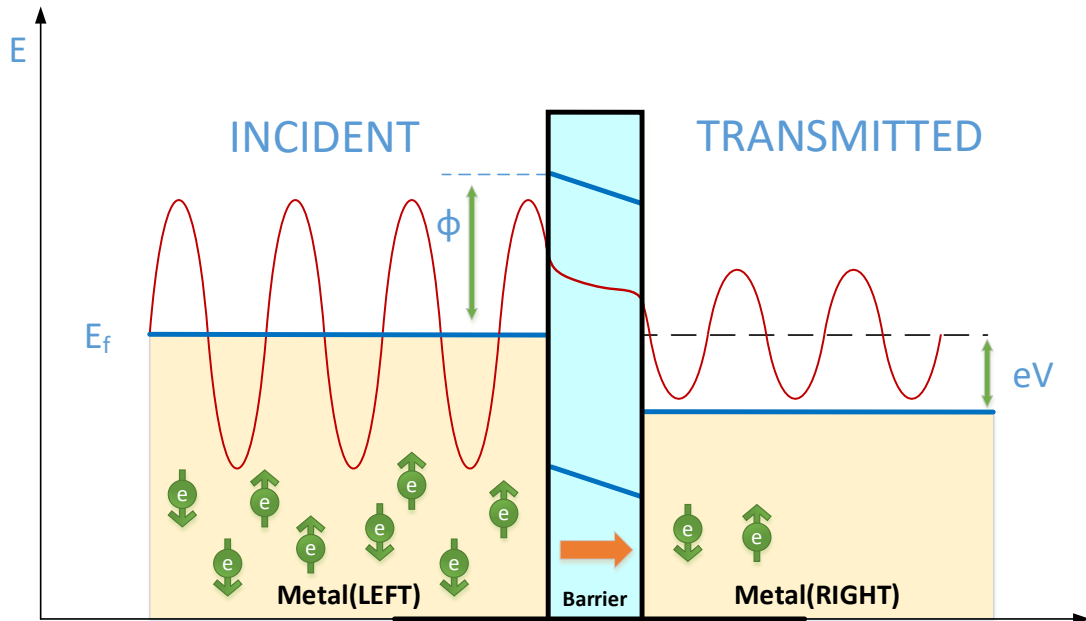

Figure 1.5 Typical wave function in a metal-oxide-metal junction, presenting how the quantum mechanical tunneling works of electrons. E_f is the Fermi energy, Φ is barrier height at interface between metal and oxide. When voltage applied, current will flow while with electrons density exponetial damping respect to the oxide thickness.

If there is no voltage difference between the metal layers, the Fermi levels should be same for the two side of the barrier, with the tunnel current equaling 0. However, once a suitable bias voltage V is applied, the Fermi level on the other side will be lowered and hence the electrons are able to tunnel in this structure.

Since the tunneling of the electrons, a current will appear and be proportional to the product of the occupied electron states at the left, and the empty states at the right side, and the transmission probability. So that, we can get the net tunneling current from left to right as:

$$I_{L \to R}(E) \propto N_L(E - ev)f(E - eV)T(E, V, \phi, t)N_R(E)[1 - f(E)] \tag{1.2}$$

Similarly, the current from right to left can be deduced and finally the total current could be written as:

$$I \propto \int_{-\infty}^{+\infty} N_L(E - ev)T(E, V, \phi, t)N_R(E)(E)[f(E - eV) - f(E)]dE \tag{1.3}$$

While, when the voltage $eV \ll \phi$, the only electrons contribute to the tunneling current are these close to the Fermi levels, E_F. And, the transmission and DOS factor will also independent to E, which reduces the current to:

$$I \propto N_L(E_F)T(\phi, t)N_R(E_F)\int_{-\infty}^{+\infty}[f(E - eV) - f(E)]\,dE \tag{1.4}$$

More ideally, if it is below a low enough temperature which make the $k_B T \ll eV$, the transparent expression for the tunnel conductance can be deduced as:

$$G \equiv dI/dV \propto N^L(E_F)T(\phi, t)N^R(E_F) \tag{1.5}$$

As mentioned in Figure 1.1, the DOS of electrons in ferromagnetic splits into spin-up and -down, thus the tunnel in FM/I/FM shows difference with in normal metal/insulator/metal case. As *Jullière* proposed, with the two assumptions mentioned, the tunnel behavior became a parallel circuit of two independent tunnel: spin-up tunnel and -down tunnel.
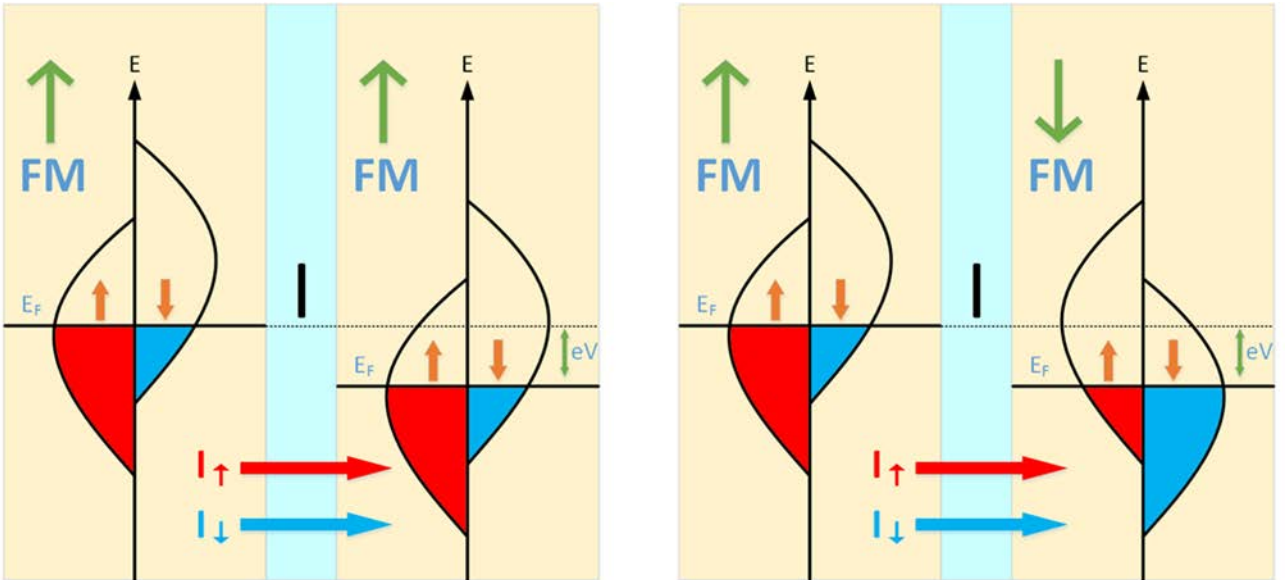
Figure 1.6 a) is parallel and b) is antiparallel configuration of the tunnel magentoresistance. The conductivitity is propotional ot he product of the DOS factors at the Fermi level. For parallel configuration, current is proportional to $N_+^2(E_f) + N_-^2(E_f)$ and for antiparallel is $2N_+(E_f)N_-(E_f)$.

As Figure 1.7 shows, when two magnetizations of FM are parallel aligned, then electrons tunnel from spin-up to spin-up and spin-down to spin-down, however, when two magnetizations of FM are antiparallel aligned, the spin-up and spin-down in one of the FM layers is reversed. Considering the current is determined

by the population of occupied electrons in the left FM and unoccupied electrons, for simplicity, also assuming that $N^L_{+(-)} = N^R_{+(-)}$, then Equation 1.5 can be written into:

$$G_P = G_\uparrow + G_\downarrow = N^L_+(E_F)T(\phi,t)N^L_+(E_F) + N^R_-(E_F)T(\phi,t)N^R_-(E_F)$$
$$\propto N^2_+(E_f) + N^2_-(E_f)$$

1.6

Where N_+ and N_- are the density of dates at E_F for majority and minority spin bands, respectively.

Similarly, when the spin orientation is antiparallel, the population of majority and minority of one of the layer is reversed, which leads to $N^L_{+(-)} = N^R_{-(+)}$, then the conductance should be like:

$$G_{AP} = G_\uparrow + G_\downarrow = N^L_+(E_F)T(\phi,t)N^L_-(E_F) + N^R_-(E_F)T(\phi,t)N^R_+(E_F)$$
$$\propto 2N_+(E_f)N_-(E_f)$$

1.7

It's obvious that the conductance is different and $G_P \geq G_{AP}$. Thus, when the magnetization configuration is manipulated, then resistance of the junction is varied and called as tunnel magnetoresistance, defined as:

$$TMR = \frac{G_P - G_{AP}}{G_{AP}} = \frac{R_{AP} - R_P}{R_P}$$

1.8

When put the population of the electrons into the TMR definition, then we have:

$$TMR = \frac{[N_+(E_f) - N_-(E_f)]^2}{2N_+(E_f)N_-(E_f)}$$

1.9

And if we define the effective tunneling spin polarization of each electrode as:

$$P = \frac{N_+(E_f) - N_-(E_f)}{N_+(E_f) + N_-(E_f)}$$

1.10

We can generalize Equation 1.9 into the famous Jullière-formula for the magnetoresistance of MTJ:

$$TMR = \frac{2P_L P_R}{1 - P_L P_R}$$

1.11

However, even this *classic* definition works well for long time, when we really considering the DOS at the interface, where, we thought the *numbers of majority or minority electrons* are determined by DOS then induced different resistance, one may find the minority is much larger than majority in Fe, Co and Ni at Fermi level. It reveals that the DOS discussed above is not really the DOS of the ferromagnetic materials, but a "DOS" combined with the tunnel barrier properties, as "tunneling DOS". It is a complex analysis to understand the TMR behind the simple Jullière model, with coherent of electrons plays a key role.

1.1.3 Tunnel barriers

As mentioned above, the tunnel barrier is a key factor to understand the TMR. How the electrons really "tunnel" through the barrier combined with the electron population together determined the TMR in a junction. To understand that, it is an effective way to start from the first observed TMR at room temperature in an Al_2O_3 based MTJ.

1.1.3.1 Amorphous AlO_x

As mentioned, for Fe, Co and Ni, minority actually dominated at Fermi level. These features will lead to a negative spin polarization, however, being contradicted with the experimental observation through spin-polarized tunneling technique (SPT), where most of the materials show the spin-polarization in the range of 40-60% with Al_2O_3 insulator.[26] Thus, the tunneling process is not simply from band structure of the electrode, but also the transmission probability, which depends on the evanescent states in the insulator []. The Fe, Co and Ni, has minority dominated at Fermi level (so called "d-electrons"), contributing to most of the magnetic moments, while the majority("s-electrons") relatively little. However, when considering the tunneling process, it is not simply following majority domination rule. Actually, the dominating d electrons quickly decays in the insulator because of a large effective mass while s electrons not.

However, after the first observation of TMR by *Jullière*, there are almost 20 years until *Miyazaki et al.* [27] observed it at room temperature. They deposited Ni-Fe/Al-Al_2O_3/Co junction via electron beam evaporation. And with optimized annealing procedures, they finally find a 2.7% TMR ratio at room temperature, as Figure 1.8[27] shows. And soon *Miyazaki*[28] and *Moodera*[8] developed the Fe/Al_2O_3/Fe MTJs with the TMR value over 10% at room temperature. In 2004, *Wang*[29] developed AlO_x based MTJ using CoFeB as free and reference layers and got a 70% TMR ratio at room temperature, and this is also the highest room temperature TMR using AlO_x as tunnel barrier.

However, it is highly required to perform a critical oxidation on Al layer to produce a tunnel barrier. Under or over oxidation usually leads to a significant decrease of TMR ratio. And due to the fact that the AlO_x is armouphous, the tunneling though it is incoherent. Since there is no crystallographic symetry in the armouphous barrier, the Block states with didifferent symmetries of wave functions existing in the 3d FM electodes will couple with evanescent states in the tunneling barrier, and make the tunneling probabilities weakened.
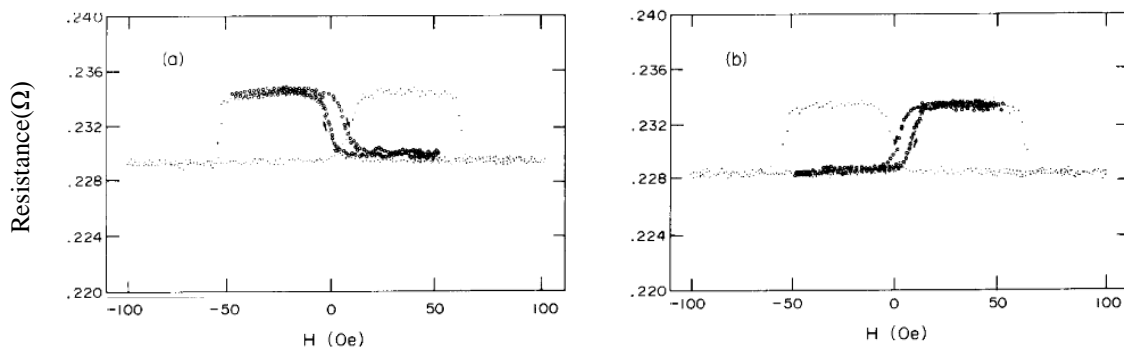

Figure 1.7 The first observation of room temperature TMR effect based on AlO_x. Reprinted with permission from [27] ©1992 Elsevier.

1.1.3.2 Crystal MgO

Unlike amorphous AlO_x based tunnel barrier, the MgO based MTJs requires a well-matched crystalline orientation of the ferromagnetic electrodes to get a high TMR ratio. Owing to the good crystalline, the tunneling process become coherent rather than incoherent in amorphous AlO_x. The coherent tunneling property significant enhanced the TMR ratio.

The underneath physics behind the coherent and incoherent tunneling is the symmetry selection rules in the tunneling process. As Figure 1.10 shows, the electrons have different symmetries of the Bloch wave function regarding with the direction perpendicular to the transport, and normally we considering about Δ_1 Δ_2 and Δ_5 in the tunneling process. In 2001, *Butler et al* reported the theoretical calculation of tunneling behavior based on the crystal MgO barrier[30], as Figure 1.11 shows. In the calculation, the different decay rates of Bloch states are taken into consideration and consequently, the barrier layer acts as a symmetry filter. For crystal MgO, it is revealed Δ_1 symmetry has a much slower decay rate, which leading to the barrier only "allowing" Δ_1 to pass through the barrier, and this is the fundamental reason that crystal MgO exhibiting such giant TMR when combined with Fe electrode
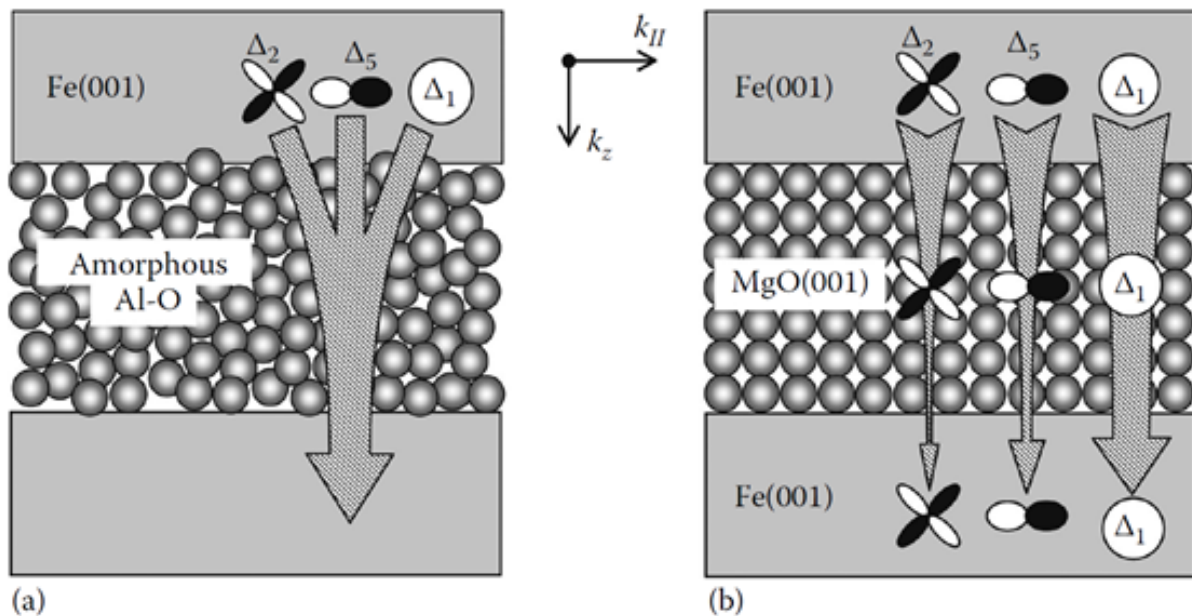

Figure 1.8 a) incoherent and b) coherent tunneling in amorphous AlO_x and crystal MgO. Reprinted from [26] ©2012, with permission from Taylor and Francis.
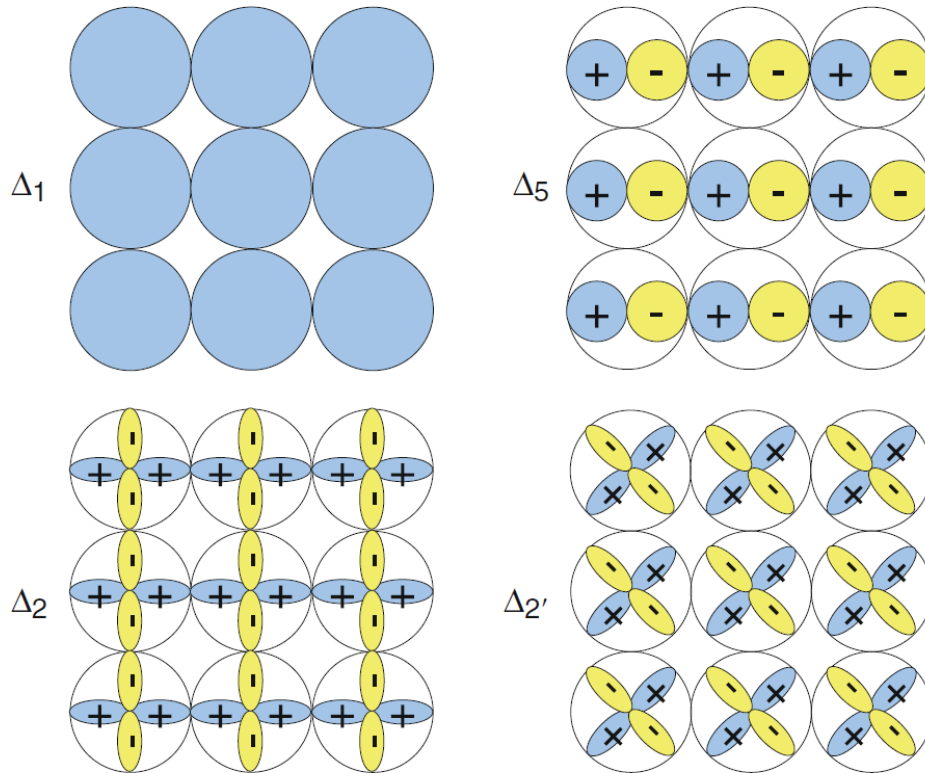
Figure 1.9 Symmetries of wave functions of a two-dimensional square lattice, reprinted from [31] ©2016, with permission from Springer Nature.
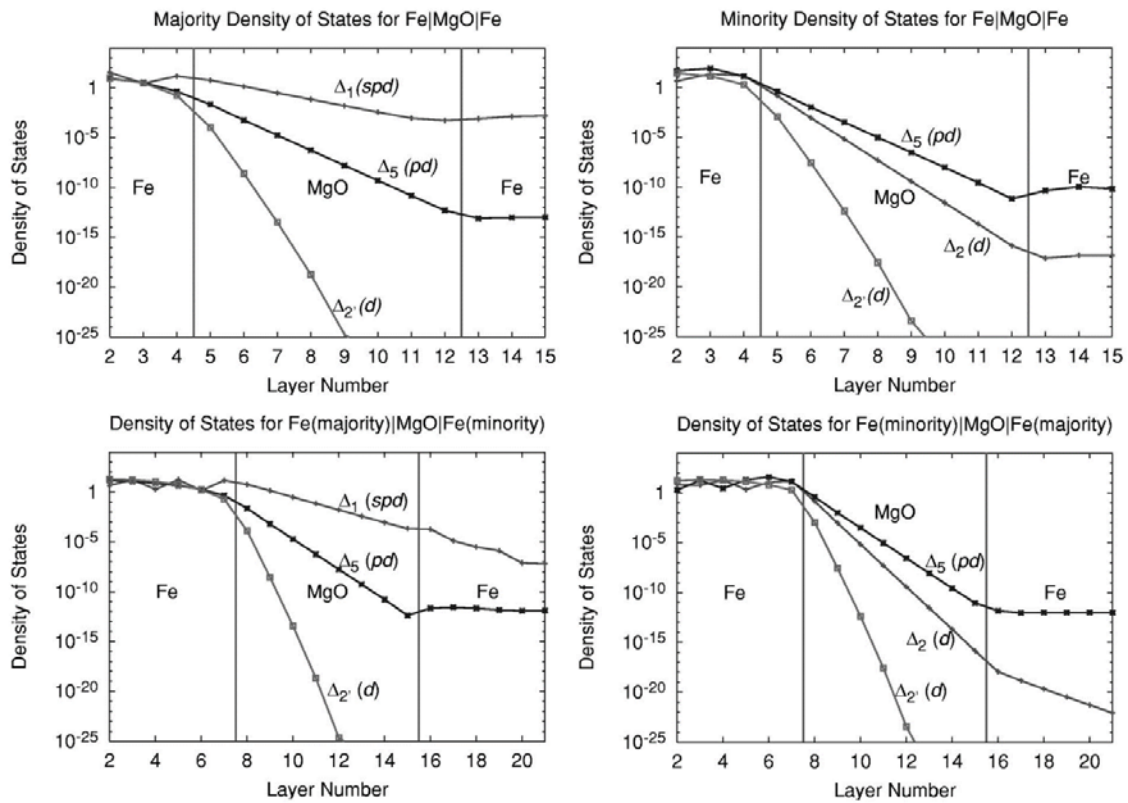

Figure 1.10 DOS of Fe/MgO/Fe at four different magnetization configurations. Reprinted with permission from [30]. ©2001 by the American Physical Society.
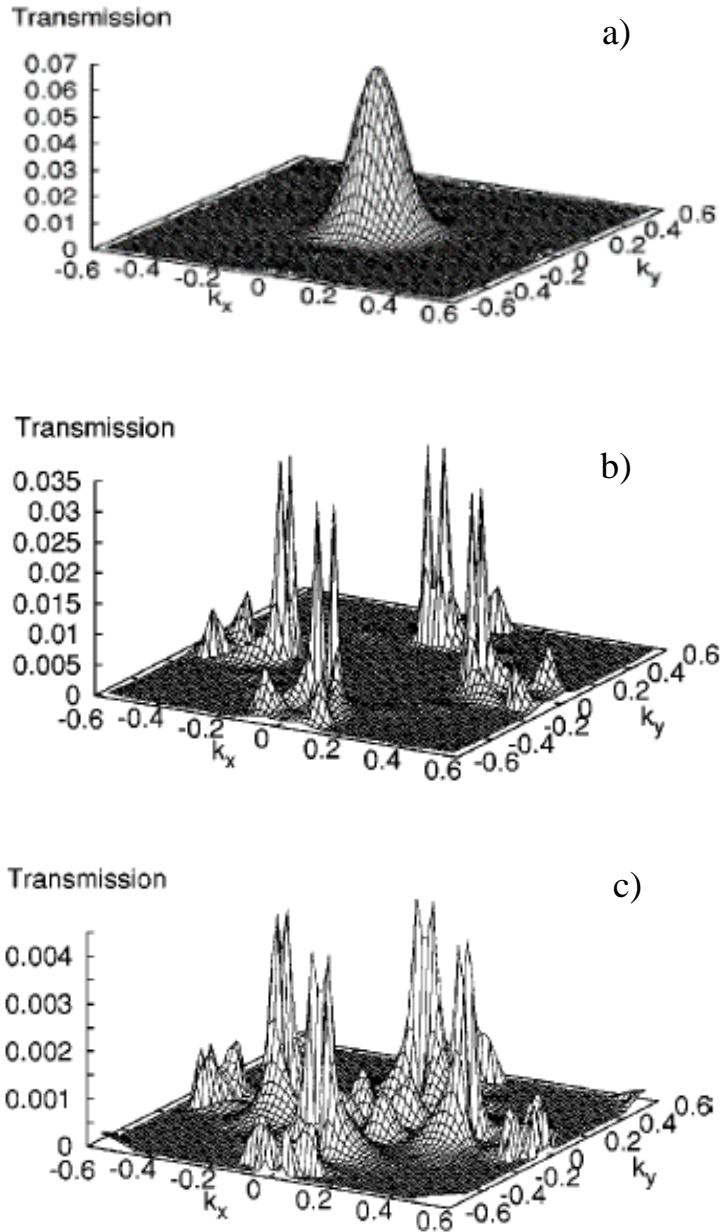
Figure 1.11 conductance for a) majority b) minority and c) anti-parallel states of a 4-layer MgO. Reprinted with permission from [30]. ©2001 by the American Physical Society.

In 2004. *Yuasa et al* reported the giant room-temperature magnetoresistance in single-crystal Fe/MgO/Fe magnetic tunnel junctions. [11] The TMR reaches 180% and it is believed coherency of the electron wave functions is conserved across the tunnel barrier. Figure 1.8 (a) is the TEM image of the fully epitaxial Fe/MgO/Fe junction and Figure 1.8 (b) is the MR ratio.[11]

a)

b)

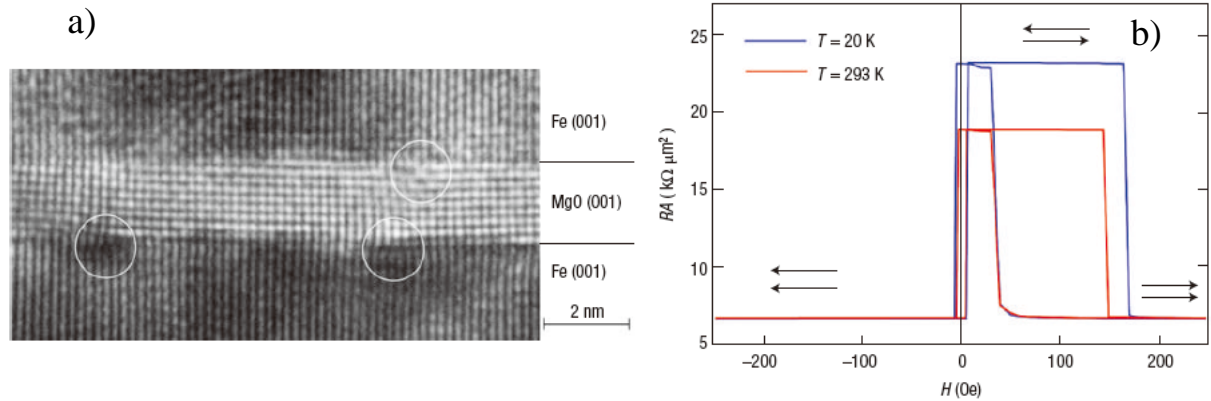Figure 1.12 a) is a TME iamge of Fe/MgO/Fe junction and b) is room temperature MR curves. Reprinted from [11] ©2004, with permission from Springer Nature.

However, the requirement of the single crystal texture of the electrode limited application of the Fe/MgO based MTJs. Instead of single crystal Fe/MgO, *Djayaprawira et al* find a promising solution that even using conventional sputtering one can get well textured tunnel barrier layer. [32] When $(CoFe)_{80}B_{20}$ is used, the CoFeB layer is amorphous while the thin MgO layer, can easily form into (001) texture. Then post annealing this stack multilayer can improve the crystallization of the two CoFeB layer form the MgO interface Figure 1.14[32].Hence, the final junction can maintain well crystallized CoFeB at the barrier interface which bring out a very high TMR ratio.[33]
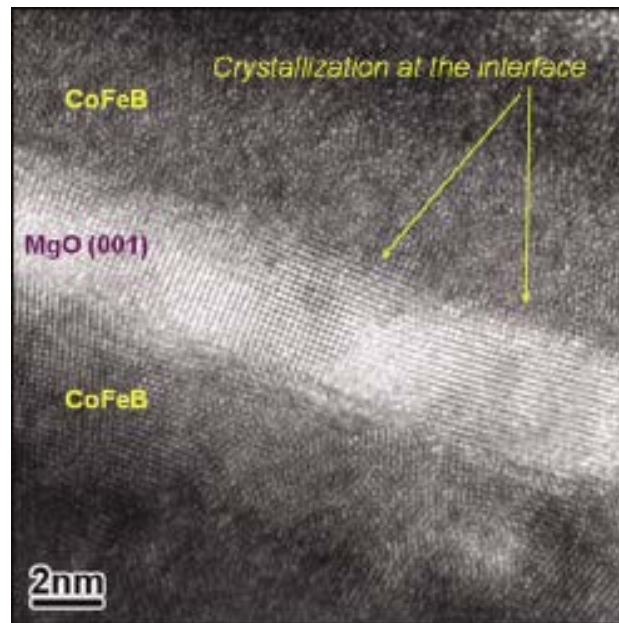
Figure 1.13 crystallization at the CoFeB/MgO interface. Reproduced from [32], with the permission of AIP Publishing.

1.1.3.3 Spinel as barrier

Spinel materials, especially $MgAl_2O_4$ is a newly developed barrier material. It shares the similar band structure and the coherent tunneling property of crystal MgO.[34,35] However, compare with MgO, the $MgAl_2O_4$ has an improved lattice matching with the common ferromagnetic electrode materials.

Figure 1.15 shows the atomic structure of spinel $MgAl_2O_4$. The lattice constant is around 0.809 nm, considering the Oxygen positions, giving an effective lattice constant of $0.809/(2 \times \sqrt{2})$, which is almost perfectly matched with Fe based electrode, as Table 1-1 shows.
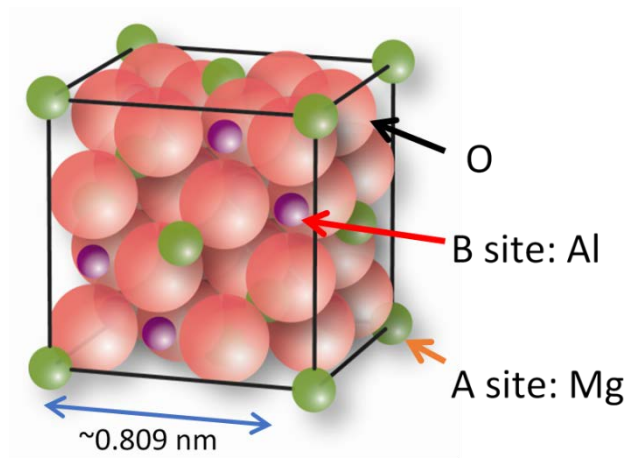

Figure 1.14 Structure of spinel $MgAl_2O_4$, courtesy of Dr. Sukegawa.

Table 1-1 Lattice comparison between $MgAl_2O_4$ and MgO with ferromagnetic electrode materials

Materials	a (nm)	Mismatch (%)	
		vs. **$MgAl_2O_4$**	vs. MgO
Fe	0.2866	**0.20**	−3.79
$Co_{50}Fe_{50}$	0.2851	**−0.32**	−4.30
$B2$-Co_2FeAl	0.573	**0.17**	−3.83
$D0_{22}$-MnGa	0.390	**−3.4**	−7.4

.

In 2009, *Sukegawa et al* established the demonstration of $MgAl_2O_4$-MTJs based on post-oxidation of MgAl alloy, where the lattice matching significantly enhanced the bias performance comparing with MgO barrier.[36] With technique improved, the TMR ratio of $MgAl_2O_4$ based MTJs is catching up with MgO based one as Figure 1.17 shows.

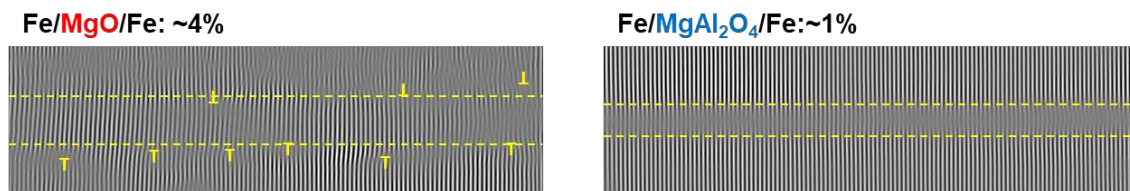Figure 1.15 comparison of lattice matching between MgO and $MgAl_2O_4$, courtesy of Dr. Sukegawa, to be published on Appl. Surf. Sci.
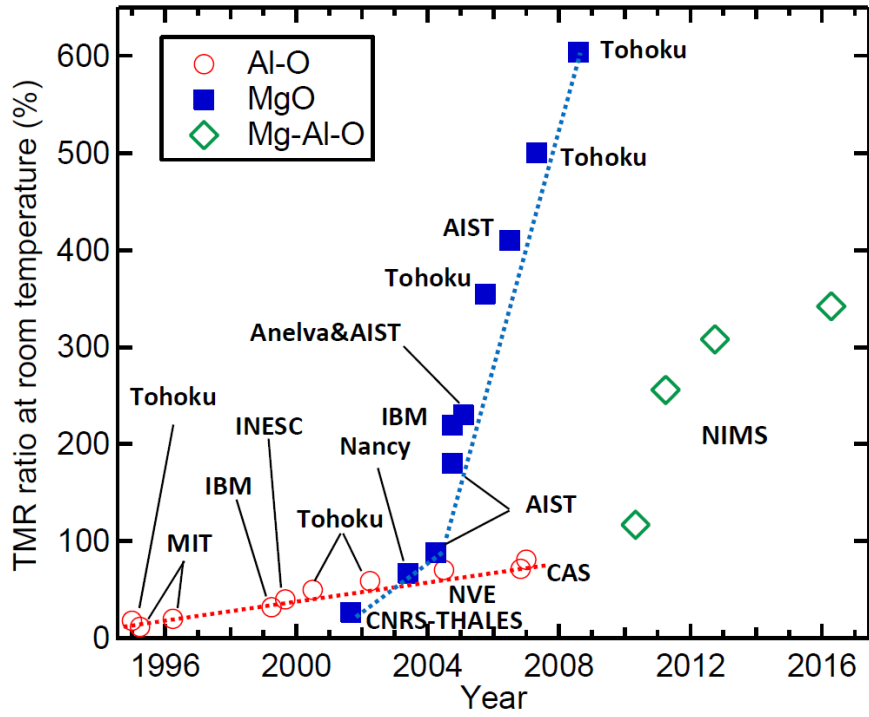
Figure 1.16 Increasing TMR in MgAl$_2$O$_4$ based MTJs, courtesy of Dr. Sukegawa.

1.1.4 Quantum well induced spin-dependent resonant tunnel effect

As mentioned above. The coherent tunnel observed in crystal MgO barrier based MTJs lead to a significant enhancement of TMR. Besides, the specific coherent property provides many possibilities to further modulation on the tunneling behavior. One of these trials is to form a quantum well(QW) in where electrons confident, with spin polarization. Generally, the approach to realize quantum confinement of spin polarized electrons is by making one ultra-thin ferromagnetic electrodes, being sandwiched with two barriers. To form a QW in MTJ, there are two major ways.

The first way is to make FM/I/ultrathin-FM/I/FM double barrier MTJ(DMTJ). It is the natural consideration if one wants to realize the spin dependent QWs. In 2006, *Nozaki et al* established Fe based DMTJs with Fe nano-islands in a thick MgO barrier, where they found the conductance oscillatory with the bias voltage, owing the resonant states created by QWs.[37] And in 2008, *Iovan et al* found a record TMR ratio over 1000% at low temperature in Fe/MgO/Fe/MgO/Au structures through point contact measurement.[38] However, no significant improvement of TMR has been observed at room temperature. And the growing of ultrathin electrode layer sandwiched by two oxide layers is not easy considering one have to deposit metal material on oxide material.
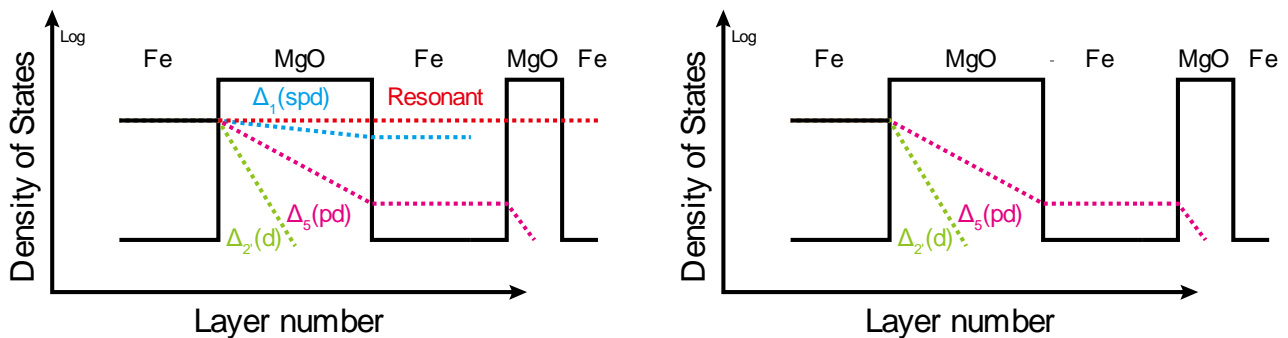

Figure 1.17 Potential profile for a typical Fe/MgO/Fe/MgO/Fe quantum well at P and AP states

Thus, another method aimed to overcome the growing difficulties of ultrathin FM layer between two barriers came out with the introduce of metallic "barrier". Owing to the coherent tunneling properties, one can consider the major contribution of tunneling from the majority electrons, i.e. $\Delta_1\uparrow$ electrons. Simply saying, in an MTJ, a metal layer can also work as barrier if there is no Δ_1 near the fermi level. And Cr is one of the best candidate since it has perfect lattice constant with Fe, and, no Δ_1 near fermi level as Figure 1.19 shows.[39]

A theoretical calculation is performed for the structure of Cr/Fe/MgO[40], where they do find a strong resonant states created due to the existence of QWs within the ultrathin-Fe layer as Figure 1.20 shows . With the assistance of the QW states, the spin-dependent resonant tunneling effect will dominate the transport, where the TMR ratio can easily over 1000% when the SDRT is switched on or off by applying different bias voltage.
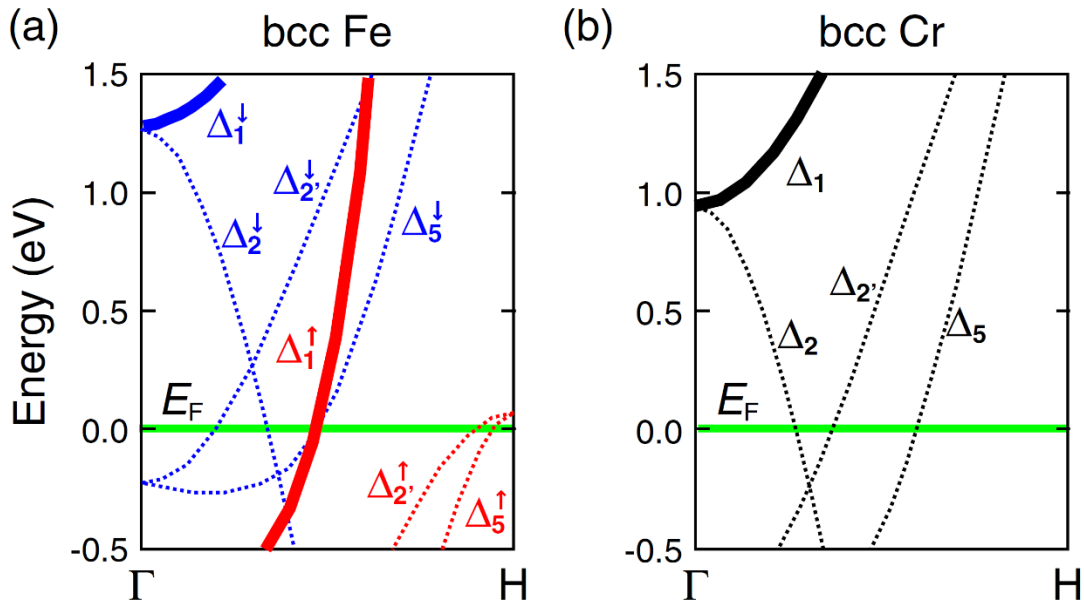
Figure 1.18 DOS of a) Fe and b) Cr. Reprinted with permission from [39]. ©2008 by the American Physical Society.
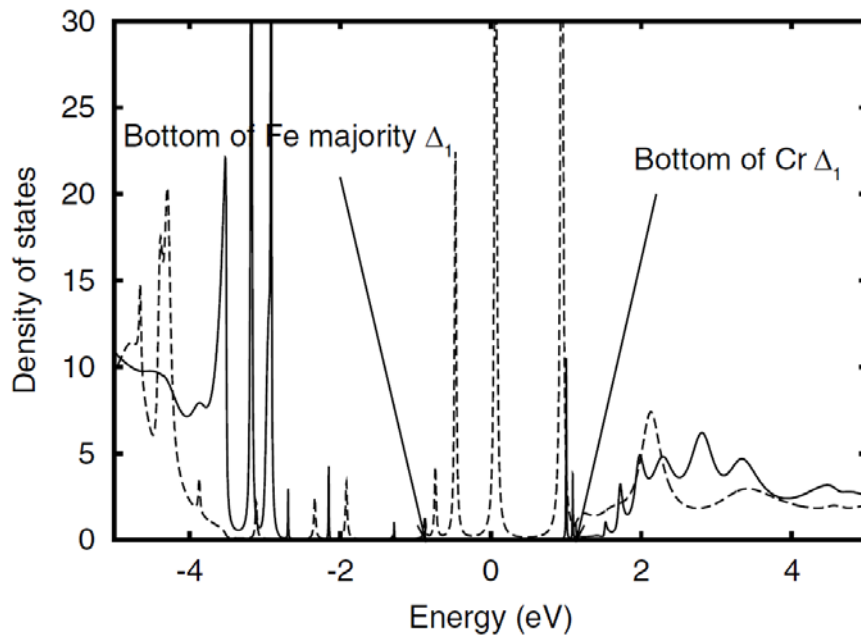
Figure 1.19 DOS of Cr/Fe/MgO with quantum well formed in Fe, Reprinted with permission from [40]. ©2005 by the American Physical Society.

In 2007, *Greullet et al* reported the observation of oscillated dI/dV in Cr spaced Fe/MgO/Fe MTJs, and a clearer oscillation in d^2I/dV^2.[41] Soon in 2008, *Niizeki et al* reported a clearer oscillation behavior in Cr/Fe/MgO/Fe MTJs. More interesting, the observed resonant peaks show periodic behavior with the QW width increased, as predicted in theoretical calculation.[40]
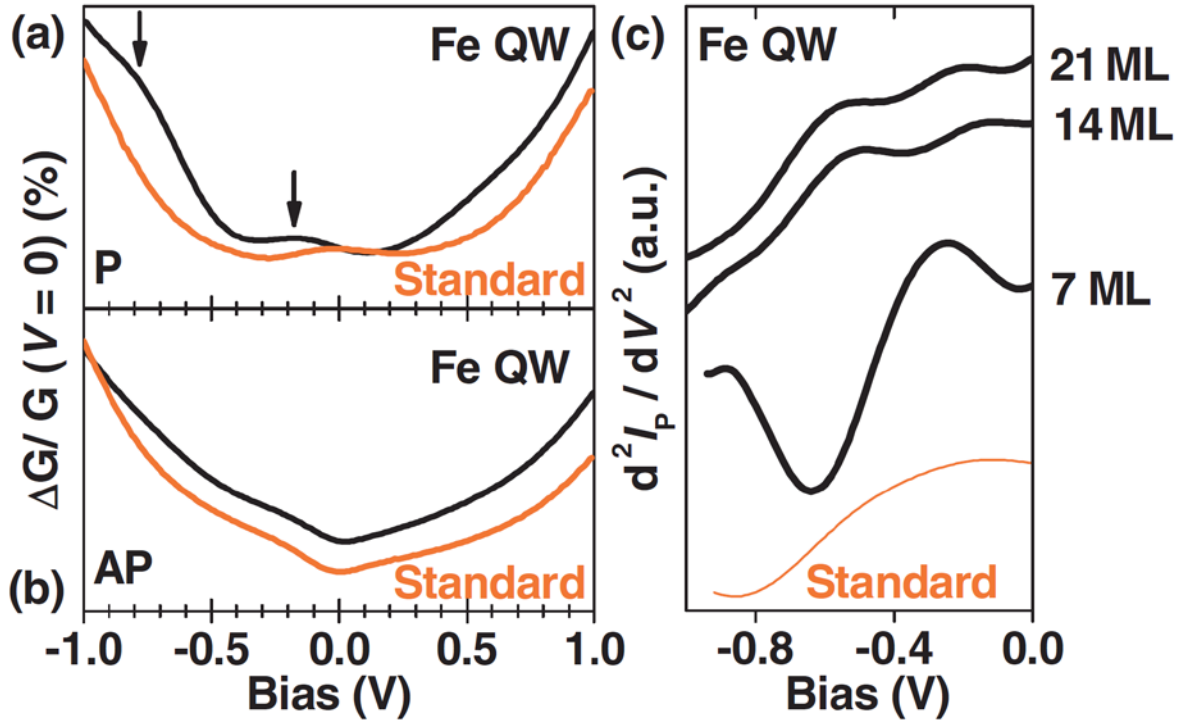
Figure 1.20 oscillation behavior of Cr spaced Fe/MgO/Fe MTJs. Reprinted with permission from [41]. ©2007 by the American Physical Society.

Here, the dI/dV spectrum is the major method to detect the existence of QWs. Since the DOS of the electrode is somehow reflected by the dI/dV spectrum. From the equation[42]:

$$\frac{dI}{dV} = \frac{2\pi e^2}{\hbar}|t|^2 D_1(E_F)D_2(E_F + eV)$$ 1.12

where $|t|^2$ is the tunnel probability, D_1 and D_2 is the DOS of two electrode besides the barrier, E_F is the fermi level and V is the voltage applied to electrode 2.
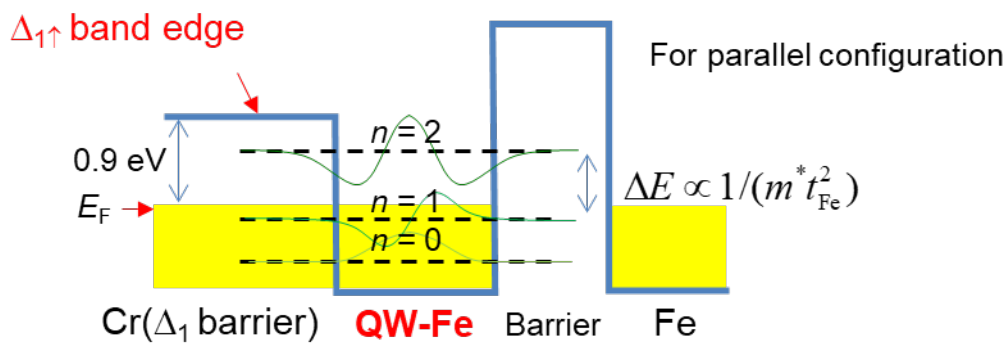
Figure 1.21 A typical potential profile for Cr/Fe/Oxide/Fe quantum well

Owing to this method, one can easily investigate the relationship between DOS and applied bias. Here, since the conductance is majorly contributed from Δ_1 electrons, one can easily observe how the Δ_1 electrons modulated by the QWs. *Sheng et al* performed detailed analysis of spin dependent resonant tunneling of Cr/Fe/MgO/Fe with continuous wedge Fe. A map of applied bias voltage, thickness of Fe, i.e. QW width, and conductance is plotted as Figure 1.24 shows. A clear periodic behavior can be observed which indicating the

quantum interference modulation characters of Δ_1 QWs.

Figure 1.22 peak positions from experiment and calculation. Reprinted with permission from [39]. ©2008 by the American Physical Society.
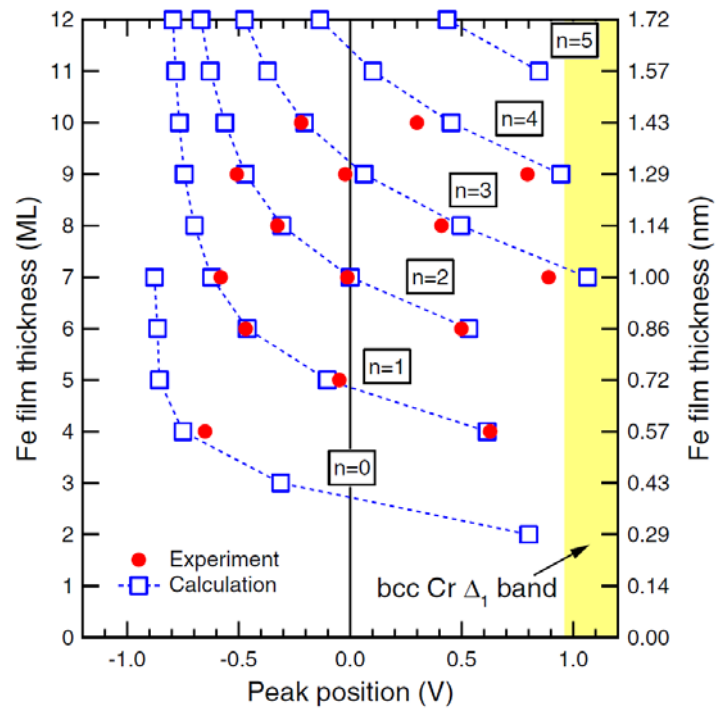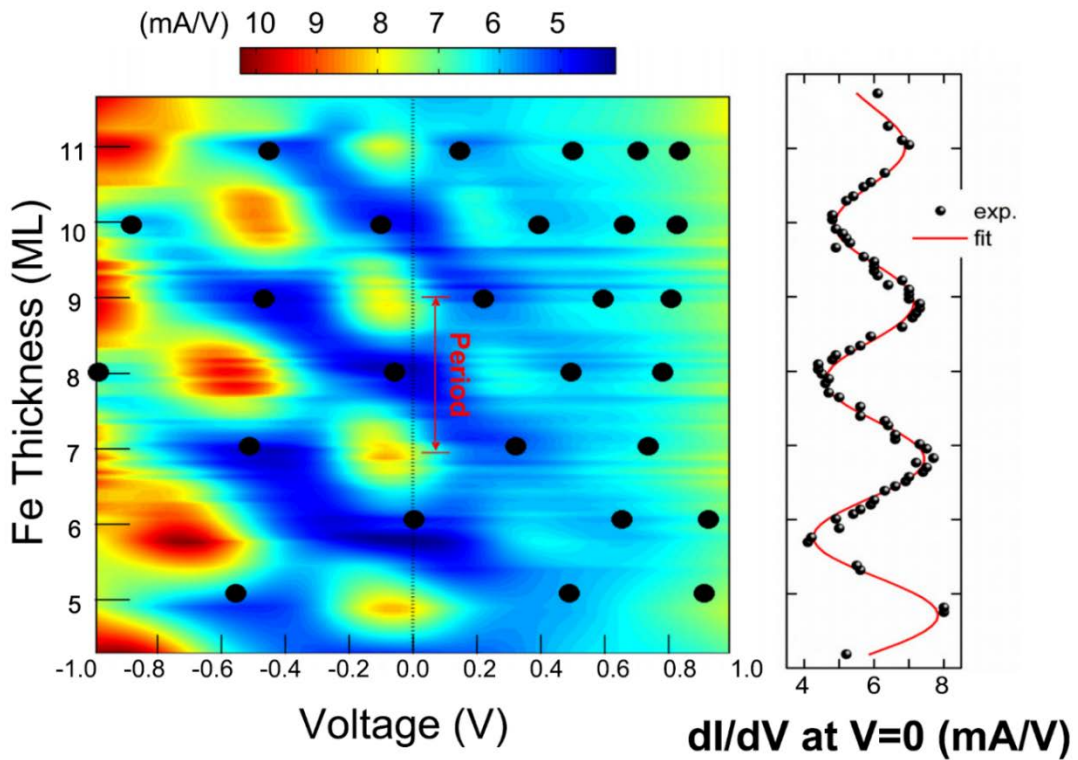

Figure 1.23 conductance map on applied voltage and Fe thickness. Reproduced from [43], with the permission of AIP Publishing.

18

1.2   Magnetic Anisotropy

Magnetic anisotropy is actually the first property of magnetic materials people utilized. Over 2000 years ago, the ancient Chinese people using a tool named as *Sinan* (meaning as "south-governor") to find the direction. This is actually the first magnetic compass, and the physics behind this interesting and useful tool revealing the anisotropy property of the magnetic materials: the *Sinan* favored to point to south.

Figure 1.24 A model of *Sinan*, the first magnetic compass invented by ancient Chinese.

In scientific description, the magnetic anisotropy is: the magnetic moment inside the ferromagnetic materials will tend to lie with one or some fixed directions called "easy axis", which the energy is much easier to transport when put the materials inside a field parallel with the "easy axis". In the case of *Sinan*, the easy axis is the direction of the spoon and the external filed is the earth's magnetic field.

The general description of magnetization to lie along an easy axis is as follow:

$$E_a = K_1 \sin^2 \theta \qquad\qquad 1.13$$

Where θ is the angle between magnetization and the anisotropy axis. Thus, rotating the magentic moment to parrallel to the exteran field can minimized the energy.

Nowadasy, the magenttic compas is just one of the applications of the magentic anisotropy, there are a lot of applications based on it no mater it is a strong magentic anistroy or a weak magentic anisotropy such as:

1) For strong magenetic anisotropy: permanent magent, electric motors, speakers, microphones, magnetic memories…
2) For weak magnetic anisotropy: transformers, electromagnets, electric motors, magnetic field sensors…

In this study, a brief introduction will give and then focus on the magnetic anisotropy in thin film and its application in magnetic memories.

1.2.1 Phenomemological description of magnetic anisotropy

As mentioned above, the states of the magentic moment are defined as *easy*, *hard* and intermediate between these two, as Figure 1.26[44] shows. The ground of the magnetic energy is defined when the magnetic moment is laying along *easy axis*, where the energy takes the minimum value. Thus, the total magnetic energy can be deduced applying the field (*H*) in *hard* axis as following:

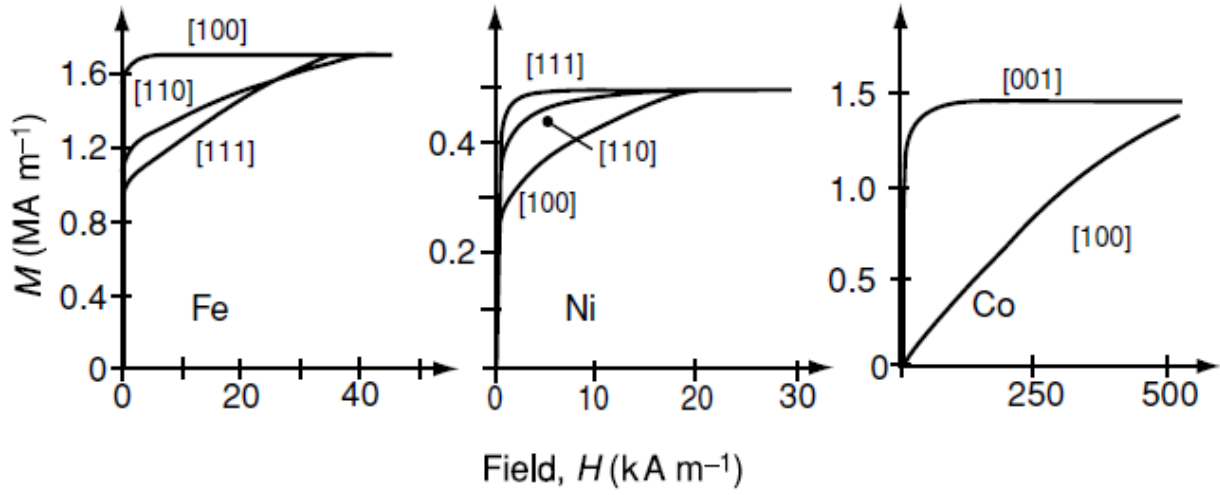$$E_{MA} = \mu_0 \int_0^{M_S} H(M)dM \qquad \text{1.14}$$

Figure 1.25 magnetization curves of single crystal Fe, Ni and Co under different external field direction respect to crystal direction. Reprintted from [44] ©2010, with permision from Cambridge Univerisity Press.

If the equation is applied to the magnetization curves in Figure 1.26, one can easily find that simply rotating the sample, different MA energies can be obtained. And the area between two curves, e.g. from [100] to [001] in Co case, is the magnetocrystalline anisotropy (MCA) energy density. That describes the fact that to saturate the Co sample, it is much harder from [100] direction while less energy is cost from [100] direction.

The MCA is a widely existed anisotropy in crystallized magnetic materials. As the name, this kind of MA is directly determined by the crystalline structure of the materials. Figure 1.27 shows the MCA energy surfaces for Fe, Co and Ni. And the different surfaces come from the different crystalline that Fe of bcc, Co of hcp and Ni of fcc.

In general, the conventional expressions for the anisotropy energy in different symmetries are:

Hexagonal: $\quad E_a = K_1 \sin^2\theta + K_2 \sin^4\theta + K_3 \sin^6\theta + K_3' \sin^6\theta \sin 6\phi$ $\qquad$ 1.15

Tetragonal: $\quad \begin{aligned} E_a = &K_1 \sin^2\theta + K_2 \sin^4\theta + K_2' \sin^4\theta \cos 4\phi + K_3' \sin^6\theta \\ &+ K_3' \sin^6\theta \sin 4\phi \end{aligned}$ $\qquad$ 1.16

Cubic $\quad E_a = K_{1c}(\alpha_1^2\alpha_2^2 + \alpha_2^2\alpha_3^2 + \alpha_3^2\alpha_1^2) + K_{2c}(\alpha_1^2\alpha_2^2\alpha_3^2)$ $\qquad$ 1.17

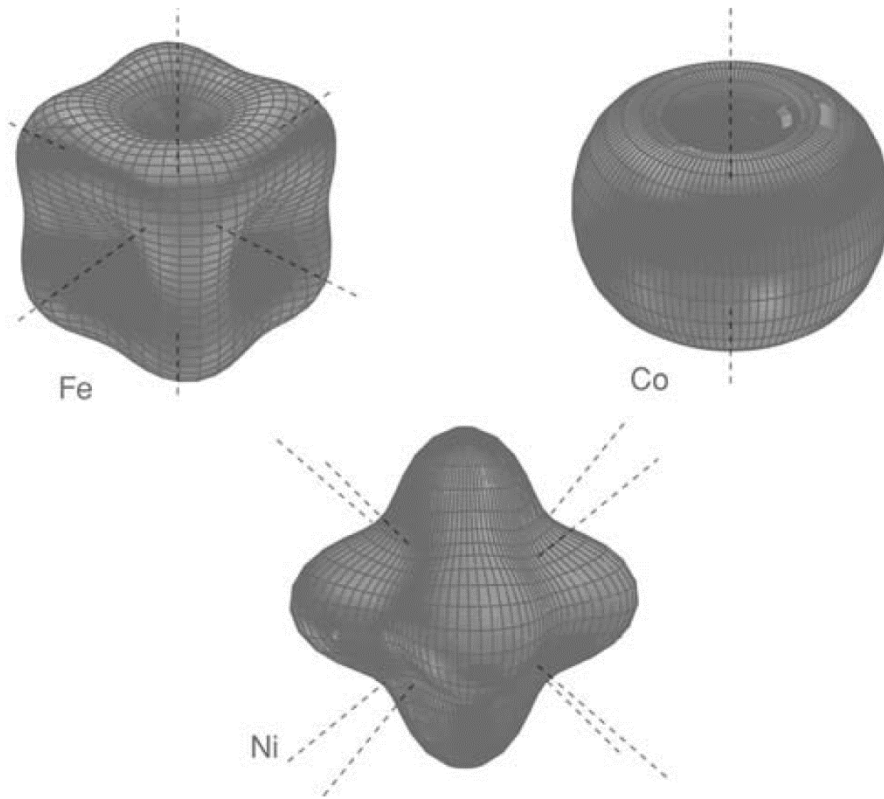where α_i are the direction cosines of the magnetization.

Figure 1.26 Magnetocrystalline anisotropy energy surfaces for Fe, Co and Ni. Fe has three easy axes along <100>, Ni has four easy axes along <111> and Co has one easy axis along [001]. Reprintted from [44] ©2010, with permision from Cambridge Univerisity Press.

The anisotropy field H_a is defined as the field where the magnetization reaches saturated along hard axis. The energy is:

$$E = K_u \sin^2 \theta - \mu_0 M_s H cos\left(\frac{\pi}{2} - \theta\right),$$ 1.18

minimizing E, with $\partial E / \partial \theta = 0$ and $\theta = \pi/2$, the solution is:

$$H_a = \frac{2K_u}{\mu_0 M_s}.$$ 1.19

This equation can also use to evaluate the MA energy density as:

$$K_u = \frac{\mu_0 H_a M_s}{2},$$ 1.20

which is commonly used to preliminarily determine the MA energy of samples by simple measure the value of H_a and M_s.

As the MCA is widely existing in crystallized ferromagnetic materials, there are two individual origins of it:

1) Single-ion contributions, which arise from electrostatic interaction of the orbitals contacting the magnetic electron with the potential created at the atomic site by the rest of the crystal;

2) Two-ion contributions, which arise from dipole-dipole interaction, such as energy difference from

broadside configuration and heat-to-tail configurations regarding to two dipoles.

The discussion above is intrinsic property considering an infinite extended crystal (or uniaxial sphered sample). However, other factors must be considering when the sample is a thin film.

The first one is the *shape anisotropy*. As the name, the *shape anisotropy* arises from the shape, which is an extrinsic factor derives from the demagnetizing field. The magnetostatic energy of a ferromagnetic ellipsoid with magnetization M_s is:

$$\varepsilon_m = \frac{1}{2}\mu_0 V \mathcal{N} M_s^2 \qquad 1.21$$

This is the basic energy formula. The other simple shapes can be approximated to ellipsoids. When the ellipsoid is magnetized along hard or easy directions, the difference in the magnetostatic energy can be used to derive the anisotropy energy. For the ellipsoid, the demagnetizing factor for the easy direction is $\mathcal{N}$ and for the hard direction is $\frac{1}{2}(1-\mathcal{N})$. Hence, the energy difference is:

$$\Delta\varepsilon_m = \frac{1}{2}\mu_0 V M_s^2 \left[\frac{1}{2}(1-\mathcal{N}) - \mathcal{N}\right]. \qquad 1.22$$

Thus, the shape anisotropy for an ellipsoid is:

$$K_{\text{sh}} = \frac{1}{4}\mu_0 M_s^2 (1-3N), \qquad 1.23$$

For uniaxial sphered shape, the $\mathcal{N}$ =1/3 which means the K_{sh} is zero, with no contribution to the anisotropy energy. And for thin films, the demagnetizing factor $\mathcal{N}$ is 1 at the perpendicular to plane direction. Thus, the shape anisotropy of a thin film is:

$$K_{\text{sh}} = -\frac{1}{2}\mu_0 M_s^2, \qquad 1.24$$

The value of shape anisotropy and MCA for Fe, Co and Ni are listed in Table 1-2

Table 1-2 magnetocrystalline anisotropy and shape anisotropy in Fe, Co and Ni at 4K.

Unit: J/m^3	Fe(bcc)	Co(hcp)	Ni(fcc)
MCA (1$^{\text{st}}$ order)	54,800	760,000	-126,300
Shape anisotropy	1,910,000	1,290,000	171,000

It is easily being awarded that for thin films, the shape anisotropy dominates the over MCA.

However, it is not always that thin film will have easy axis along the film's plane direction since shape anisotropy dominate the MA. Especially when the film is thin enough, it is necessary to reconsidering the MCA since the *surface/interface* contribution cannot be ignored as the dissuasions about MCA above, where an infinite sphere crystal, with MCA coming all from volume contribution without any consideration of the *surface/interface*. Néel pointed it out that atoms located near an interface is different from those of the bulk,[45] witch contributed to the MA as symmetry is always broken near the surface/interface. Thus, it is better to distinguish the surface contribution and the volume contribution as:
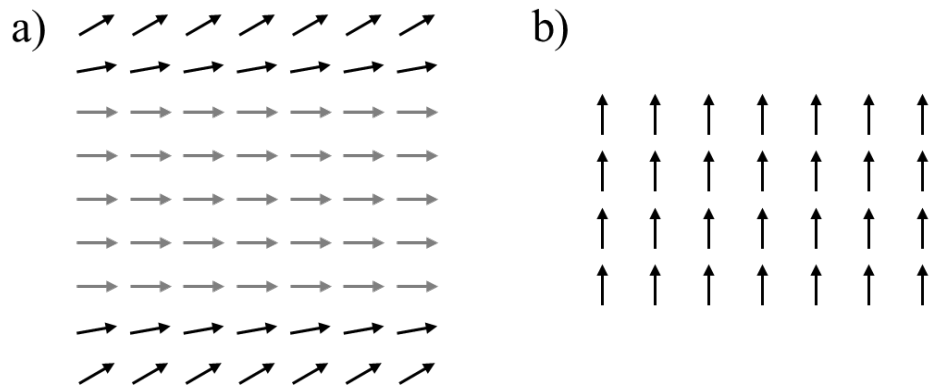
$$K = K_V + \frac{K_S}{t}, \qquad 1.25$$

Figure 1.27 The illustration for reorientation phase transition from a) thick films to b) thin films

Considering the surface contribution, one can assume a system that the bulk moments prefer to lay in-plane of the film, and the surface moments prefer to perpendicular to the film as Figure 1.28 a) shows. When the film is thick enough, the contributions is dominated by the bulk component, which shows an in-plane easy axis. However, when the film is thin enough, then the strong enough surface anisotropy can reorient the whole moments perpendicular to the film. And this the perpendicular magnetic anisotropy(PMA), which plays a very important role in various application of thin magnetic films. The next section will be a detailed introduction about the PMA.

1.2.2　Perpendicular magnetic anisotropy

As mentioned above, the easy axis is normally in-plane of films since the shape anisotropy dominates. However, the PMA exists when an ultra-thin film is investigated due to the in-negligible contribution from the surface/interface. Generally, the broken of symmetry near the interface is the origin of the surface anisotropy. When the contribution from surface is larger than from bulk, the film presents with out-plane easy axis.

1954, *Néel* firstly pointed out that the atoms located near a surface/interface have total different circumstance comparing with those inside the bulk, which will result in the interface/surface anisotropy.[45] In 1968, the first experiment was performed by *Gradmann* and *Muller* on ultrathin NiFe films on Cu(111) to reveal such an interface anisotropy.[46] In their study, a 1.8 monolayers of NiFe was observed with an easy axis perpendicular to the film plane.
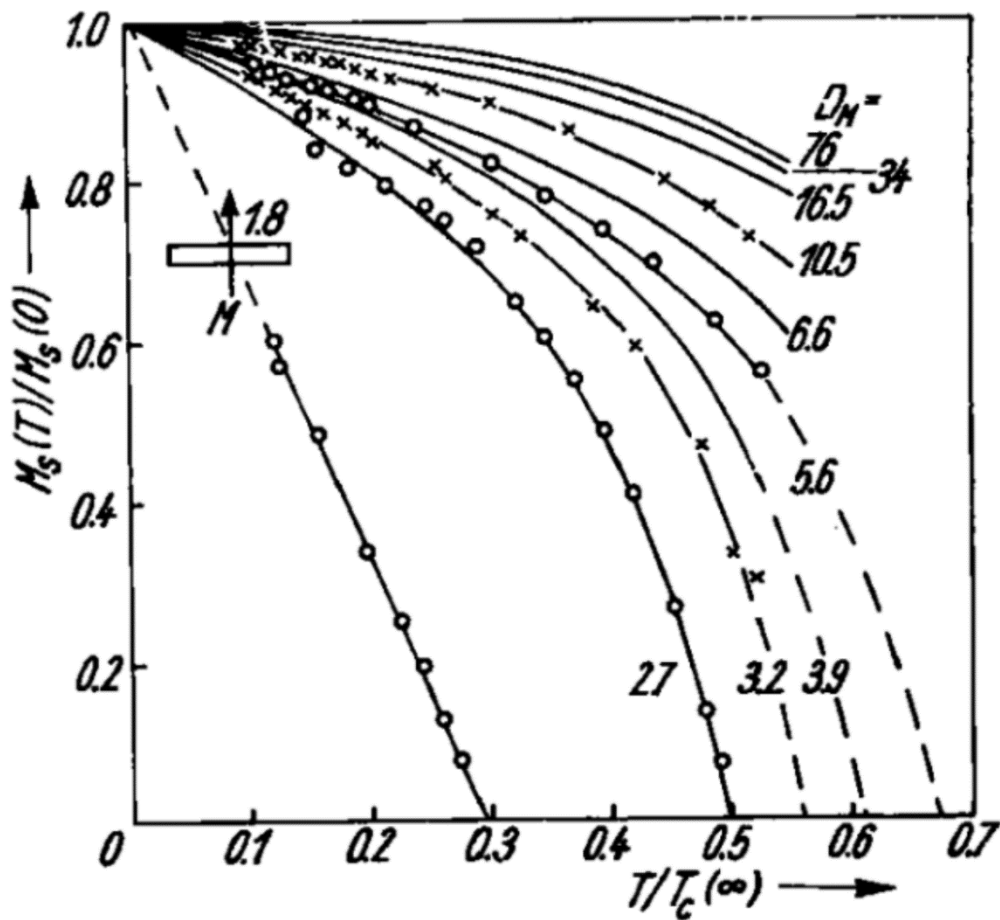

Figure 1.28 Magnetization temperature dependence of NiFe, where 1.8 ML sample show a perpendicular easy axis while others with in-plane easy axis. Reprinted from [46] with permission. ©2000 by John Wiley Sons, Inc.

In these studies, the anisotropy energy, exactly speaking, effective anisotropy energy is described with both contribution from volume and surface/interface. A typical NM/FM/NM structure is described as:

$$K = K_{eff} = K_v + \frac{2K_s}{t},$$

1.26

where K_v (Jm^{-3}) is the volume contribution and K_s (Jm^{-2}) is the surface/interface contribution. The

thickness of magnetic layer is used for the convention of volume and surface. And the factor 2 is given with the two interfaces. From this, one can easily figure out the K_V and K_s distinctly with the plot of K_{eff} and thickness of materials. Figure 1.30 [47] is a typical example of Co/Pd multilayers by *den Broeder*[48]. When the K_{eff} is positive, it means the magentization perfered lay perpendicularly to the plane of sample and negative for the parallel to the plane of sample. And the negative slope, namely negative volume anisotropy K_V, trends to make the magnetization lay the in plane direaction, while the positive intercept indicating a postive K_s which favors perpendicular magentization. Such a conflict between the K_s and K_V make it possible that under a certain value of thickness $t_\perp$, the K_{eff} will be a positive value which makes the whole sample show perpedicualr magentic anisotropy and above this certain value, the K_V will prevail and make the whole sample show in-plane magentic anisotropy.
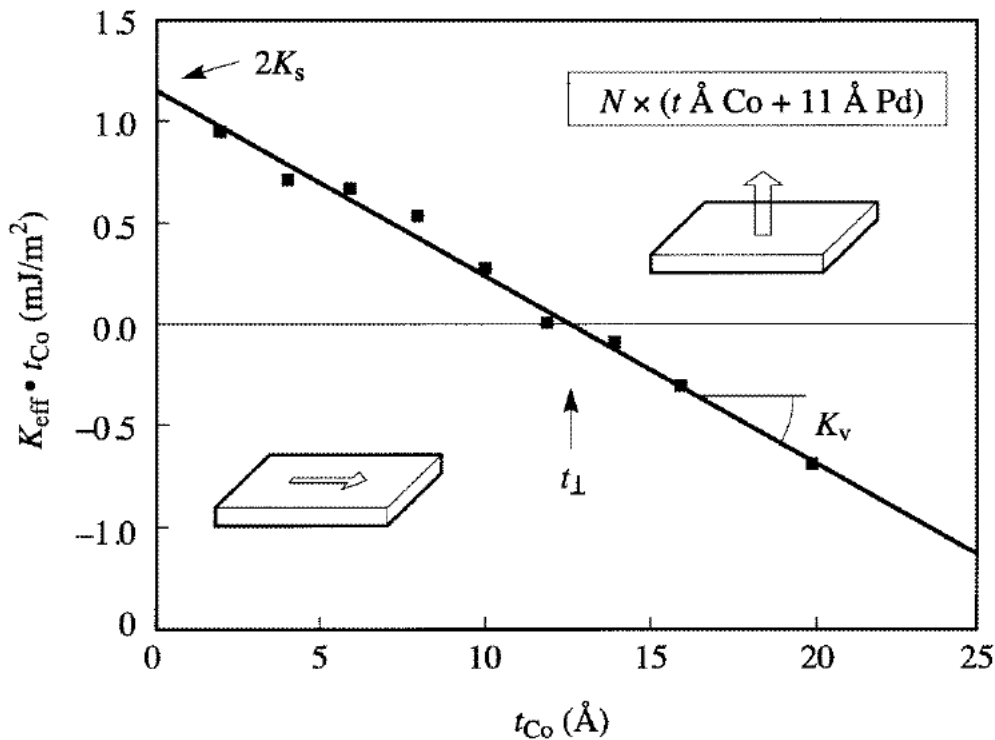

Figure 1.29 Thickness dependence of MAE of cobalt in Co/Pd multilayer structure. Reprintted with permision from [47] ©1996 by IOP publishing.

With the development of PMA, it firstly wildly utilized in the application of HDDs, where the PMA can significant increase the data storage density by minimizing the domain size with the PMA. These PMA materials used for HDDs are basically alloy materials with large spin-orbital coupling (SOC) such as CoPt based alloy or multilayers. Since the topic will focus on thin films, especially related to MRAMs. The following part will focus on the PMA arise from transition metal/oxide interface, which is identified as interfacial-PMA(i-PMA) and its energy density usually expressed as:

$$K_{eff} = K_v - \frac{1}{2}\mu_0 M_s^2 + \frac{K_i}{t}, \qquad 1.27$$

where K_v is the contribution from bulk, $-(\mu_0/2)M_s^2$ is the demagnetization energy and K_i is the sum of contribution from the surface: one surface or both two surfaces. As the demagnetization energy is a thickness-independent value, the plot of K_{eff} versus t still works to figure these values out, where the slope representing the net bulk anisotropy and intercept with vertical axis representing the net interfacial anisotropy.

Comparing with the PMA observed in large SOC system such as Co/Pt (~1.4mJ/m^2), the first observation of i-PMA in a CoFe/alumina based MTJ[49] is quite small, however, very surprising considering there is neither heave metal materials nor large SOC from theoretical calculation. In their, study, anomalous Hall effect(AHE), also known as extraordinary Hall effect(EHE) is measure for sample with CoFe/AlO$_x$ where AlO$_x$ post-oxidized from Al with external field applied out-plane of thin films. The EHE signal shows an out plane easy axis within certain range of the Al layer as Figure 1.31[49] shows. *Monso et al* assumed this i-PMA comes from the CoFe/AlO$_x$ interface as oxidization penetrates from the top.
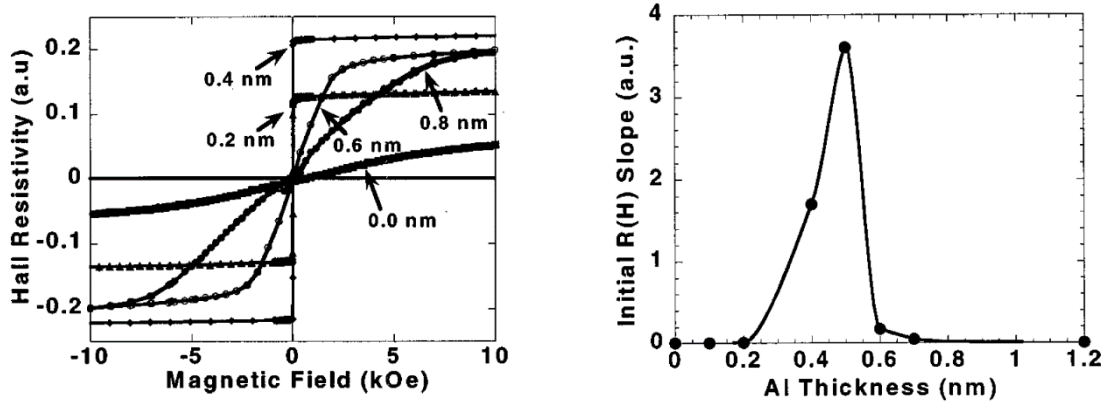
Figure 1.30 a) EHE signals with different t_{Al} and initial R(H) slope versus t_{Al}. A large slope indicates an out-plane easy axis. Reproduced from [49], with the permission of AIP Publishing..

This kind of phenomenon is soon found existed in many materials systems except AlO$_x$ such as MgO$_x$, TaO$_x$ and RuO$_x$.[50] To close the hypothesis that i-PMA arise from metal/oxide interface, x-ray absorption (XAS) and x-ray photoemission (XPS) measurement is performed.[50] The results, as Figure 1.33 shows, convinced the hypothesis: the i-PMA is originated from the formation of chemical bonds between the oxygen ions in oxide and the ions in the neighboring transition metals.
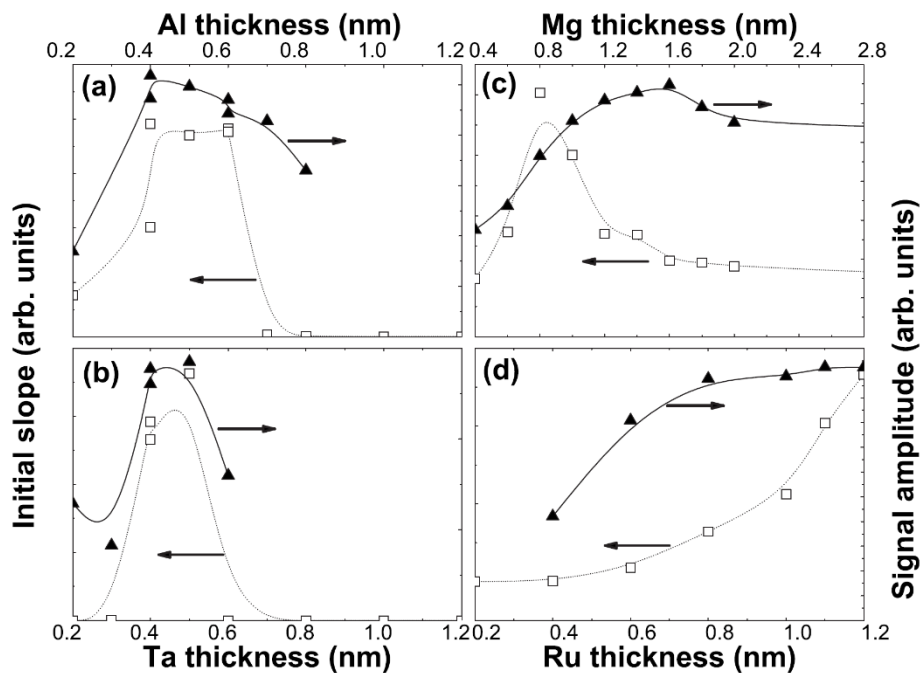

Figure 1.31 EHE measurement performed to various materials with out-plane external field. Reproduced from [50],
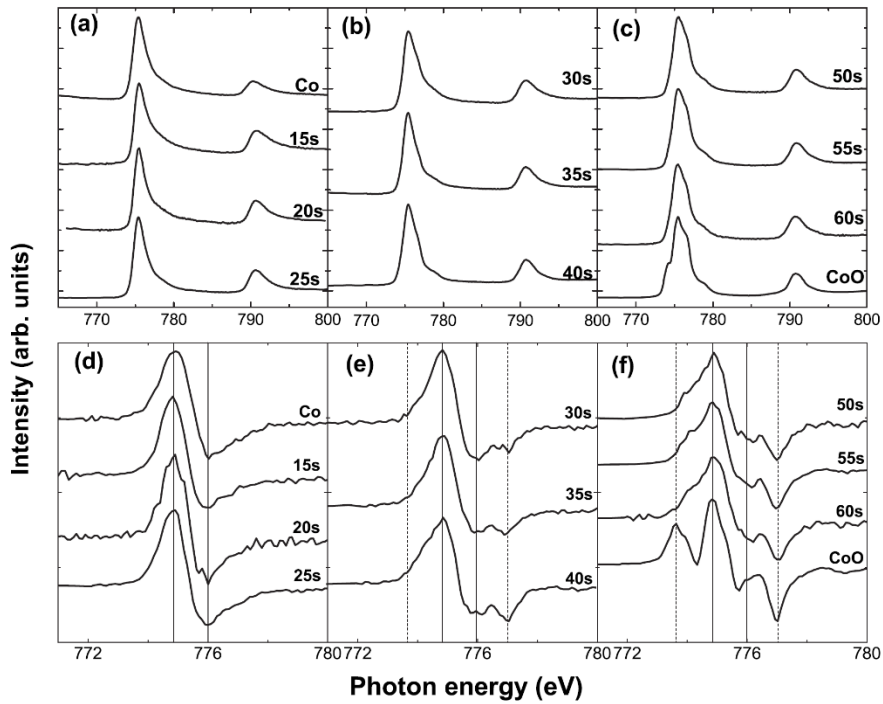
with the permission of AIP Publishing.

Figure 1.32 XAS spectrum. Reproduced from [50], with the permission of AIP Publishing.

Soon, a remarkable observation is reported by *Ikeda et al.*[16] A giant i-PMA exhibited in a Ta/CoFeB/MgO based MTJ, where the MgO is directly sputter from the oxide target. As Figure 1.34[33] shows, the i-PMA density reaches ~1.3 mJ/m^2. More important, a large TMR ratio up to 120% is obtained simultaneously. This big step towards application based on perpendicular MTJ(p-MTJ) is owing to the easy absorption of B from CoFeB by the buffer Ta layer.
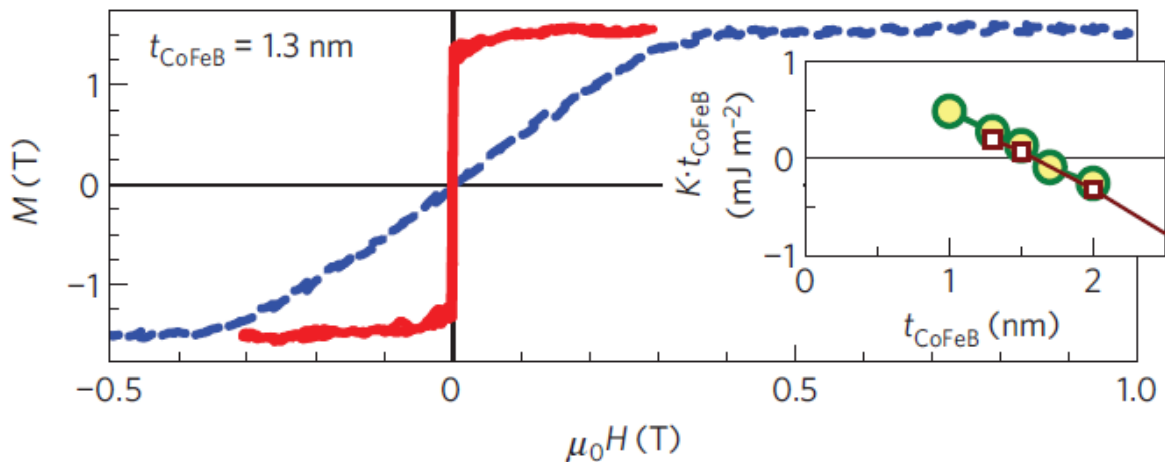
Figure 1.33 Perpendicular magnetic anisotropy of CoFeB/MgO. Reprinted with permission from [16] ©2010 by Springer Nature.

In 2013, the largest iPMA is reported by *Koo et al* from an epitaxial Fe/MgO.[51] The K_{eff} reached ~1.4MJ/m³ and K_i reached ~2.0 mJ/m² as Figure 1.35 shows. This large PMA is due to a proper oxidized Fe/oxide interface where a just Fe-O band is formed.[52]
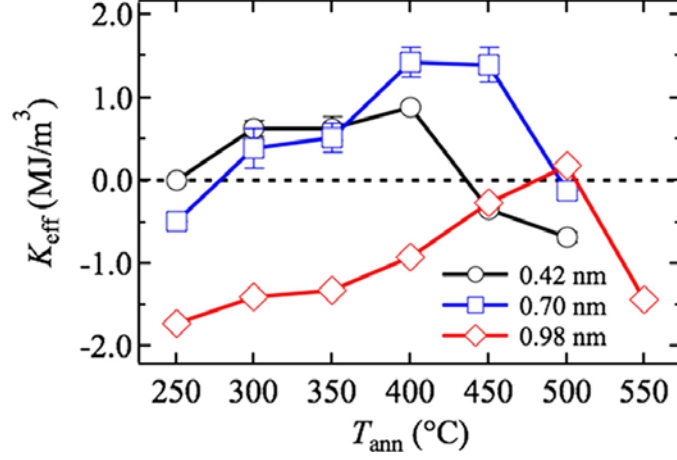

Figure 1.34 PMA energy densities regarding to various Fe thickness and annealing temperature. Reproduced from [51], with the permission of AIP Publishing.

To understand the physic pictures of the large i-PMA arise from the transition metal/oxide interface, the term of K_i in the Equation 1.27 should be well understood. And it is better start with the SOC mentioned above, which is normally large in the FM/NM type PMA samples such as Co/Pt, however, is considering weak in the FM/Oxide type i-PMA samples.

The SOC can be regarded as the string between the electron spin and the magnetic field created by the Circular motion around the nucleus, with the latter one known as orbital motion. Thus, the Hamilton term of the spin-orbital system with spherical symmetric potential can be written as[53]:

$$H_{SO} = \frac{e\hbar}{4m^2c^2r}\frac{dV}{dr}\boldsymbol{\sigma}\cdot(\mathbf{r}\times\mathbf{p}) = \frac{e\hbar}{2m^2c^2r}\frac{dV}{dr}\mathbf{L}\cdot\mathbf{S} = \xi(r)\mathbf{L}\cdot\mathbf{S},$$
1.28

where the $\mathbf{L}\cdot\mathbf{S}$ is the product of the orbital angular momentum and spin operator, which can be written using the longitudinal and ladder operators as:

$$\mathbf{L}\cdot\mathbf{S} = \frac{1}{2}(L_+S_- + L_-S_+) + L_ZS_Z$$
1.29

thus, Equation 1.28 can be rewritten in a matrix form:

$$H_{SO} = \xi(r)\begin{pmatrix} H_{SO}^{\uparrow\uparrow} & H_{SO}^{\uparrow\downarrow} \\ H_{SO}^{\downarrow\uparrow} & H_{SO}^{\downarrow\downarrow} \end{pmatrix} = \frac{1}{2}\xi(r)\begin{pmatrix} L_Z & L_- \\ L_+ & -L_Z \end{pmatrix},$$
1.30

For simplicity, considering a free magnetic atom with l=2d orbitals, with the existence of the SOC, the eigenstates of the Hamiltonian matrix are as follows:

$$|d_{xy};\sigma\rangle = \frac{i}{\sqrt{2}}(|-2;\sigma\rangle - |2;\sigma\rangle),$$

$$|d_{yz};\sigma\rangle = \frac{i}{\sqrt{2}}(|-1;\sigma\rangle + |1;\sigma\rangle),$$

$$|d_{3z^2-r^2};\sigma\rangle = (|0;\sigma\rangle),$$
1.31

$$|d_{xz};\sigma\rangle = \frac{1}{\sqrt{2}}(|-1;\sigma\rangle - |1;\sigma\rangle),$$

$$|d_{x^2-y^2};\sigma\rangle = \frac{1}{\sqrt{2}}(|-2;\sigma\rangle - |2;\sigma\rangle),$$

It is obvious that the spin-up $d_{3z^2-r^2}$ state is mixed with the spin-down d_{xz} and d_{yz} states though SOC

in states with $m_j = \pm 1/2$. This kind of hybridization through SOC is considered as the origin of the interfacial PMA especially arise from the Fe/Oxide interface, as reported by *Yang et al* in 2011.[52] In their *ab initio* calculation, the SOC effect on the Fe/Oxide is carefully evaluated that with or without SOC it exhibited different PMA energies. Moreover, the oxidation conditions are also evaluated that both over-oxidation or under-oxidation will significantly reduce the value of i-PMA.
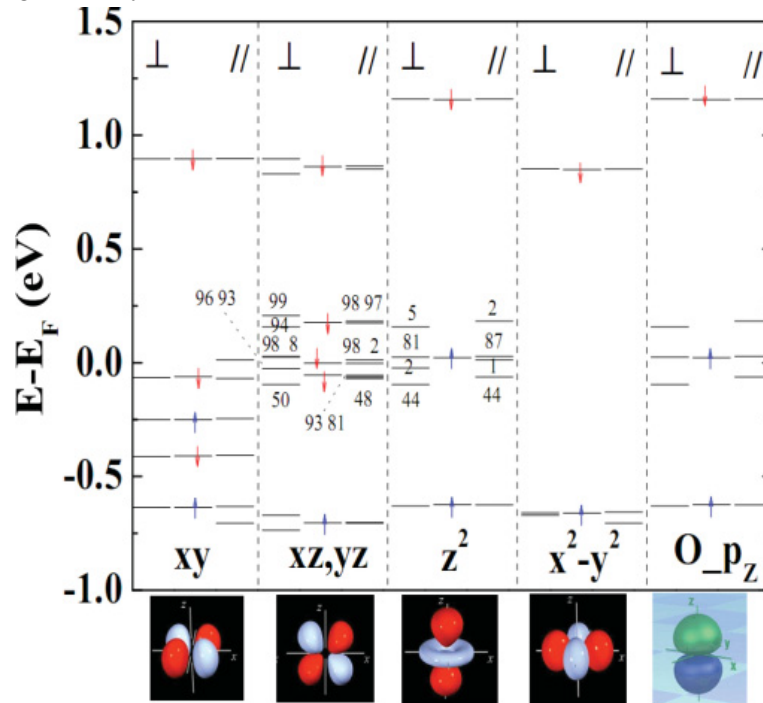

Figure 1.35 *ab initio* calculation of Spin-orbit coupling effects on interfacial Fe d and neighbor oxygen p_z orbitals for the pure Fe/MgO interface. In each column, the band levels are shown for no SOC case(middle) and with SOC case for out-of-pane and in-plane orientations of magnetizations. Reprinted with permission from [52]. ©2011 by the American Physical Society.

1.2.3   Manipulation of perpendicular magnetic anisotropy

The PMA is a very important role for development of the modern magnetic memories. It not only determines the possibilities to reduce the junction size to increase storage density, but also determines the data storage endurance and writing energy efficiency directly. Here, the benefit to reduce junction size by introducing PMA to the p-MTJ is easy to understand naturally, the latter two about storage endurance and writing energy efficiency will be detailed introduced.

Regarding the data storage of magnetic materials, no matter the HDDs, the Magento-disk or the magnetic memories, the fundamental idea is how to keep the magnetization, or more exactly, the direction of the magnetization. As the bistable states coming from the configuration of the magnetization directions, if the magnetization is easily reversed, then the data is easily lost

Thus, by evaluate how difficult the magnetization reversed, one can easily see how stable this system is. And the major origin of this kind of disturbance is thermal thus the endurance is normally correlated with the thermal stability.

Nevertheless, as the anisotropy always existed with those pattern small junctions or small magnetic domains, the energy that required to switch the magnetization of the two states is just the anisotropy energy as discussed in the beginning of the Chapter 1.2.1, connected the volume of the small magnetic materials should be:

$$\Delta E = K_u V, \tag{1.32}$$

where the K_u is the anisotropy energy density (in J/m^3) no matter the anisotropy is in-plane or out-plane or just uniaxial. And this energy gap is also called as energy barrier as Figure 1.37 shows.
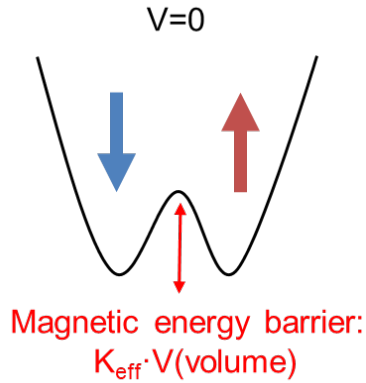

Figure 1.36 the magnetic energy barrier in a typical bistable data storage element.

If one system has a small ΔE, it indicated that switch of the magnetization is easily switched by accident due to the thermal fluctuations, i.e. $K_B T$. By statics analysis, the information degradation by the thermal fluctuations is defined by the time required to switch the magnetizations trough the energy barrier as:

$$\tau = \tau_0 \exp(\frac{\Delta E}{K_B T}), \tag{1.33}$$

where τ_0 is a characteristic attempt time of ns order. Thus, we can connect this time with a so-called retention time (T_r), which described how long one want the information stored stable with the requirement of the energy barrier:

$$\Delta E > K_B T \tau_0 \log(\frac{T_r}{\tau_0}),$$

1.34

And normally, for a p-MTJ to store the information over 10 years, the ΔE is required to:

$$\Delta E = K_u V > 60 K_B T,$$

1.35

From this we can roughly calculated that for an MTJ with a junction size less than 20 nm and free layer around 1 nm, a K_u larger than $1MJ/m^3$ is normally required.

One may think, as discussed above, it seems that the larger ΔE is, the more stable for the storage system. And it is even possible to obtain infinite endurance time to store information just if we get large enough ΔE. However, the nature never provides perfect solution for human. The ΔE is also related to another important sided for data storage: that is writing information. It is easily understood that for writing data, the magnetization must be switched desirably. I.e. for the MTJ, if one wants to write "0", the free layer must be switched to parallel to the reference layer, while if to write "1", it must be switched to antiparallel to. And the energy cost to switch is also the energy barrier discussed above. For example in the STT switch method, the current required to switch the magnetization is[54]:

$$I_{c0} = \left[\frac{4ek_B T}{\hbar}\right]\frac{\alpha}{\eta}\frac{\Delta E}{K_B T},$$

1.36

and it is clear to see the critical current for switch process is proportional to the energy barrier.

Facing such a dilemma, a natural idea is that if, the magnetic anisotropy can be manipulated, i.e. in the STT switch, the energy barrier is reduced for writing process while keeps a high value for long endurance besides the writing, then it is possible to achieve both low writing energy and long endurance/ better stability.

The most promising method to manipulate the magnetic anisotropy is introduced the voltage induced modification as considering the usage for magnetic memories. Actually in 1965, it was already observed the potential applied to the rare earth materials can modify its magnetic properties.[55] Until 2007, *Weisheit et al.* firstly reported about the electric-field induced modification for ferromagnetic thin films[56]. However, in this work, a liquid electrolyte is required for applying a high electric field to the thin film surface. The first experiment for voltage induced perpendicular magnetic anisotropy modification in an all solid state thin film was carried out in 2009, by *Maruyama et al.*[15] From then, how to utilize the voltage induced PMA modification to provide a more efficient writing technique start to be a hot topic. And this phenomenon is described as voltage-controlled magnetic anisotropy(VCMA).
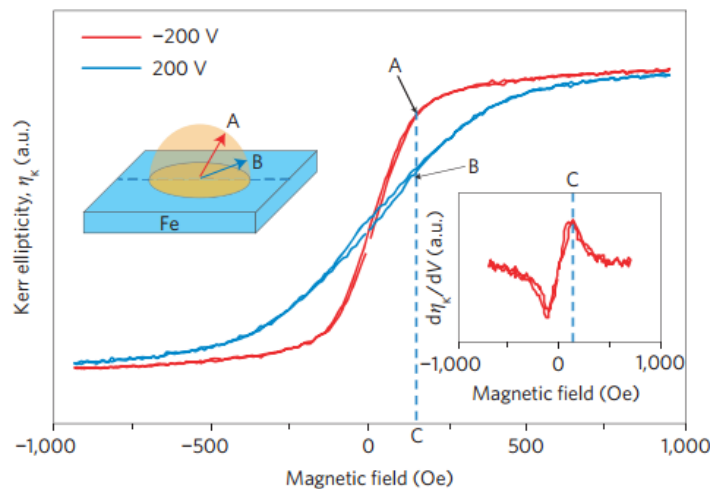

Figure 1.37 Voltage-controlled magnetic anisotropy in ultrathin-Fe, reprinted with permission from [15] ©2009 by Springer Nature.
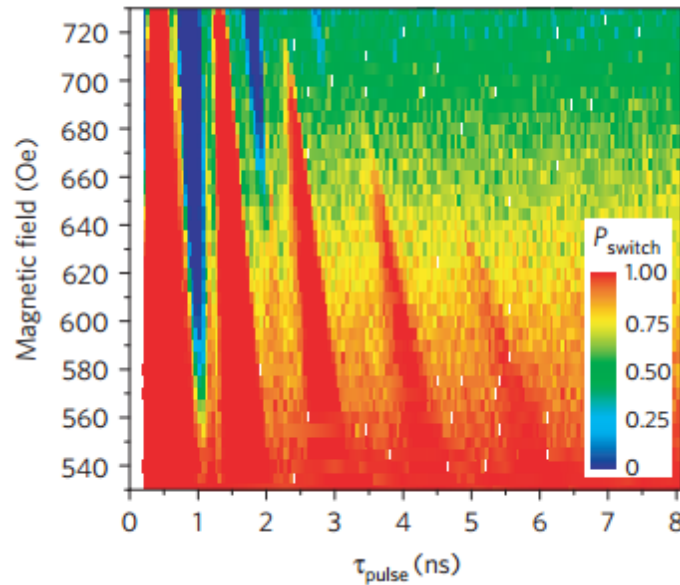
Figure 1.38 Magnetization switched by pulse. reprinted from [57] ©2012, with permission from Springer Nature.
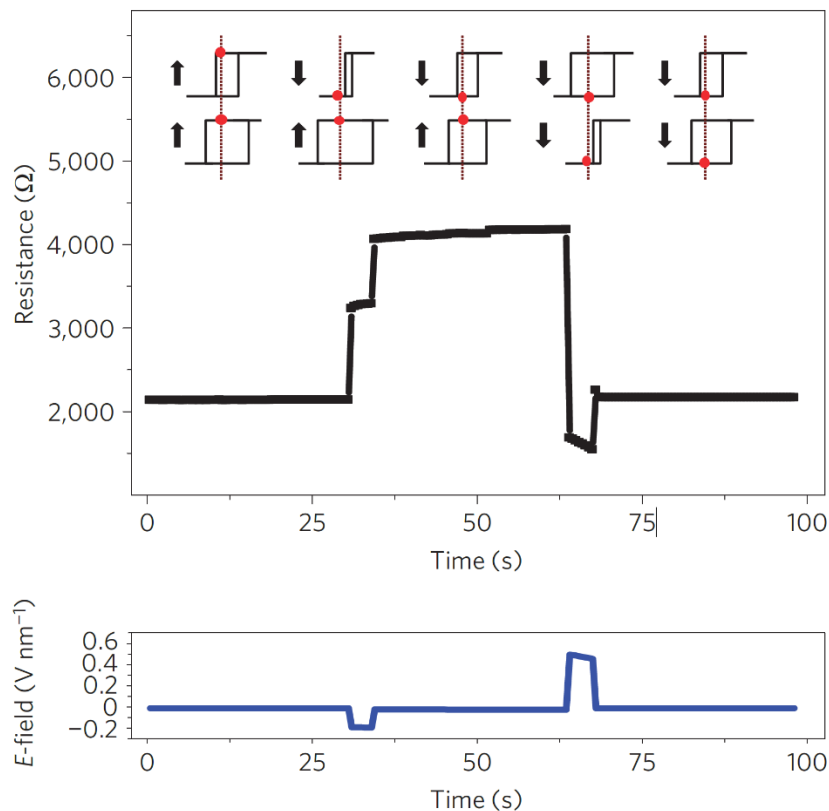

Figure 1.39 Resistance change by voltage-assisted coercivity manipulation. reprinted with permission from [58] ©2012 by springer Nature.

In the experiment of *Maruyama et al.*, ultrathin Fe/MgO MTJs are used, which is the typical element for MRAMs. Figure 1.38[15] shows the **M-H** curves under large external voltages of ±200V. For 200V, the easy axis is close to in-plane direction of the Fe thin film, while for -200V, close to out-of-plane direction. Such a clear modification, up to ~39% change due to the report, indicated a viable way to switch the magnetization by voltage itself: "pushing" the magnetization into precession motion to cross the energy barrier by the initial

32

application of the voltage.

Soon in 2012, the switching of the magnetization related to the voltage-controlled magnetic anisotropy are reported by two groups. *Shiota et al.* applied electric field pulses to MTJs to realize coherent processional magnetization switching.[59] A FeCo/MgO/Fe MTJ with orthogonally aligned magnetizations in top and bottom layers is used. the bottom FeCo layer has perpendicular easy axis while the top Fe layer has in-plane easy axis. The junction is put in an in-plane external field. The applied electric pulse shortly "pulled" the magnetization from perpendicular to the in-plane direction, causing precession of the magnetization to switch the magnetization. Figure 1.39 shows the possibility of switching due to different external magnetic field and pulse duration. [59]

Another group, *Wang et al.* utilized the voltage introduced coercivity modification to realize the switching with field assistance.[58] As Figure 1.40[58] shows, the applied electric field reduces the coercivity of the CoFeB electrodes and make the magnetization of electrodes aligned with the applied magnetic field. However, in this design of experiment, the STT switching is believed to induce switching in the opposite direction. Besides, the switching of magnetization by VCMA combined with STT[60] or SOT[61] are also investigated.
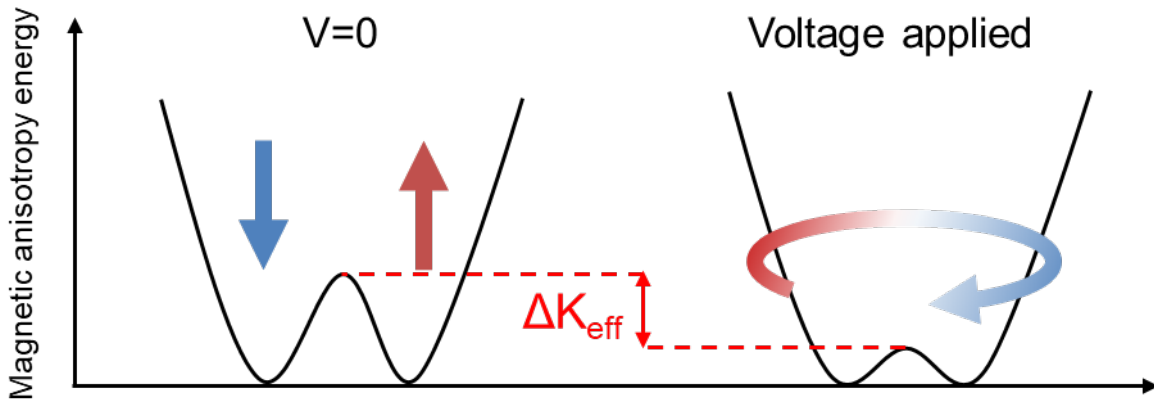
Figure 1.40 schematic illustration of PMA modulation by voltage

Among these switching methods related to VCMA, one of the most critical issue is how efficient can we modulate the PMA as Figure 1.41 shows. Hence, the VCMA coefficient is defined as the modification of PMA energy density(J/m^3) per applied electric-field(V/m) as:

$$VCMA \text{ coefficient} = \frac{\Delta K_{eff} \cdot t_{free-layer} \cdot t_{barrier}}{\Delta V}, \qquad 1.37$$

To quantitively evaluate the VCMA coefficient, *Shiota et al* developed a method by measuring the magnetoresistance of a special aligned MTJ as Figure 1.42 shows.[62] The orthogonal aligned MTJ gave a *R-H* loop when the bottom ultrathin-Fe with PMA rotating its magnetization with enlarging external field as:
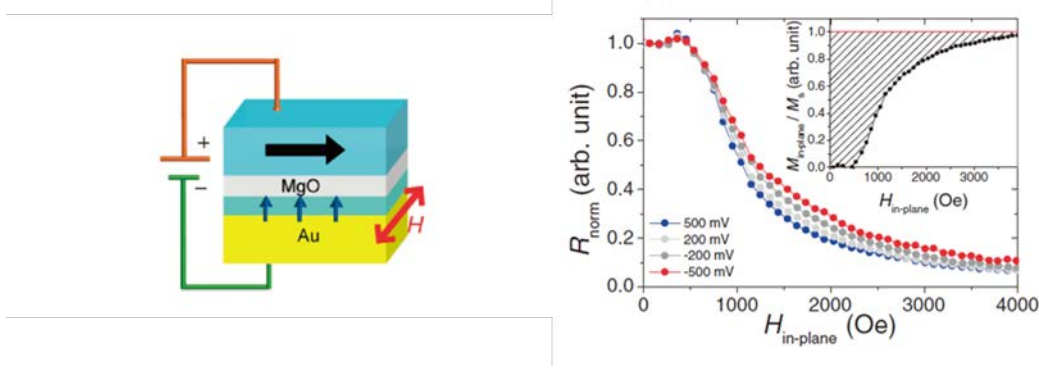
Figure 1.41 Detection of anisotropy change caused by electric field effect. Reproduced with permission from [62]. ©2011 The Japan Society of Applied Physics

$$R(\theta) = \frac{R_{90} R_p}{R_p + (R_{90} - R_p) \cdot \cos\theta} \tag{1.38}$$

Since the magnetization direction of the top Fe layer is considered to be parallel to H_{ex} (i.e., in-pane direction), the ratio of the in-plane component of the magnetization $M_{in\text{-}plane}$ to its saturation magnetization M_s in the bottom ultrathin Fe layer can be determined as:

$$\frac{M_{in-plane}}{M_s} = \cos\theta = \frac{R_{90} - R(\theta)}{R(\theta)} \frac{R_p}{R_{90} - R_p} \tag{1.39}$$

Then, the PMA energy density can be evaluated as:

$$k_{eff} = \int_0^{H_k} (M_s - M_{in-plane}) dH \tag{1.40}$$

As the obtained K_{eff} is corresponded to each bias voltage, then the slope of the plot of K_{eff} and V represents the quantitively evaluation of VCMA.

To realize the practical application based on VCMA, a large VCMA is preferred with large PMA. Figure 1.43 shows recent progress on the VCMA research. The value is still far away from the requirement by application view. And the mechanism of VCMA is still not solid. There are many unexplored places regarding the manipulation of magnetic anisotropy through electric method. In this study, I focused on exploring the VCMA of a Fe/Oxide interface, as well as its fundamental PMA and transport properties.
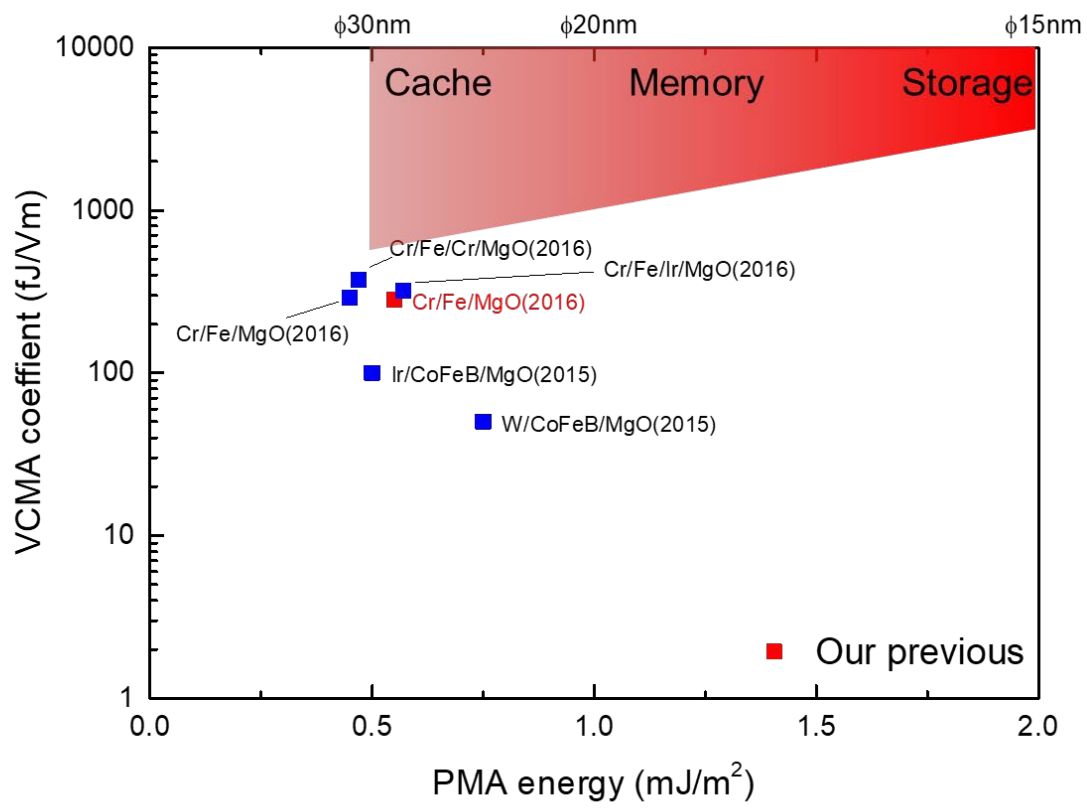
Figure 1.42 Summary of recent VCMA and PMA researches.

Chapter 2   Experimental methods

This chapter describes the details about the experimental methods used in this study, including but not only the sample preparation, characterization, measurement set-up and related calibrations. The basic introduction of each instrument used in this study is briefly given. However, the underneath mechanism and related physics are just slightly touched due to the author's limited knowledge. Some details about the measurement set-up is also discussed though the set-up may not be perfect. In general, the topic is given by the natural order of the experiment: sample preparation including magnetron sputtering and electron-beam(EB) evaporation, microfabrication, measurement including in-situ RHHED measurement, magnetic properties measurement using vibrating sample magnetometer (VSM) and VSM incorporated with superconducting quantum interference device (SQUID), transport measurement using 4-probe direct current(DC) and physical property measurement system (PPMS).

2.1   Sample preparation

The very important factor that spintronics developed almost 60 years later than the observation of spin, is due to the poor sample preparation techniques. Unlike other subjects, the spintronics research requires precise sample preparation techniques such as molecular. beam. epitaxy (MBE). The early observation of GMR, by Fert and Grunberg, both relies on the thin film prepared by MBE. And the quick commercialization of GMR, is based on the preparation method transferred from MBE to sputtering technique by Parkin in 1991, which is favored by industrial people. In this section, these two major techniques are introduced due their irreplaceability: evaporation method for precise control of ultrathin film and sputtering method for very high efficiency.

2.1.1   Electron-beam evaporation

Electron-beam evaporation is a type of MBE, which utilizes electron beam to heat the source materials. Figure 2.1 shows the typical schematic of EB evaporation. Usually the electron beams come from a tungsten filament under high vacuum, and then are steered by the magnetic field to reach source materials.

By adjusting the power of the filament, the strength of electron beam can be modulated in a wide range, which leads to a wide deposition rate also: up to few micrometers per minute and down to sub-nanometer per minute. The ultra-low deposition rate, combined with the high vacuum during the deposition, one can realize precise control of the film deposition, with flat and uniform surfaces.
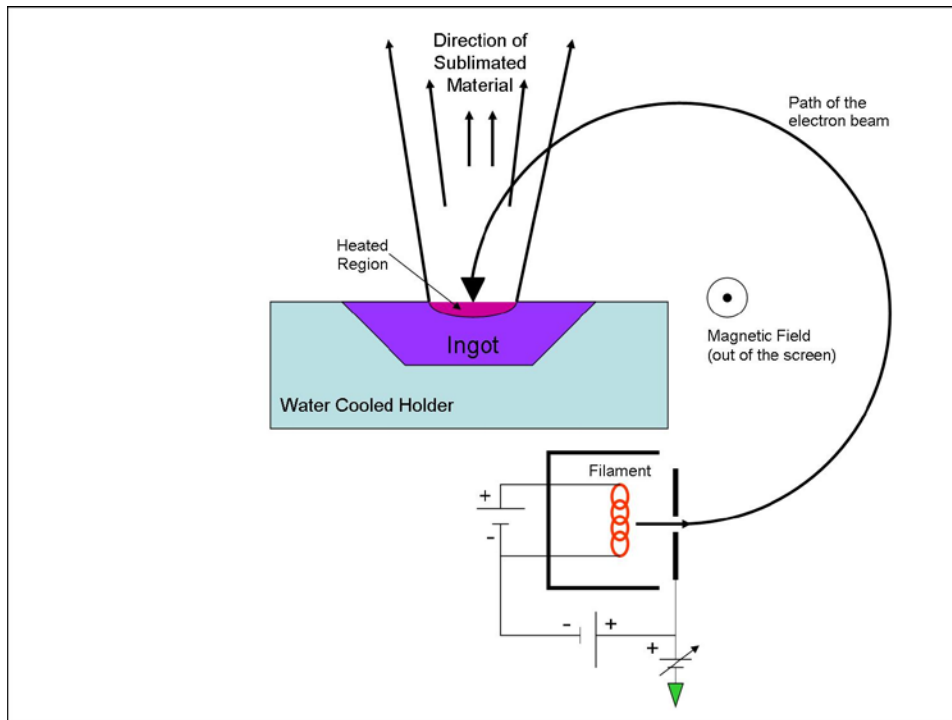
Figure 2.1 Illustration of EB evaporation, adapted from Wikipedia.
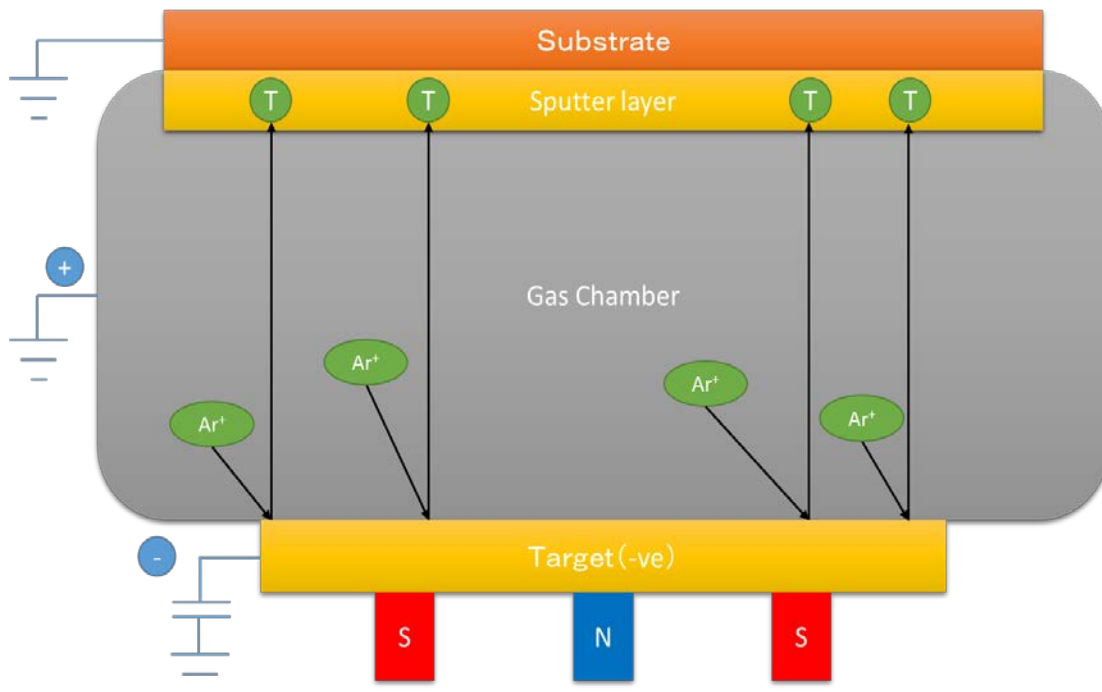
2.1.2　Sputtering

Figure 2.2 Schematic illustration of magnetron sputtering system.

Sputtering, as one kind of *Physical Vapor Deposition* (PVD) techniques, is widely used in industrial due to its wide coverage of "target" materials.

As Figure 2.2 shows, generally, during the deposition, the gas, normally Ar, is ionized by applied power,

which leads to the formation of plasma near the target cathode. The ionized gas has a positive core and a negative charge around it. And as the gas ions have high energy, when they are attracted by the target cathodes due to coulomb attraction, bombardment of the gas occurs on to the target, which leads to ejection of target atoms from the surface. Limited ejected atoms will reach the substrate and form thin films.
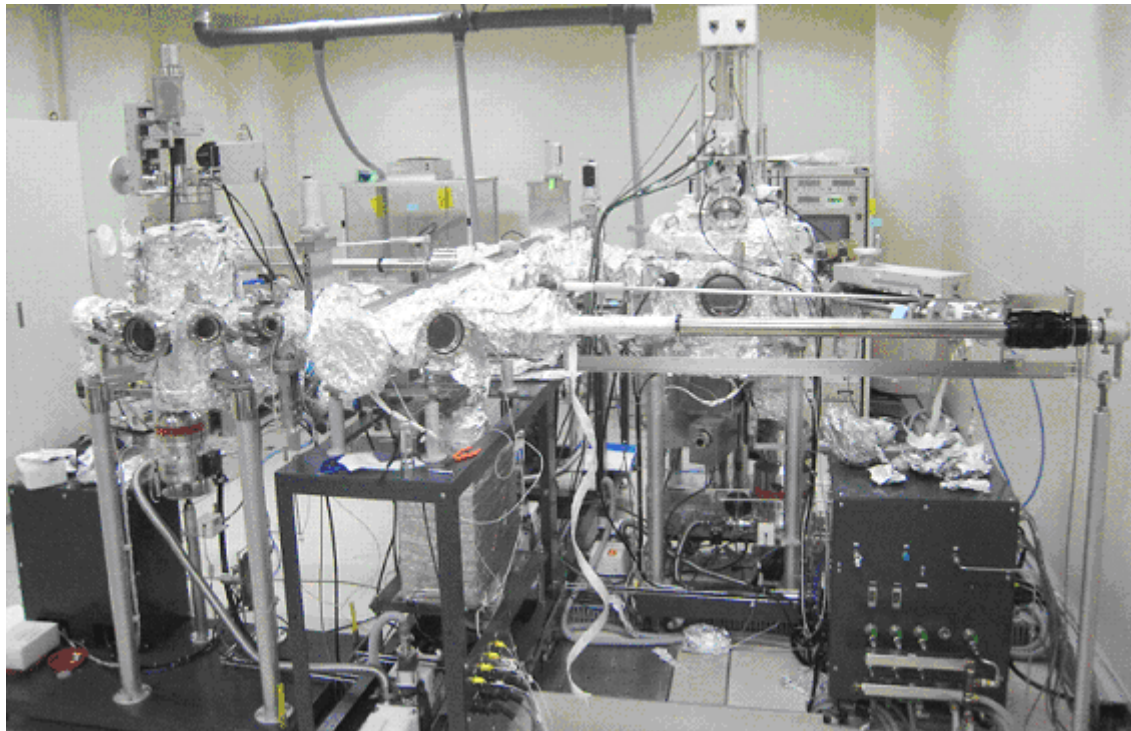
Figure 2.3 Picture of the sputtering system

In this study, a magnetron sputter system allowing possibility of 10 different targets to be deposited one over the other is used. A turbo molecular pump is used to drive the chamber down to the ultra-high vacuum regime (order of 10^{-7}~10^{-8} Pa.), which prevents the surface from contamination. In addition to the sputtering chamber (i.e.: the setup on the right) where deposition performed, there is also an oxidation chamber (seen on the left) and a transport chamber enabling heat treatment and sample loading/unloading respectively.

2.2 Microfabrication

Microfabrication is the most important work during the exploration of the transport properties. Generally, the microfabrication contains the following procedures: photo or electron beam lithography, milling, lift-off and deposition as following:

Promoter: Hexamethyldisilane(HMDS)   photoresist: ma-N1407   Developer: ma-D533

Remover: N-Methyl-2-pyrrolidone(NMP)   Rinse: Butanone

1) Spin coat with HMDS at 1000 rpm for 10s then 3000 rpm 40s
2) Post bake at 100°C for 3 mins
3) Spin coat with ma-N1407 at 1000 rpm for 10s then 3000 rpm 40s
4) Post bake at 100°C for 1.5 min
5) Exposure for 100 seconds under ultraviolet light source
6) Develop with ma-D535 for 40 seconds
7) Milling or sputtering
8) Lift-off with NMP, rinse with Butanone

The details of our procedure for microfabrication of the MTJs is schematically demonstrate in Figure 2.4:

1) Milling the cap for cleaning the surface with 250V, 30 seconds
2) Photo the bottom electrode pattern
3) Milling the bottom electrode until substrate with the milling angle of 60°
4) Sputter SiO2 around 50 nm
5) Lift-off for bottom electrode
6) Photo junction pattern
7) Milling junction with optimized angel control, until bottom electrode materials
8) Lift-off for junctions
9) Photo removal pattern
10) Milling removal until buffer layer
11) Sputter 3nm Ta and 100nm Au
12) Lift-off for removal
13) Photo pad pattern
14) Sputter SiO2 for 50 nm
15) Lift-off for pad
16) Photo Top electrode pattern
17) Milling top for cleaning surface around 20 seconds
18) Sputter 3nm Ta and 100nm Au
19) Lift-off top electrode pattern

As mentioned in the procedures, an angel control is performed to optimize the microfabrication. This is due a critical issue in MTJ microfabrication: redeposition problem. During the milling process, the etched materials will just redeposit to the sides. When one performs the junction milling, this kind of redeposition will easily make the MTJs shorted once it occurs to cover the insulator layer. Thus, during the normal milling process, we use 60° angel to avoid the redeposition. However, when deposit the junctions, a fixed 60° will cause the shadowing effect, which make the size of the junction bottom electrode much larger than designed.

To avoid that, a multi-angels-control process is performed with repeating 25° and 70° milling every 30 seconds.
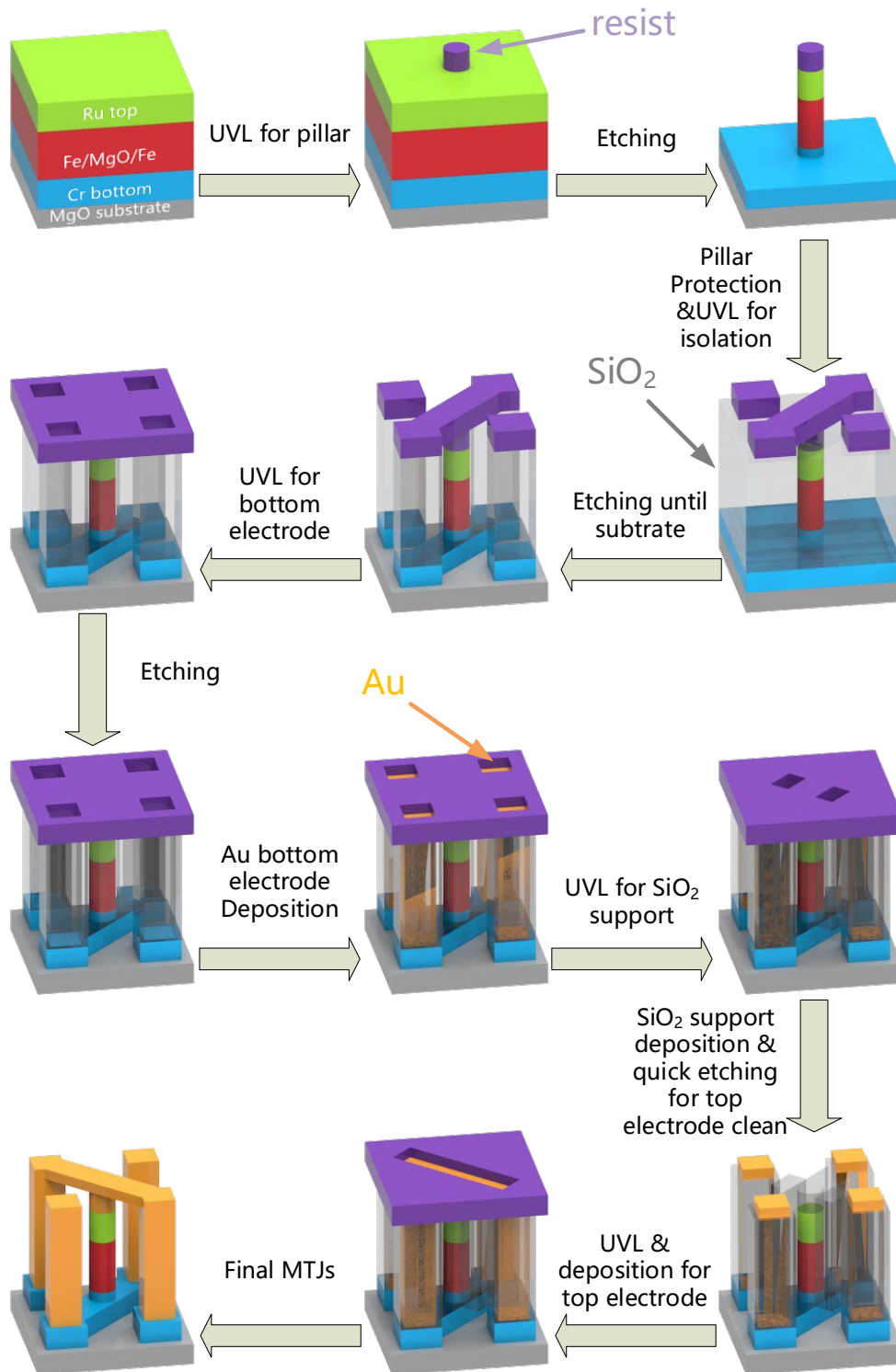
Figure 2.4 Process for microfabrication

2.3 Measurement

2.3.1 Structural characterization

2.3.1.1 Atomic force microscopy

Atomic force microscopy (AFM) is a very high solution scanning probe microscopy, which can easily reach the order of nanometer, thousands of times higher than the optical diffraction limit. This kind of microscopy use a real probe to approach the surface of specimen and force will appear between the surface and the probe. Due to the Hooke's Law, a deflection of the cantilever will be caused by the forces. And the information is gathered by detecting the change of the forces. After a whole scanning, it is easy to rebuild the surface conditions among the scanning zone. Using this method, one can easily obtain the roughness information. And it is also possible to use it to check is there any pinholes or unexpected construction damage during the deposition and post annealing.
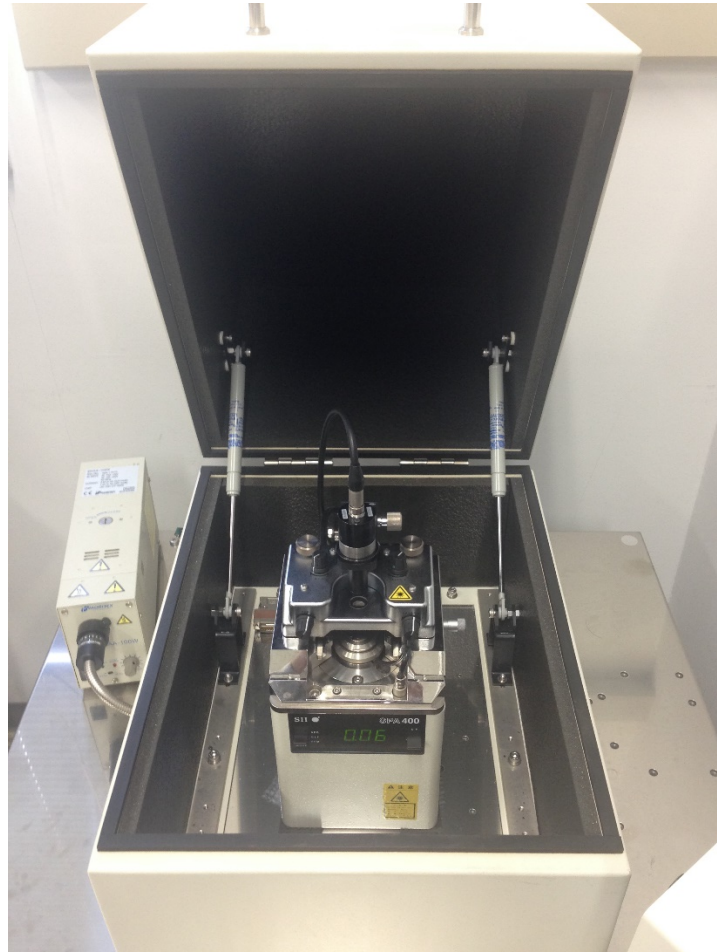
Figure 2.5 AFM used in this study

Figure 2.6 is a typical scanning result of Cr layer by an AFM. The Cr layer is post-annealed at 800°C, which grants a terrace surface with high flatness.

	Z1[nm]	Z2[nm]	ΔZ [nm]	Distance [nm]	Φ[°]
🟥					
🟨					
🟦					
🟩					
🟪					

Ra : 7.165E-02 nm   L : 1.230E+03 nm
P-V : 7.998E-01 nm   λc : 4.101E+02 nm
Rz : 5.968E-01 nm   Δa : 8.572E-01 °

Ra : 1.333E-01 nm
P-V : 1.800E+00 nm
Rp : 7.173E-01 nm
Rv : -1.083E+00 nm
RMS : 1.702E-01 nm

Rz : 1.239E+00 nm
(10 Points)
S : 9.998E+05 nm²
S Ratio : 1.00040

	Z Data	Histogram[%]	Bearing Ratio[%]
🟨	0.89	1.10	87.90
🟦	0.89	1.10	87.90

Pitch : 0.01 nm

File : 15N10001.xqd
Com.1 :
Com.2 :
Com.3 :
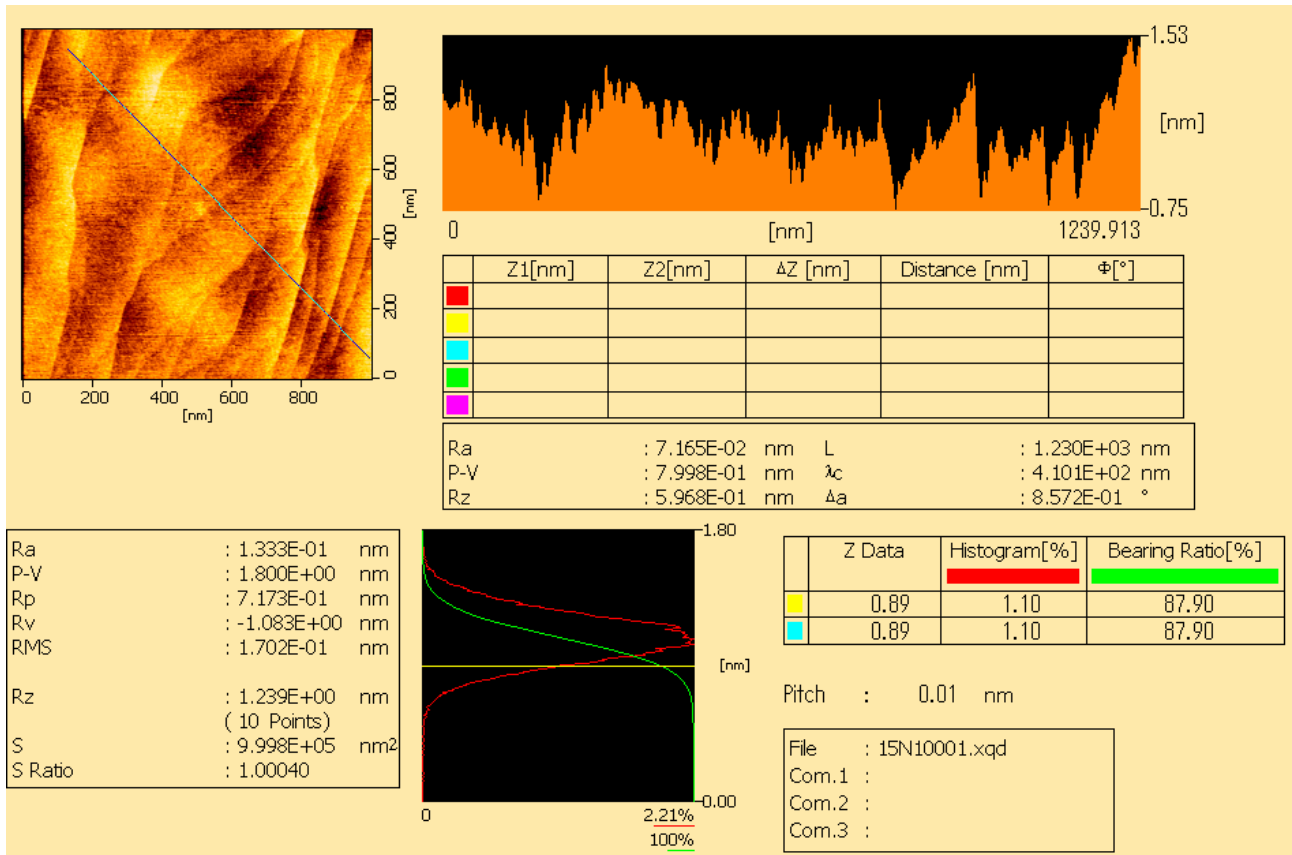
Figure 2.6 A typical AFM scanning result for surface of Cr annealed at 800°C.

2.3.1.2 Reflection high-energy electron diffraction

RHEED is an important technique used for in-situ characterization of the surface of a crystalline. Different from transmission electron microscopy, though RHHED also use high energy electrons, it only characterizes the surface layer of the sample. Figure 2.7[63] shows the basic setup for a RHEED system. The high energy electrons come out from the electron gun. These electrons form a beam and reach the sample surface at a very small angel. Then incident electrons diffract from atoms at the surface of the sample, which will cause a fraction to interfere with the electrons themselves and form a diffraction pattern on the detector. That is to say, the diffraction pattern contains the information of the sample surface.
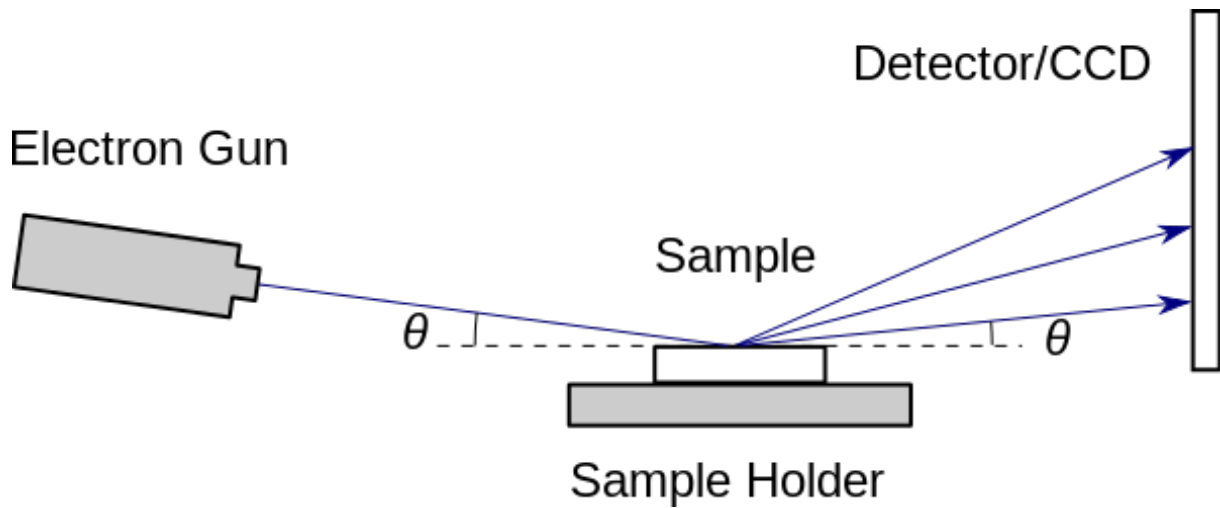
Figure 2.7 illustration of the RHEED system, adapted from Wikipedia [63].

Another benefit of the RHEED system is that one can utilize it to monitoring the growth thickness real-time[64].
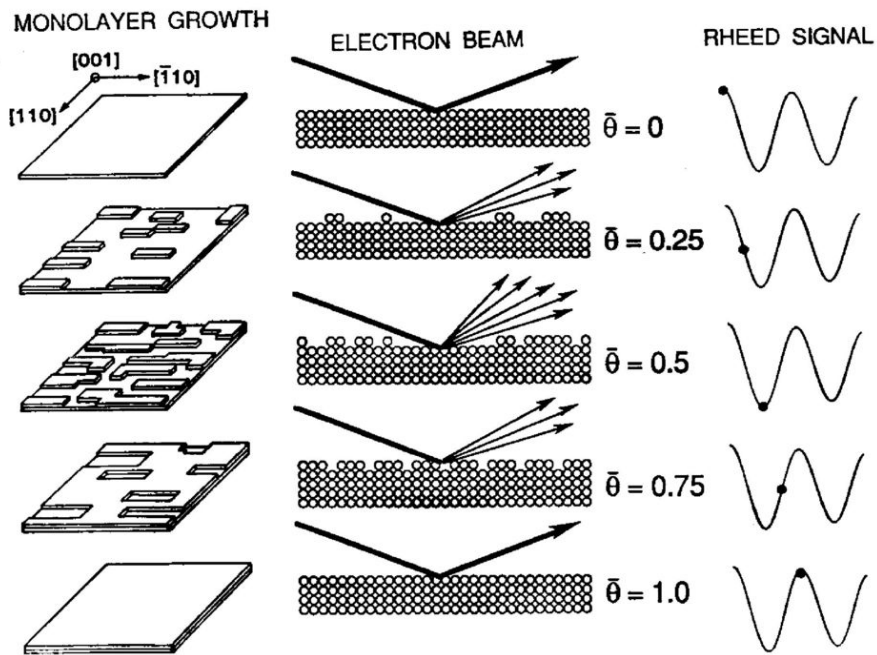
Figure 2.8 Mechanism for thickness monitor from RHEED intensity. Reprinted from [64] ©1992 with permission from Elsevier.
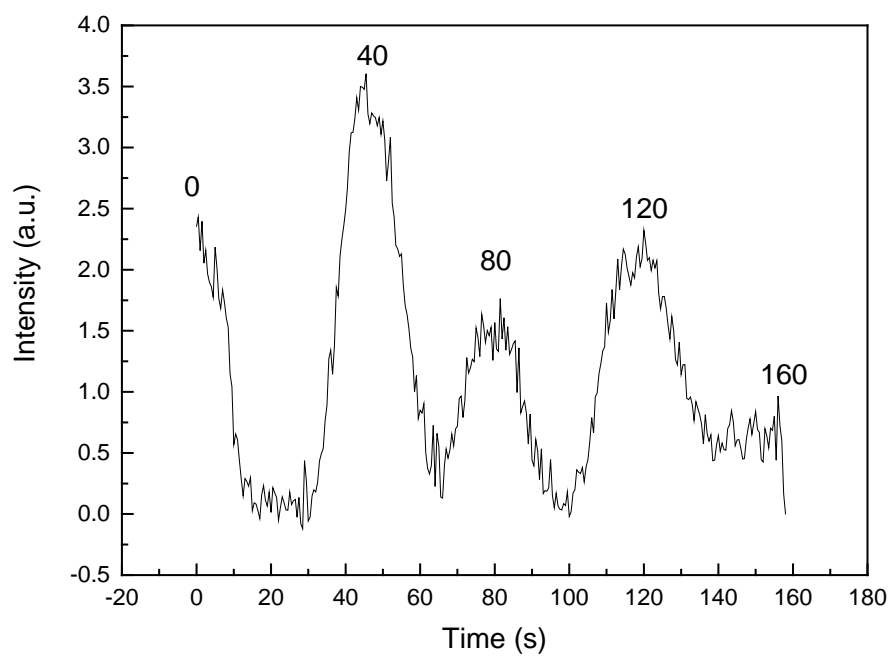
Figure 2.9 An example of real-time thickness monitor by RHEED intensity oscillation for a 4 ML sample.

2.3.2 Magnetic property measurement

2.3.2.1 Vibrating sample magnetometer
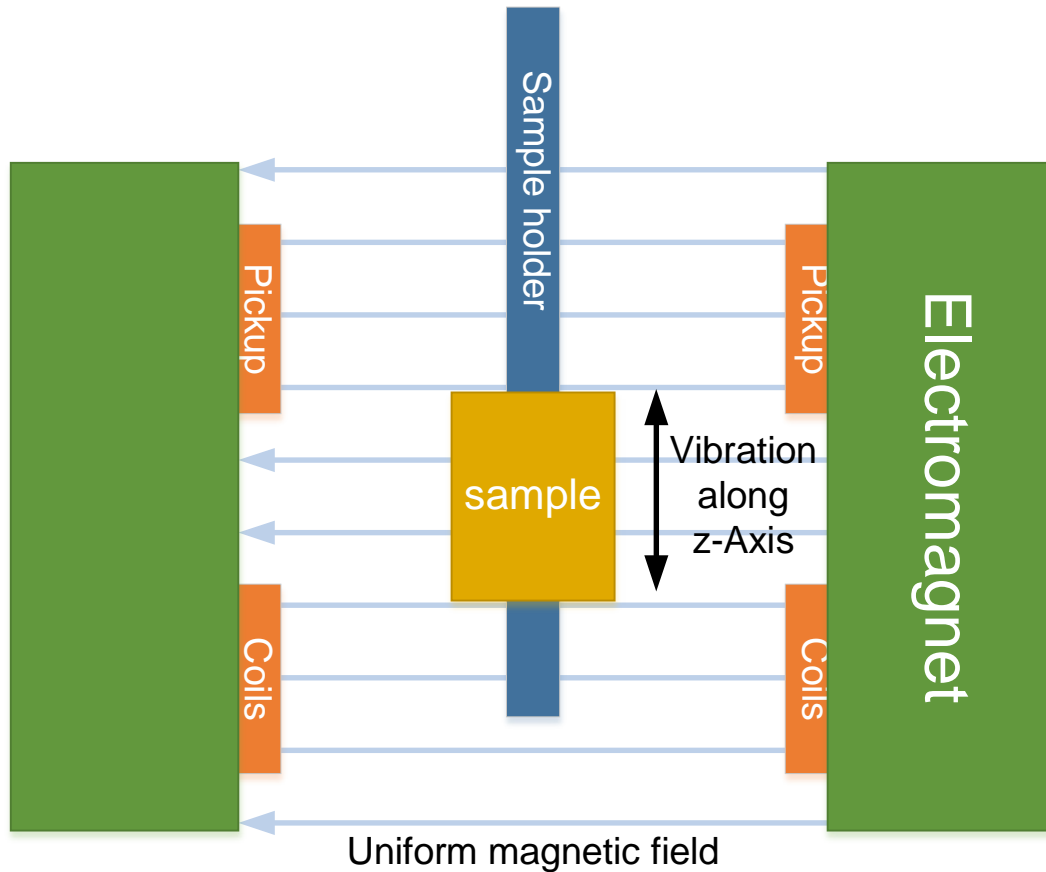
Figure 2.10 A schematic illustration for sample measured in a VSM system.

The vibrating sample magnetometer (VSM) is the most common facility in magnetism and spintronic research, which was invented in 1955 by Simon Foner at Lincoln Laboratory MIT to measure magnetic properties. A sample should be placed at the center point of uniform magnetic field, and the sample will be vibrated sinusoidally to induce voltage on the pickup coil, which is proportional to the sample's magnetic moment. The induced voltage is given as:

$$V_{induced} = \frac{d\phi}{dt} = \left(\frac{d\phi}{dz}\right)\left(\frac{dz}{dt}\right)$$ 2.1

Where the ϕ is the magnetic flux enclosed by the coil, z is the vertical position of the sample with respect to the coil, and t is time. The oscillation magnetic field of the moving sample induces an alternating electromotive force (emf) in the pickup coils, whose magnitude is proportional to the magnetic moment of the sample. And the alternating emf is amplified by a lock-in amplifier to make sure it is only sensitive to signals at the vibration frequency.

Figure 2.10 is a typical scheme illustration of the measurement zone. And Figure 2.11 is the picture of the VSM machine used in this study.
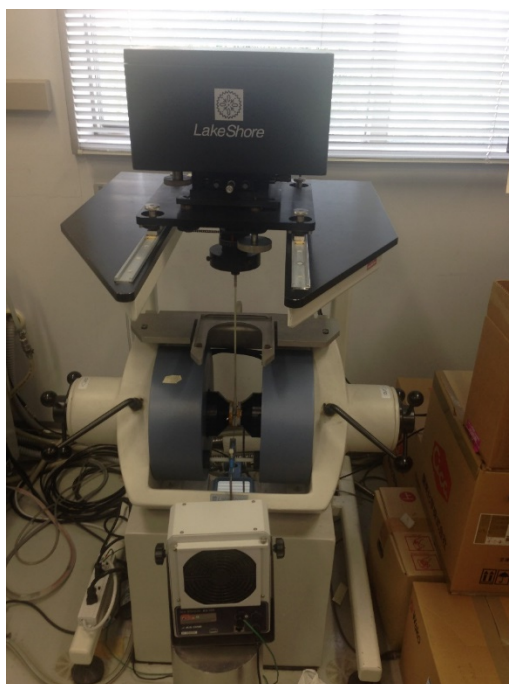
Figure 2.11 VSM used in this study

In this study, the target layer of prepared samples for evaluation is ultrathin, normally less than 1 nm, with comparable weak signal as the moment strength is not strong enough. In this case, a small position change by sample installation will introduce a significant measurement error. Thus, a careful calibration method using Ni standard film is used with continuous in-plane and out-of-plane measurement.
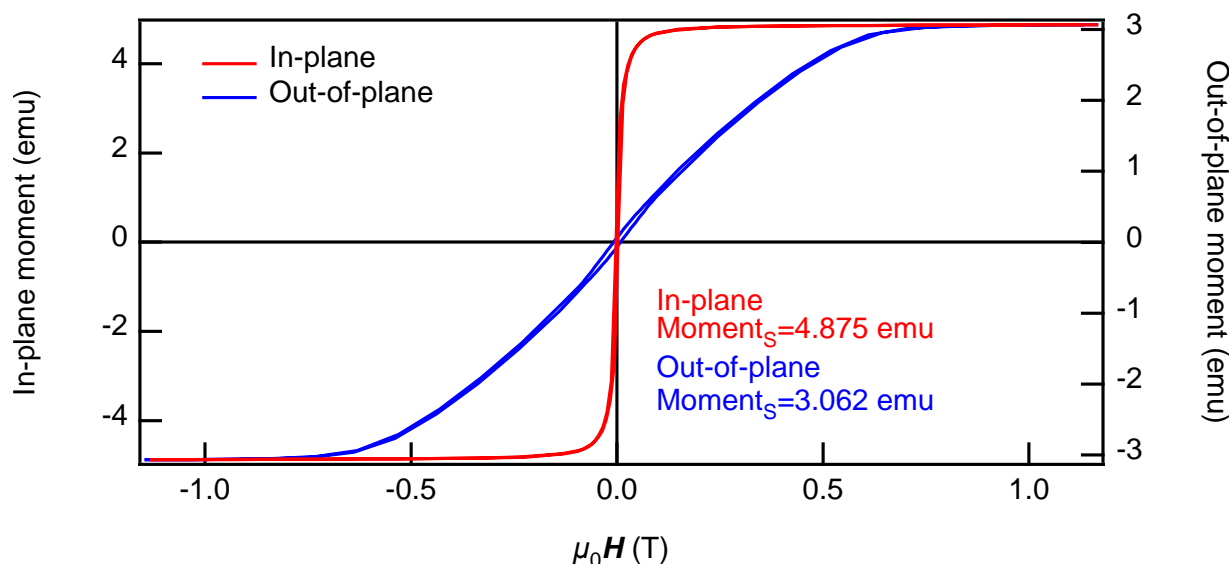
Figure 2.12 Magnetization curves for a standard Ni sample with external field in-plane(red) or out-of-plane(blue) to the film direction.

Figure 2.12 shows the *M-H* curves for a standard Ni thin film measured at in-plane and out-of-plane directions continuously, with only rotating the stage to change the measurement direction. Due to the spatial distribution, even a same sample will generate different induced voltages due to the measurement direction. In Ni standard sample case, the in-plane saturation moment is calibrated by its weight, density and standard

magnetization value. As the sample is saturated at both directions, the out-of-plane saturation moment should be as same as in-plane one. Thus, a calibration factor for measurement of out-of-plane direction can be obtained by $c = 4.875/3.062 \approx 1.6$. By this way, only one calibration measurement is required before a complete measurement of both in-plane and out-of-plane direction, with the minimalized sample spatial distribution.

2.3.2.2 Superconducting quantum interference device

In this study, the maximum field of a VSM can provide is limited to 2T, and VSM can only work for room temperature. Thus, for large field and low temperature magnetic property evolution, A Superconducting quantum interference device (SQUID) is used. A SQUID is a very sensitive magnetometer which can be used to measure extremely subtle magnetic fields, based on superconducting loops containing Josephson junctions. It is possible to measure small samples over a broad range temperature and magnetic field. There are two main types of SQUID: one is direct current, and another is radio frequency. Generally, the DC type shows a high sensitivity but low tolerance to disturbance while the RF type is opposite. In this study, a RF-SQUID was used. When the magnetic field through the superconducting rings, the current passes through the Josephson junction is:

$$I_c = \frac{\phi_{ex} - \phi}{L_S \sin\left(\frac{2\pi\phi}{\phi_0}\right)}$$

2.2

where, ϕ is the magnetic flux through the superconducting ring, ϕ_{ex} is the external magnetic flux, ϕ_0 is the fluxoid of 2.0×10^{-7} emu/cm, and L_S is the self-inductance of the superconducting ring.
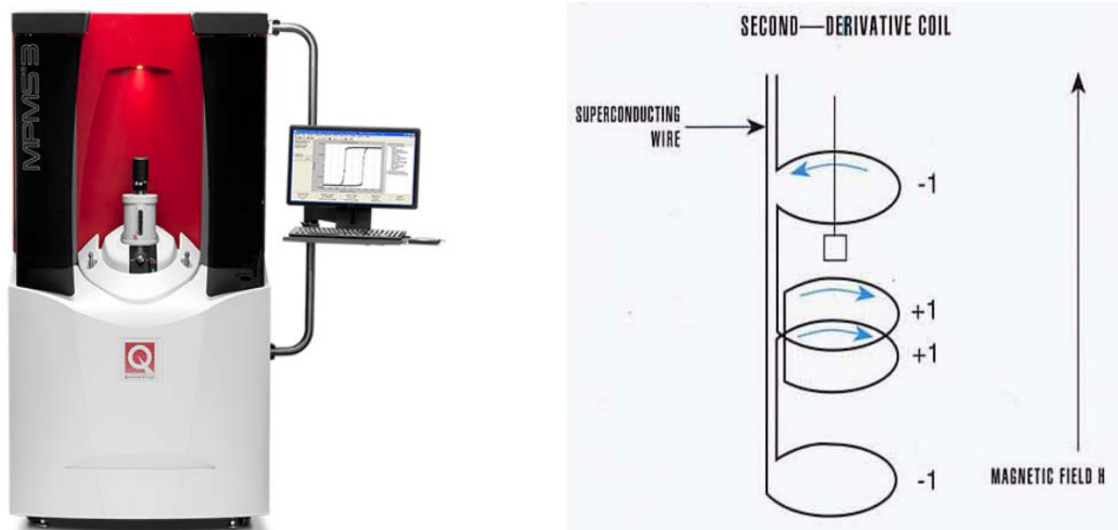
Figure 2.13 a) SQUID used in this study, b) the coil to detect magnetic moment. Adapt from Quantum Design[65].

On the other hand, since the magnetization of the sample can be evaluation by VSM exactly with calibration from easy axis measurement direction, the measurements using a SQUID is more focusing on the capture of the **M-H** curve, with normalized magnetization instead of accurate values.

2.3.3   Transport property measurement

How the transport property of magnetic structures can be modulated by the magnetization is the fundamental issue of spintronics. Especially for the magnetic memories, the magnetoresistance behavior with various conditions is a major topic. In this study, a 4-probe measurement is performed on prepared MTJs. For large field and low temperature conditions, the measurement is performed using a physic Physical Property Measurement System

2.3.3.1 4-probe DC measurement

As the MR is measured through the probe contact, then a 4-probe contact leads to a result ignoring the contact resistance. Thus, the resistance change can be more accurate detected.
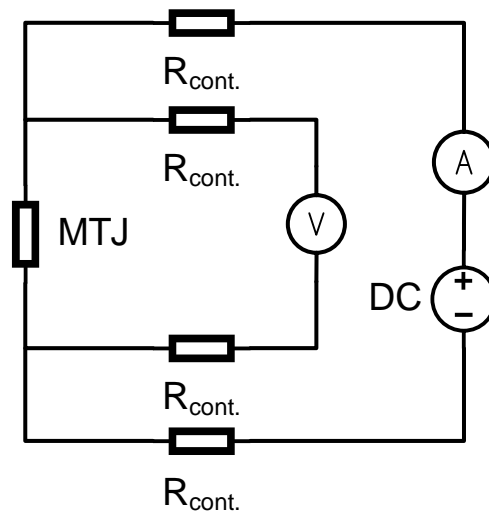
Figure 2.14 A typical 4-contact circuit with DC current source.

2.3.3.2 PPMS

PPMS is a system can provide large magnetic field with various corelated angel with measured sample under various measurement temperature with a 4-contact measurement setup.
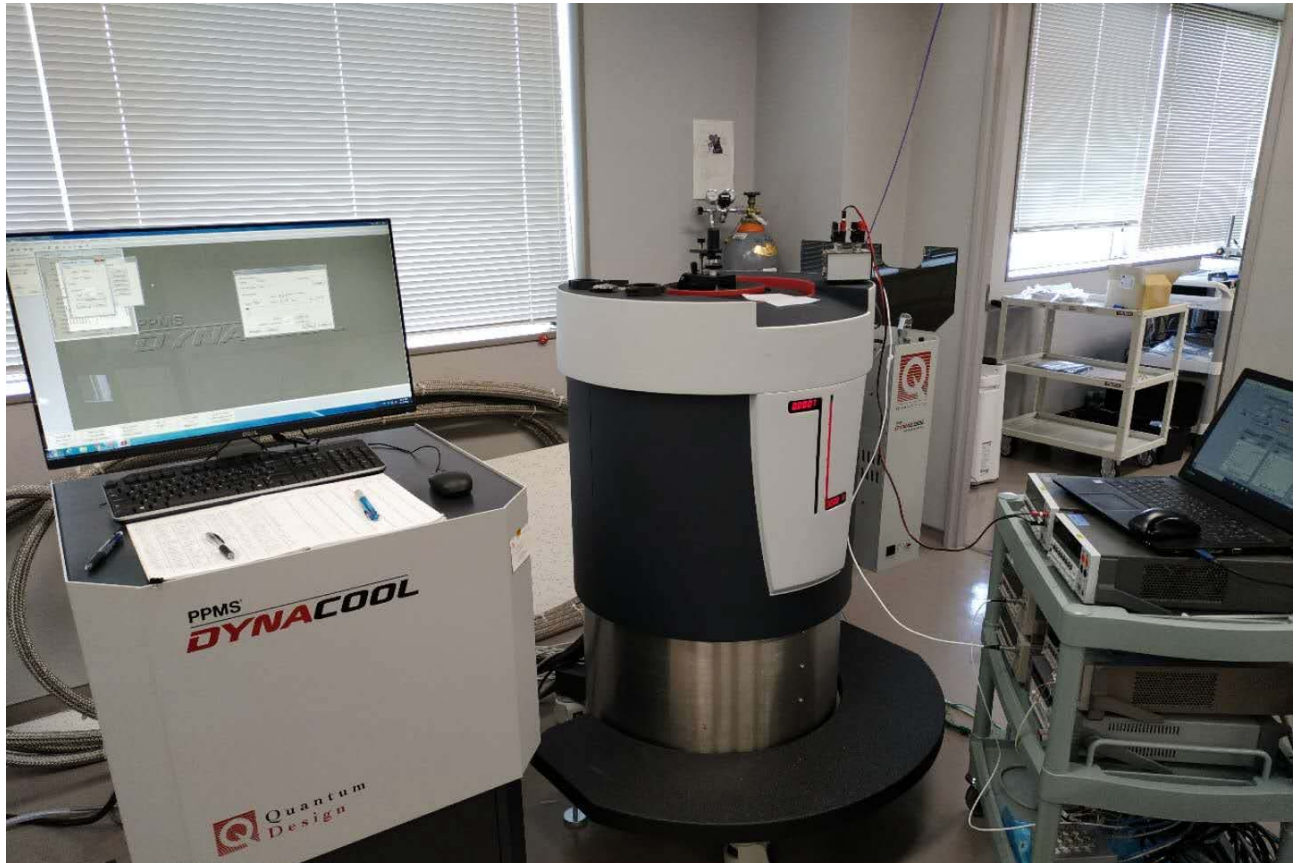
Figure 2.15 PPMS system used in this study.

Chapter 3   Nonlinear VMCA behavior observed in Fe/MgO/Fe MTJs

3.1   Introduction

The voltage-controlled magnetic anisotropy (VCMA), also known as electric field effect on magnetic anisotropy, in ferromagnetic metal layers attracts much interest in recent years [15,56,59,62,66–84]. This technology can help to realize low-power magnetization switching in devices, which is a key to next generation magnetic random-access memories (MRAMs). In fact, by using the VCMA, direct manipulation of magnetization by voltage pulse [57,85,86] and assistance to spin transfer torque(STT) switching[58,60] have been demonstrated.

Cr-buffered Fe/MgO heterostructures are of particular importance in perpendicular magnetic anisotropy[51,84,87] (PMA) and relevant studies, and *Nozaki et al*. have recently achieved a remarkable progress in the VCMA study using magnetic tunnel junctions (MTJs) with the Cr/Fe/MgO structure [72]. First, a very large interface PMA was predicted for the Cr/Fe/MgO structure by *ab initio* calculations[52,88], followed by an experimental demonstration of PMA of ~1.4 MJ/m^3 (~1000 µJ/m^2 for areal energy density) in previous studies[51,89]. Then, *Nozaki et al*. successfully reproduced such a large PMA in their MTJs including the Cr/Fe/MgO structure, so that its VCMA was examined. The VCMA coefficient obtained for the PMA reached 290 fJ/Vm[84]. However, those sample with large VCMA coefficient always show nonlinearity meanwhile as Figure 3.1[84] shows.
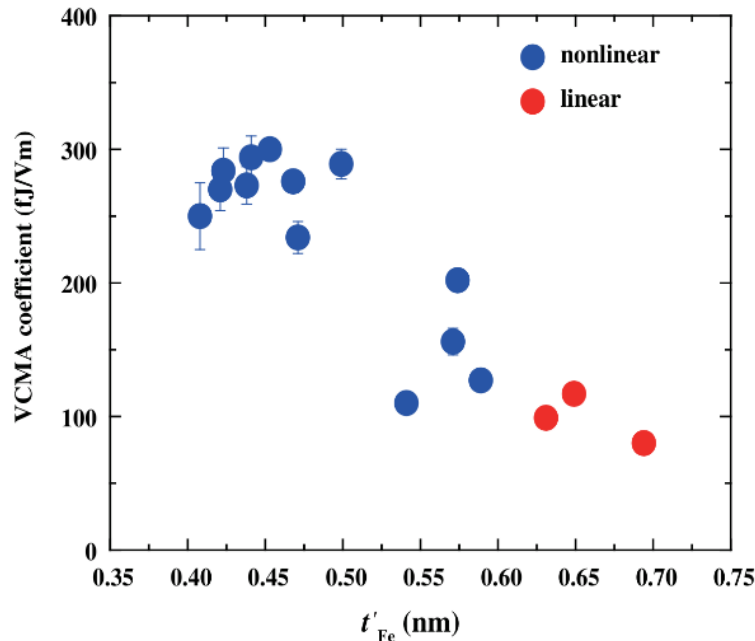
Figure 3.1 VCMA coefficient in ultrathin-Fe/MgO with various t_{Fe}. Those with large VCMA coefficients show nonlinearity also. Reprinted with permission from [84]. Copyright (2016) by the American Physical Society.

The mechanism of the large VCMA in Cr/Fe/MgO has not been well understood, although *ab initio*

studies have described the effect of charge accumulation and depletion at the interface that affects the spin-dependent screening and electron's occupancy of 3d orbitals[89,90]. Furthermore, an open question is the nonlinear behavior observed unexpectedly in the electric field dependence of PMA energy density[84]. Since it appears to be a unique feature for the VCMA coefficient more than 200 fJ/Vm, the nonlinear behavior could be a key to develop further large VCMA. At the same time, one may wonder if the nonlinearity can be associated with possible sample-to-sample variation, since no theoretical explanation has been provided. As Cr diffusion into the Fe layer (also into the Fe/MgO interface region) and possible interface contamination with carbon and/or oxygen are somehow discussed in Ref. [84], it may be difficult to obtain the well-defined Fe/MgO interface repeatedly and systematically.

In this experiment, I examined the VCMA in Cr/Fe/MgO under different conditions, i.e., temperature for annealing the structure and temperature of the VCMA measurement, to confirm the presence of the nonlinear VCMA behavior occurring characteristically in the Cr/Fe/MgO with a large VCMA coefficient. The nonlinear VCMA that was obtained together with a large areal PMA energy of ~600 μJ/m^2 and a large VCMA coefficient of more than 200 fJ/Vm gave rise to a local minimum at around 100 mV/nm in the VCMA curves, being independent of both the post-annealing temperature (i.e., interface quality) and the measurement temperatures. The results insensitive to the interface quality and the measurement conditions suggest that the nonlinear VCMA has an intrinsic origin such as a basic feature of the interface electronic structure.

3.2 Experiment
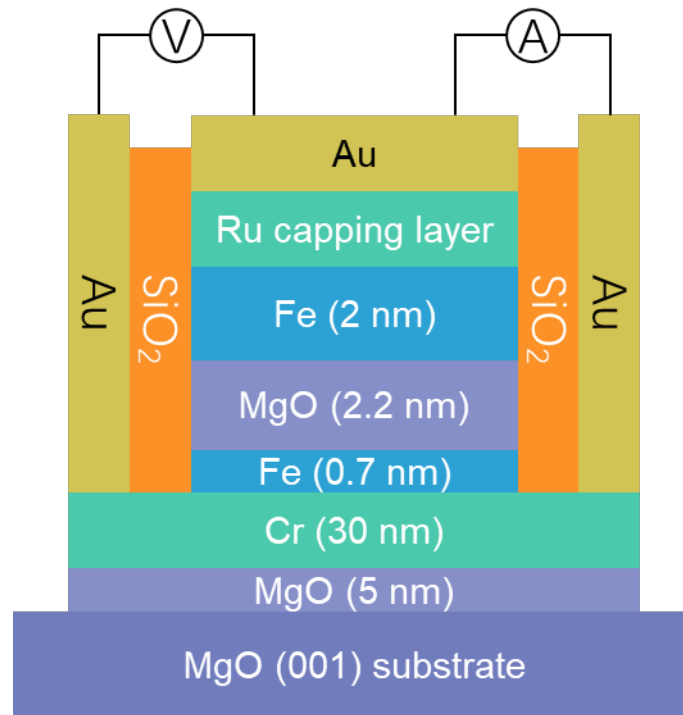
Figure 3.2 Schematic illustration of epitaxial magnetic tunnel junctions of Fe/MgO/Fe in this study.

In this study, MTJs based on Cr/Fe/MgO/Fe structure is prepared. Figure 3.2 shows a schematic design of the MTJ used in this experiment. A fully epitaxial stack of MgO (5 nm)/Cr (30 nm)/Fe (0.7 nm)/MgO (2.2 nm)/Fe (2 nm)/Ru (15 nm) was deposited on a MgO (001) substrate by electron beam evaporation, while, the capping Ru is deposited by sputtering. The bottom 0.7 nm Fe layer is the free layer to respond the voltage effect with different PMA energy density, while the 2 nm top Fe layer with in-plane magnetization is the reference layer to quantitatively evaluate the VCMA effect. Here, the thickness of the bottom (free) Fe layer t_{Fe} corresponds to five monolayers of bcc-Fe (001). At the beginning, the substrate was annealed at 800°C to clean its surface, followed by the deposition of a 5 nm MgO seed layer at 450°C. A Cr buffer layer was deposited at 150°C, and then was post-annealed at 800°C to obtain a flat Cr (001) surface. This crucial post-annealing temperature is critical to obtain large PMA for an ultrathin Fe layer deposited on the Cr buffer.
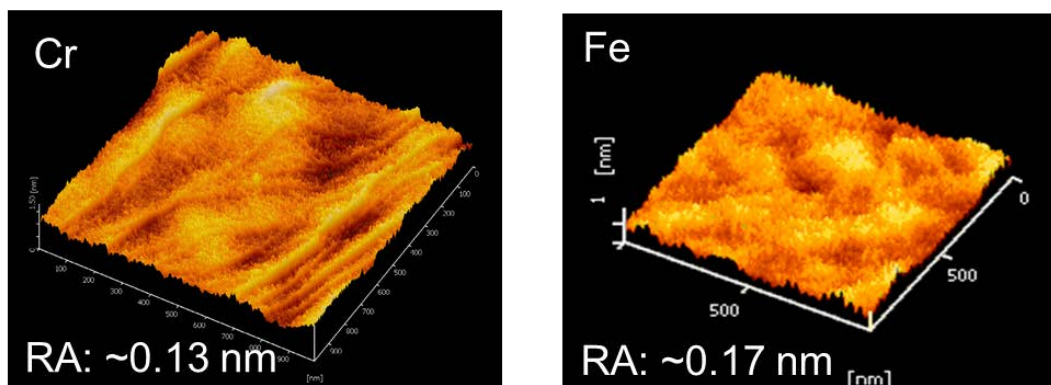
Figure 3.3 AFM images for a) Cr with terrace surface after 800°C annealing b) ultrathin-Fe grown on Cr.

52

The conditions used for the ultrathin Fe were 150°C for growth and 250°C for post-annealing to improve the surface flatness. Then, the MgO barrier layer was deposited at 150°C, followed with post-annealing at different temperatures (325°C, 350°C, 375°C, and 400°C) to modify the Fe/MgO interface conditions. The reference Fe layer was deposited at 150°C without post-annealing. Finally, a Ru capping layer was sputter-deposited at room temperature (RT). Through the growth process, surface structures and epitaxial growth were monitored by reflection high-energy electron diffraction (RHEED). The MTJ multilayer stacks prepared were patterned into a 5×10 μm^2 elliptical shape by using photo-lithography, Ar ion-beam milling and lift-off processes. The tunnel magnetoresistance (TMR) ratio was measured using the physical property measurement system (PPMS) under an in-plane external magnetic field at RT and low temperatures. The positive sign of applied voltage was defined as the polarity corresponding to the current flow from the top to bottom Fe electrode. The typical resistance-area product (RA) of the MTJs was the order of 10^4 Ωμm^2. Separately, the magnetization curve of the ultrathin Fe layer was characterized by using a vibrating sample magnetometer to determine the saturation magnetization (M_s).
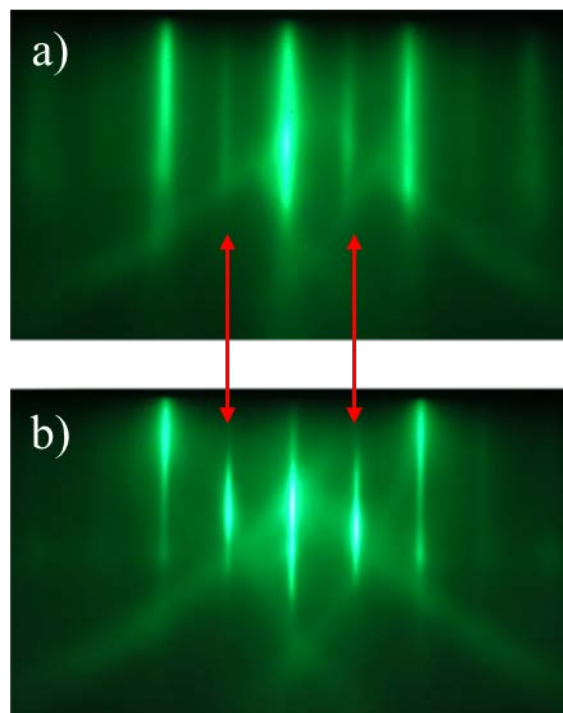
Figure 3.4 RHEED patterns taken for the surfaces of (a) ultrathin Fe and (b) Cr buffer layers. The incident electron beams are along the [100] azimuth of MgO (001) substrate. Sub-streaks indicated by red arrows correspond to a c(2×2) surface structure.

Figure 3.4(a) and (b) show the RHEED patterns of the ultrathin Fe (0.7 nm) and the Cr buffer layers with the incident electron beam parallel to the [100] azimuth of the MgO(001) substrate. Formation of c(2×2) surface structure is observed for both the Cr and Fe surfaces, as the additional streaks pointed by red arrows. Such a surface structure may improve the surface flatness and the magnitude of PMA of the ultrathin Fe layer.[51] In addition, it is noted that the absence of the c(2×2) structure for Fe was reported in Ref.[84], in contrast to the present study.

3.1 Results and discussion

3.1.1 Annealing temperature dependence for VCMA

Figure 3.5 shows a full TMR curve of a prepared MTJ annealed at 400 °C in the in-plane magnetic field (H_{ex}). Due to the small shape magnetic anisotropy energy of the ultrathin Fe layer and the sufficiently large interface PMA induced at the Fe/MgO interface, the easy axis of the ultrathin Fe layer is aligned perpendicular to the film plane; meanwhile, the top Fe layer has an easy axis parallel to the film plane. This orthogonal-easy-axis design enables us to electrically detect the rotation of the magnetization in the ultrathin Fe layer by applying an H_{ex} [62]. As described in Figure 3.5, the two Fe layers take the orthogonal magnetization configuration at $H_{ex} = 0$, which brings about a high tunnel resistance state of the MTJ. By applying a H_{ex}, the magnetization of the top Fe layer (reference layer) immediately turns parallel to the H_{ex} due to its in-plane magnetic anisotropy and small in-plane coercivity ($<$a few Oe), i.e., the magnetization of the top layer is almost always parallel to the H_{ex} direction. On the other hand, the magnetization of the bottom Fe layer (free layer) gradually tilts and finally becomes parallel to the H_{ex} direction when the H_{ex} reaches the anisotropy field of the bottom Fe layer (H_k). Therefore, the TMR curve reflects the magnetization process of the free Fe layer, i.e., the tunnel resistance takes the maximum at $H_{ex} = 0$ (orthogonal magnetization configuration) and gradually decreases down to the minimum with the increase of |H_{ex}| (parallel magnetization configuration). The TMR ratio in Figure 3.5 corresponds to a half of the whole TMR change between parallel and antiparallel magnetization configurations.
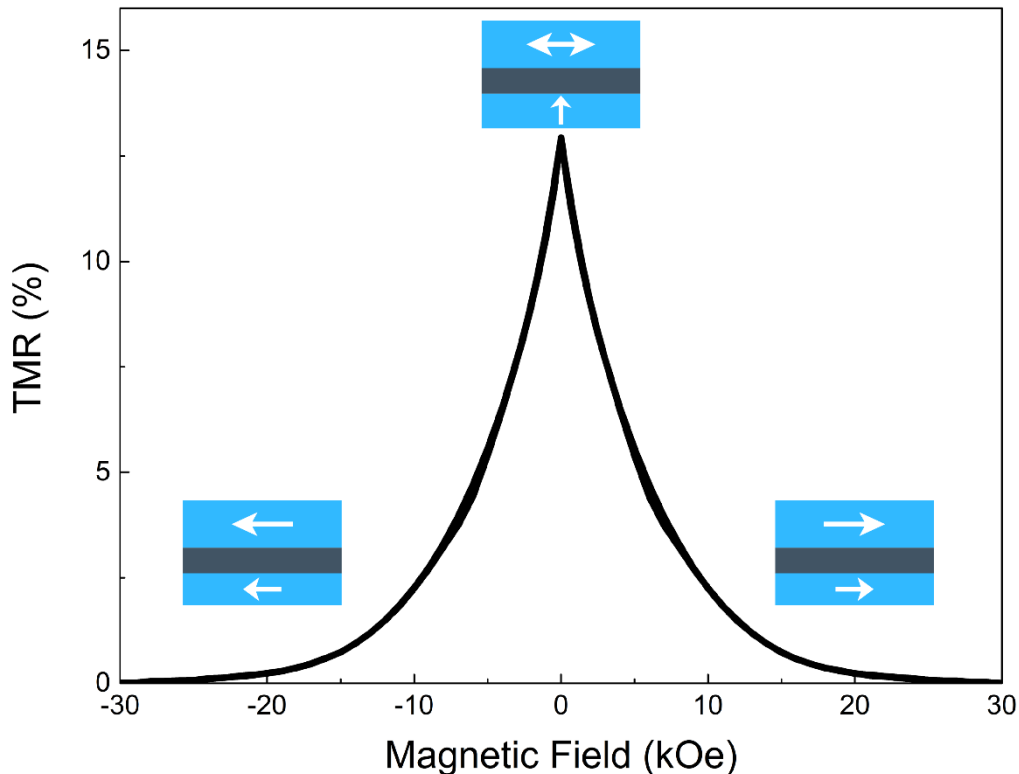
Figure 3.5. A typical TMR curve for the MTJ with annealing temperature of 400°C

Figure 3.6 shows the normalized TMR curves in the negative H_{ex} region for MTJs annealed at different temperatures. The TMR ratio is normalized by using the maximum (at $H_{ex} = 0$) and minimum (at $H_{ex} > H_k$) values, respectively. In the TMR curves, one can clearly see that the saturation behavior changes with the annealing temperature. This means that H_k strongly depends on the annealing temperature, indicating that the annealing process governs the Fe/MgO interface conditions that determine the PMA characteristics.

From the normalized TMR curves, we can evaluate the effective PMA energy density (K_{eff}), including the contribution of the shape magnetic anisotropy, as follows: the tunnel resistance is given by the relative angle between the magnetizations of the free and reference magnetic layers. In the sample design, the maximum resistance occurs at the 90° configurations (R_{90} at $H_{ex} = 0$), while the minimum resistance does in the parallel configuration (R_p at $H_{ex} = H_k$). The resistance at a given relative angle is expressed as [84]:

$$R(\theta) = \frac{R_{90}R_p}{R_p + (R_{90} - R_p) \cdot \cos\theta} \qquad 3.1$$

Since the magnetization direction of the top Fe layer is considered to be parallel to H_{ex} (i.e., in-pane direction), the ratio of the in-plane component of the magnetization $M_{in\text{-}plane}$ to its saturation magnetization M_s in the bottom ultrathin Fe layer can be determined as:

$$\frac{M_{in-plane}}{M_s} = \cos\theta = \frac{R_{90} - R(\theta)}{R(\theta)} \frac{R_p}{R_{90} - R_p} \qquad 3.2$$

The $M_{in\text{-}plane}/M_s$ calculated from the observed TMR curve of the MTJ with post-annealing at 350°C is shown in the inset of Figure 3.6, as an example. The K_{eff} is finally obtained by calculating the product of the area of shadow region $A_{in\text{-}plane}$ and the M_s.
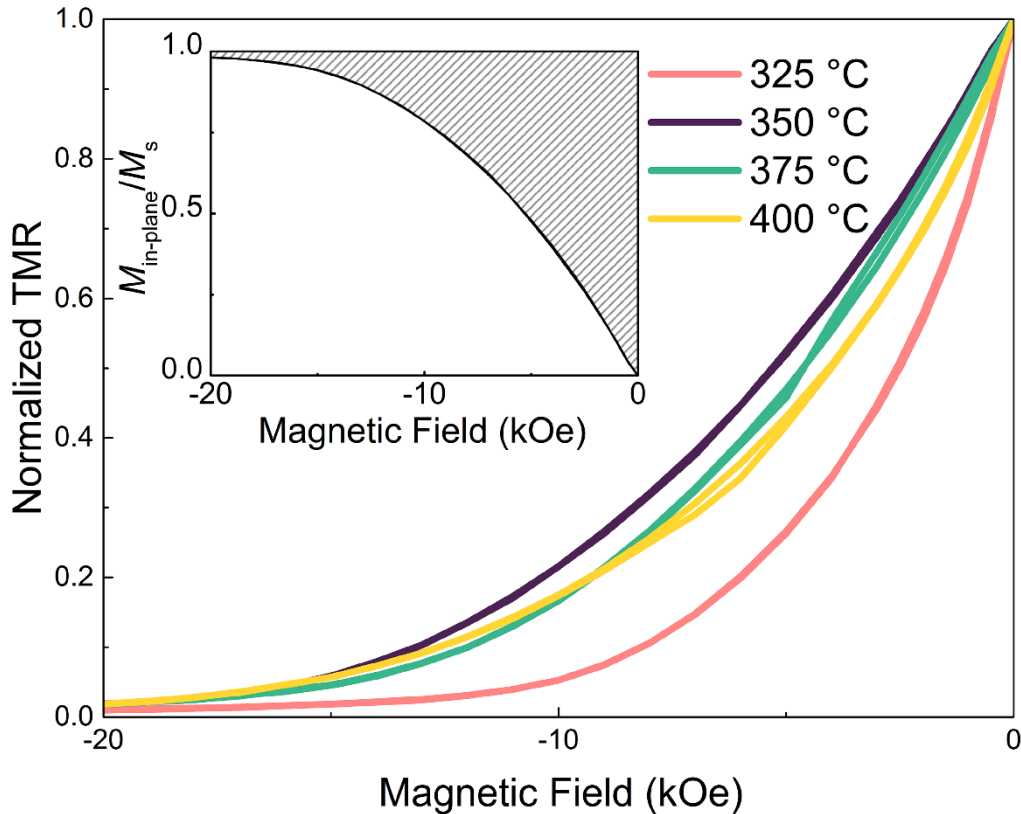
Figure 3.6 Normalized TMR curves for the MTJs with different annealing temperatures. The inset is an example of the in-plane component of magnetization (annealing temperature of 350°C), where the shadow area corresponds to the PMA energy density.
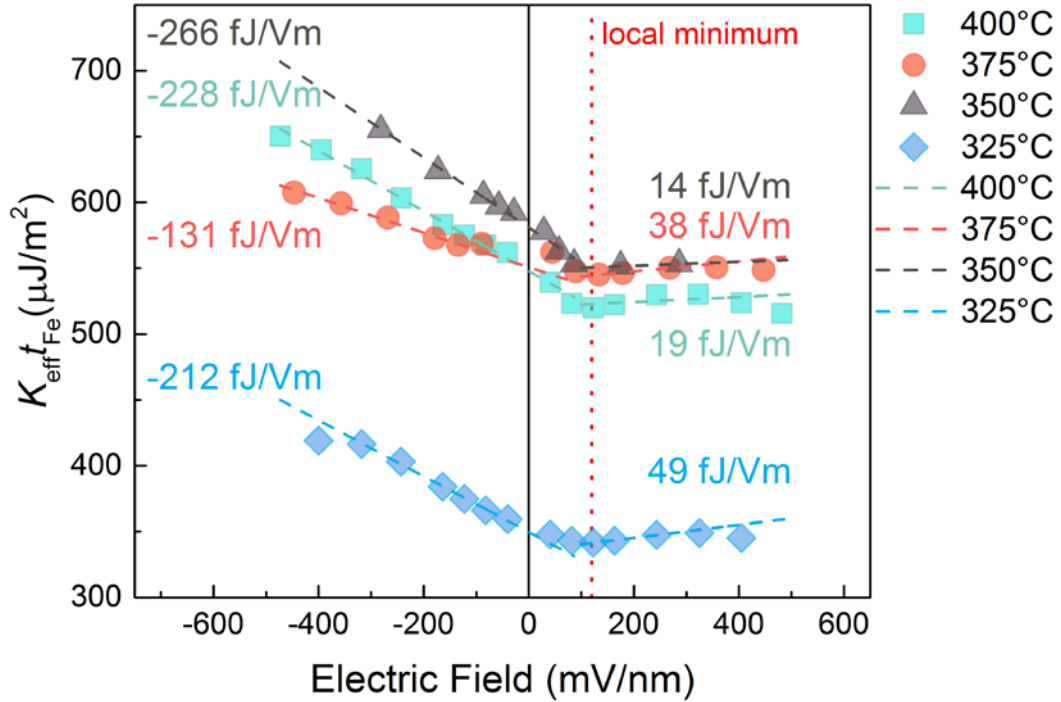
Figure 3.7. $K_{eff}t_{Fe}$ as a function of applied electric field E at RT for MTJs annealed at different temperatures. The dash line is the linear fitting. The dotted line indicates the position of the local minimum.

Figure 3.7 summarizes the areal PMA energy densities ($K_{eff}t_{Fe}$) as a function of the external electric field (E) measured at RT for MTJs with different annealing temperatures, where $t_{Fe} = 0.7$ nm and E is defined as the applied voltage divided by the thickness of the MgO barrier (=2.2 nm). The applied voltage range of -1000 to +1000 mV corresponds to the E range of -450 to +450 mV/nm. For all the MTJs, the E dependences of $K_{eff}t_{Fe}$ have a local minimum at around +100 mV/nm, which is indicated by the red dotted line in Figure 3.7. It is also found that $K_{eff}t_{Fe}$ varies almost linearly with E below and above the local minima. The linear fitting results were plotted for each MTJ (dashed line). The slope below the local minimum positions were in the range of -133 to -266 fJ/Vm. The values of the slopes are the so-called VCMA coefficient, and those observed in the present Fe/MgO interfaces are consistent with that reported in Ref. [84]. In the range of E above the local minima, the VCMA coefficients are much smaller than those below the local minima. Furthermore, it is a new finding in the present study that the local minimum position around +100 mV/nm is independent of the annealing temperature. This suggests that the nonlinear behavior is insensitive to the interface conditions, while the PMA energies and VCMA coefficients are very likely to depend on the interface conditions.

3.1.2   Measurement temperature dependence for VCMA

The appearance of the local minimum always observed at around +100 mV/nm despite the variation in the annealing temperature would be specific to the VCMA characteristics of Cr/Fe (0.7 nm)/MgO structures. To explore it further, the VCMA characteristics for the MTJ annealed at 400 °C was evaluated at low measurement temperatures. Figure 3.8 shows the $K_{eff}t_{Fe}$ as a function of E at 10, 100, 200 and 300 K, respectively. It is clearly seen that the $K_{eff}t_{Fe}$ increases with decreasing the measurement temperature. Interestingly, the local minimum positions (~ +100 mV/nm) are independent of the temperatures, while the nonlinearity becomes significant at lower temperatures. In addition, there might be a few fine structures, as implied by the faint peak at around -50 mV/nm, in the E dependence of $K_{eff}t_{Fe}$ at low temperatures.

As shown in Figure 3.7 and Figure 3.8, the nonlinear behavior, particularly the local minimum at around +100 mV/nm, has been found to be independent of both the annealing and measurement temperatures. The former temperature is likely to influence the interface conditions, and indeed the PMA and the VCMA coefficient vary with the annealing temperature. The latter temperature may be related with possible extrinsic effects such as an epitaxial strain induced in the MTJ and some kinds of artifacts. Thus, the observed insensitivity of the minimum position suggests that the nonlinear behavior is attributed to an intrinsic origin such as a basic feature of the electronic structure at the Fe/MgO interface. In fact, interface resonant states (IRSs) are formed in the minority spin band of the Fe/MgO system, and the IRSs may affect the transport properties in the Fe/MgO-based MTJs, as proposed by *Belashchenko et al.*[91]. The effect of IRSs on the VCMA at the Fe/MgO interface was also studied by means of *ab initio* calculations[92]. Thus, the results obtained are expected to contribute to the progress in theoretical studies, particularly in *ab initio* calculations on the mechanism of VCMA.
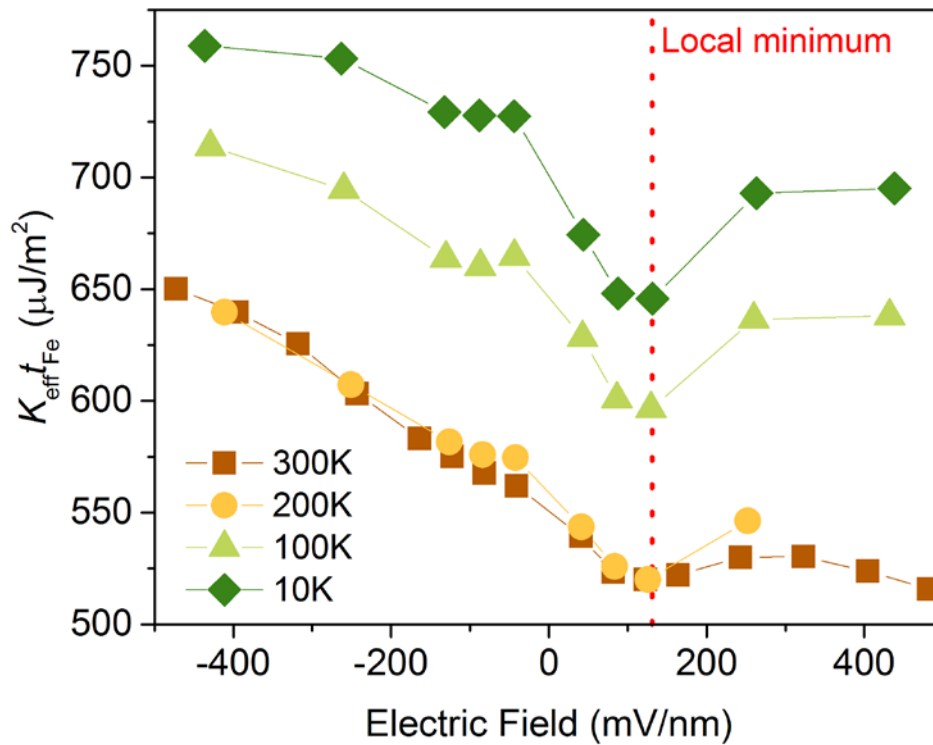
Figure 3.8 $K_{eff}\, t_{Fe}$ as a function of applied electric field E at different measurement temperatures. The annealing temperature of MTJ is 400 °C.

3.2 Summary

The nonlinear VCMA characteristics in orthogonally-magnetized MTJs with a Cr/Fe(0.7nm)/MgO structure was studied by evaluating post-annealing and measurement temperature dependences. A large VCMA coefficient of more than 200 fJ/Vm and a large areal PMA energy density of around 600 μJ/m^2 at RT were obtained at the 0.7-nm Fe/MgO interfaces. More interestingly, regardless of the post-annealing and measurement temperatures, a clear local minimum around +100 mV/nm was observed in the electric field dependence of magnetic anisotropy. The present results imply that the origin of the local minimum is attributed to an inherent electronic structure in the Cr/Fe/MgO.

Chapter 4 Large perpendicular anisotropy of ultrathin-Fe/MgAl₂O₄

4.1 Introduction

$MgAl_2O_4$ is considered a promising alternative barrier material to MgO for magnetic tunnel junctions (MTJs) due to its tunable lattice constant[36,93] and the Δ_1 band preferential transport due to the coherent tunneling effect.[11,12,34,35] Especially, a large tunnel magnetoresistance (TMR) ratio[93,94] and improved bias dependence of the TMR ratio[36,95] have been reported in $MgAl_2O_4$-based MTJs. In addition to such TMR properties, interface-induced perpendicular magnetic anisotropy (PMA) at an $MgAl_2O_4$ interface is a crucial property for applications of perpendicularly magnetized MTJs (p-MTJs). The utilization of perpendicularly magnetized films with a large PMA energy can substantially improve thermal stability of p-MTJs to ensure long data retention for next-generation high-density non-volatile magnetic memories such as spin-transfer-torque magnetoresistive random access memory (STT-MRAM) and magnetoelectric-RAM.[49,96,50,15,16,52,58,77,60,84,87] So far, the largest interface PMA energy density around 1.4 MJ/m³ has been reported in an epitaxial ultrathin-Fe/MgO(001) heterostructure.[51] For $MgAl_2O_4$ based epitaxial structures, smaller PMA energy density ~0.4 MJ/m³ has been experimentally reported in Fe/MgAl₂O₄(001)[97] and Co₂FeAl/MgAl₂O₄(001) heterostructures[98], where the $MgAl_2O_4$ layers were prepared by post-oxidization of an Mg-Al metallic layer.
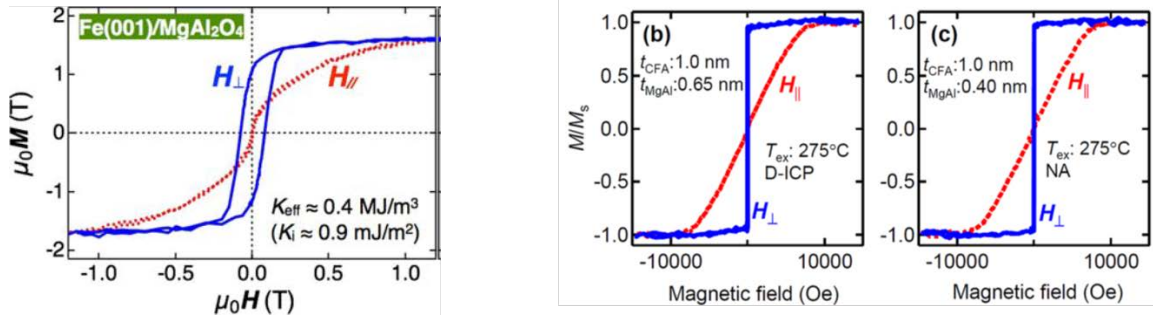
Figure 4.1 a) PMA obtained in Fe/MgAl₂O₄, reprinted from [97] with permission. Copyright © 2000 by John Wiley Sons, Inc. b-c) CoFeAl/ MgAl₂O₄ by post-oxidized MgAl alloy. Reproduced from [98] with the permission of AIP Publishing.

On the other hand, based on a recent theoretical calculation,[99] the areal PMA energy density of ~1.3 mJ/m² was predicted at an Fe/MgAl₂O₄(001) interface, which is nearly comparable to that at an Fe/MgO(001) interface (~1.5−1.7 mJ/m²). Interestingly, even the small difference in the PMA densities between Fe/MgAl₂O₄ and Fe/MgO was clearly interpreted through the second perturbation theory with the orbital resolved densities of states. Therefore, further improvement in the PMA energy of ultrathin-Fe/MgAl₂O₄(001) interfaces, i.e., observation of the intrinsically large PMA, is expected if a clean interface is obtained by suppressing atomic intermixing and over-oxidation through process optimization. In addition, related magnetic properties of the

PMA heterostructures such as magnetic damping and temperature dependence of PMA properties were evaluated: The former determines the switching speed and the current density for MRAM operations, and the latter guarantees the device operation temperature range of p-MTJs.[100,101]

System	$K_i\,(\mathrm{mJ/m^2})$	$E_{\mathrm{demag}}\,t\,(\mathrm{mJ/m^2})$	$K_{\mathrm{eff}}\,t\,(\mathrm{mJ/m^2})$
Fe/MgAl$_2$O$_4$	1.199	-0.893	0.306
Fe/MgO $(a = a_{\mathrm{MgO}}/\sqrt{2})$	1.467	-0.827	0.640
Fe/MgO $(a = a_{\mathrm{Fe}})$	1.715	-0.915	0.800

Figure 4.2 Calculated PMA energy density of Fe/MgO and Fe/MgAl$_2$O$_4$, reproduced from [99] with the permission of author.

4.2 Experiment

Figure 4.3 (a) shows a schematic design of the multilayer structure to examine the PMA properties at an Fe/$MgAl_2O_4$ interface. A fully epitaxial stack of MgO (5 nm)/Cr (30 nm)/Fe (t_{Fe} = 0.7 nm)/$MgAl_2O_4$ (t_{MAO} = 2 and 3 nm) was deposited on an MgO (001) substrate by EB evaporation (base pressure ~1×10^{-8} Pa). Before deposition, the substrate was annealed at 800°C to clean its surface, followed by the deposition of the 5 nm MgO seed layer at 450°C. The Cr buffer layer was deposited at 150°C, and then it was post-annealed at 800°C to obtain a flat Cr (001) surface. This post-annealing temperature is critical to obtain a large PMA for an ultrathin Fe layer deposited on the Cr buffer.[51] The temperature conditions for the ultrathin Fe were 150°C and 250°C for growth and post-annealing, respectively, to improve the surface flatness. Then, the $MgAl_2O_4$ barrier layer was deposited at 150°C with a ~0.01 nm/s deposition rate from a high-density (98.6% of the theoretical density) sintered $MgAl_2O_4$ chip (Ube Material Industries), instead of from an $MgAl_2O_4$ substrate as the previous report.[102] Although the barrier composition may slightly deviate from $MgAl_2O_4$ during the deposition,[102] in this study the notation "$MgAl_2O_4$" is used for simplicity. The deposited $MgAl_2O_4$ barrier was post-annealed at different temperatures (350°C, 400°C, 450°C, and 500°C) to modify the Fe/$MgAl_2O_4$ interface conditions. Finally, the 2 nm thick Ru capping layer was sputter-deposited at room temperature (RT). Through the growth process, surface structures and epitaxial growth were *in-situ* monitored by reflection high-energy electron diffraction (RHEED). Magnetic hysteresis loops (***M-H*** loops) of the samples were measured using a vibrating sample magnetometer (VSM) at RT and a vibrating sample magnetometer incorporated with superconducting quantum interference device (VSM-SQUID) under temperatures between 100 and 300 K. The ultrafast magnetization dynamics was measured by an all-optical TR-MOKE microscope to evaluate magnetic damping. The 1028 nm fundamental femtosecond laser pulse was used to excite the sample whereas the second-harmonic (wavelength, λ = 515 nm) of the fundamental beam was used to probe the magnetization dynamics by measuring the change in Kerr rotation as a function of time-delay between both pump and probe beams. A variable magnetic field was applied at an angle of 70° with respect to the perpendicular direction of the sample surface.

The RHEED patterns of the sample with an Fe (0.7 nm)/$MgAl_2O_4$ (3 nm) were shown in Figure 4.3. (b)-(g). As seen in Figure 4.3 (d) and (f), the additional sub-streaks indicated by red arrows represent the formation of the c(2×2) reconstructed surface of Cr and Fe, which is believed to improve the surface flatness and consequently the magnitude of PMA of the ultrathin Fe layer when capped with MgO.[51] It is noted that the absence of the c(2×2) structure for Fe was reported in Ref. [84], in contrast to the present study. Besides, as shown in Figs. 1 (b) and (c), the RHEED patterns of the $MgAl_2O_4$ surface after post-annealed at 400°C are similar to those of sputter-deposited $MgAl_2O_4$ on a thick Fe layer.[95] Therefore, the growth of a fully epitaxial structure with (001) orientation was confirmed. The patterns of the $MgAl_2O_4$ surface also indicate that the EB-evaporated $MgAl_2O_4$ in this study has a cation-disordered spinel structure, which ensures the giant TMR effect similar to an MgO barrier.[93,94]
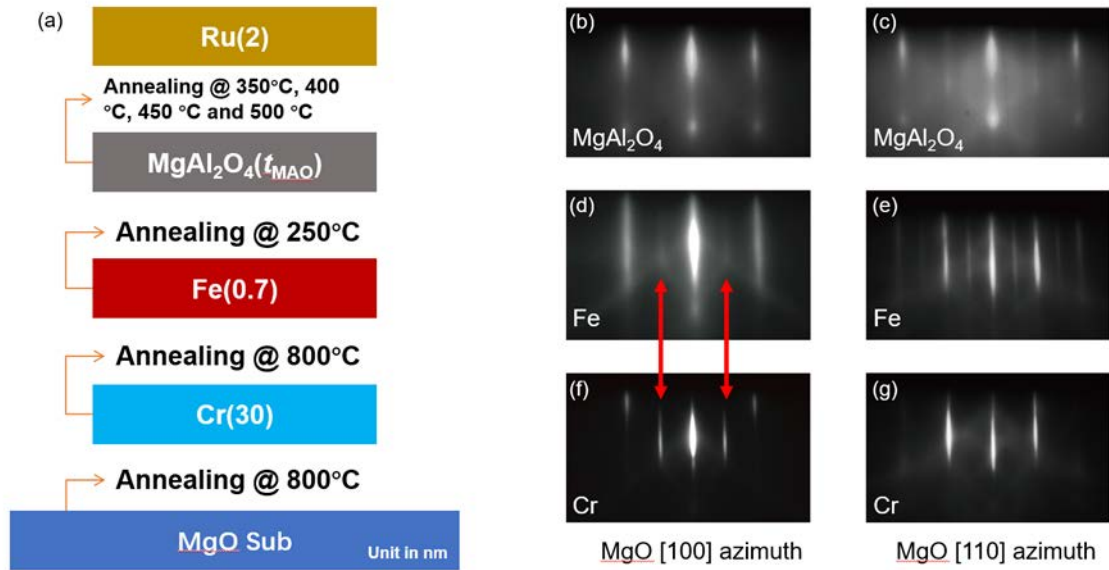
Figure 4.3 (a) Schematic illustration of an epitaxial heterostructure. (b)-(g) RHEED patterns taken from a sample of Fe (0.7 nm)/MgAl$_2$O$_4$ (3 nm) annealed at 400°C; (b), (d) and (f) The incident electron beams are along [100] azimuth of MgO (001) substrate and (c), (e) and (g) [110] azimuth. Sub-streaks indicated by red arrows correspond to c(2×2) surface structure.

4.3 Results and discussion

4.3.1 Annealing temperature dependence

The largest PMA energy density is obtained for Fe (0.7 nm)/MgAl$_2$O$_4$ (3 nm) with annealing temperature of 400°C. The **M-H** loops of this sample is shown in Figure 4.5 (a), where the effective PMA energy density, i.e., K_{eff}, was determined by the area enclosed by the in-plane, out-of-plane **M-H** loops, and the y-axis (shadow area). The largest K_{eff} reaches ~1.0 MJ/m^3, which is comparable to the value (~1.4 MJ/m^3) in the previous report for an Fe (0.7 nm)/MgO. Firstly, it should be noted that the K_{eff} observed in this study is more than twice as large as the reported in an Fe (0.7 nm)/MgAl$_2$O$_4$ (~ 0.4 MJ/m^3),[97] where the MgAl$_2$O$_4$ was prepared by post-plasma-oxidation of an Mg$_{33}$Al$_{67}$ metallic layer. Secondly, the large PMA which is close to but slightly smaller than that of Fe/MgO is in a good agreement with the theoretical predictions.[99] This fact strongly suggests that the first principles approach describes the mechanism of interface PMA of Fe/oxide correctly. Theoretical calculations also revealed that the over- or under-oxidation at the interface of a ferromagnetic layer and an oxide layer significantly reduces the magnitude of the PMA energy density.[52] Thus, EB-evaporated MgAl$_2$O$_4$ grown from high-density MgAl$_2$O$_4$ chips may have improved interface oxidation conditions compared to the post-oxidized MgAl$_2$O$_4$. It was suggested in Ref.[98] that uniform oxidation of a metal layer is not easy, which tends to cause over-oxidation or under-oxidation at the bottom-side barrier interface depending on the oxidation condition.
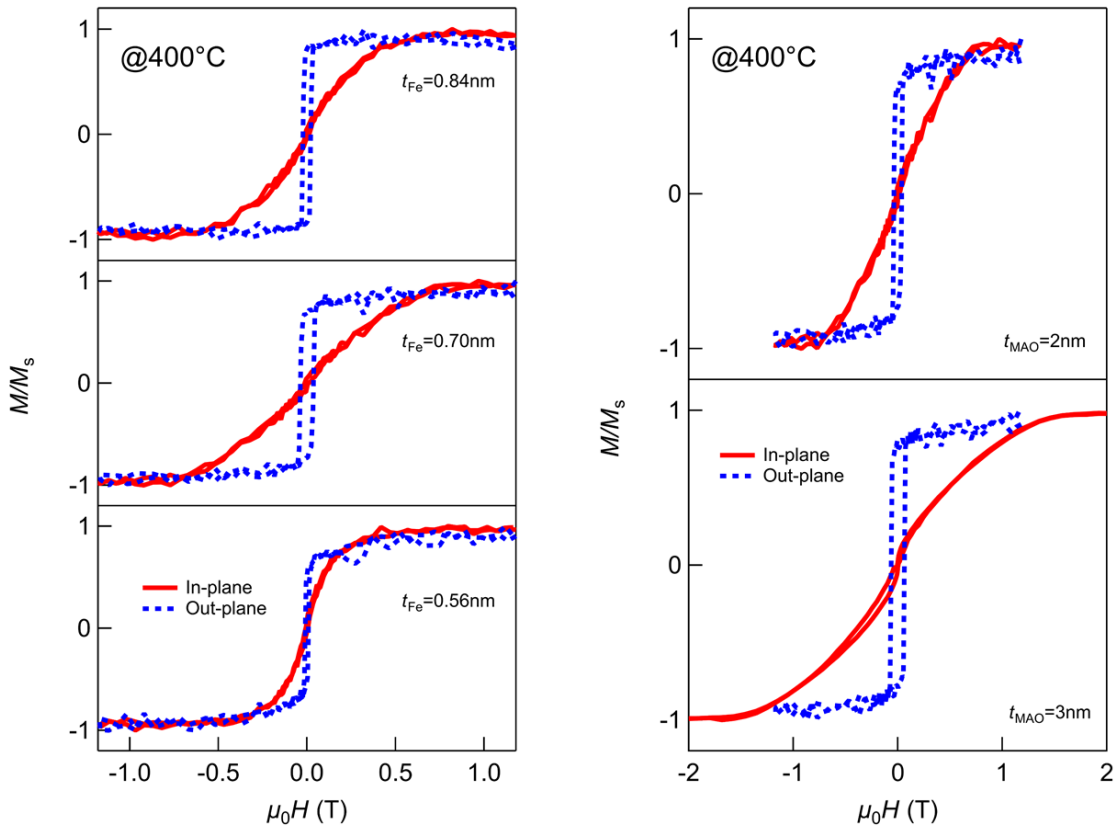
Figure 4.4 Annealing temperature dependence of PMA

By varying the MgAl$_2$O$_4$ thickness and post-annealing temperature, interface conditions, such as the degree of oxidation, can be tuned.[87] Figure 4.5 (b) shows K_{eff} as a function of the post-annealing temperature for t_{MAO} = 2 and 3 nm. The samples with t_{MAO} = 3 nm show larger PMA energy density than those with t_{MAO} = 2 nm at all post-annealing temperatures, which may be related to possible variation of oxygen amount near the Fe/MgAl$_2$O$_4$ interface by increasing the MgAl$_2$O$_4$ thickness. Moreover, the PMA retains even at 500°C for t_{MAO} = 3 nm, suggesting that the PMA of ultrathin-Fe/MgAl$_2$O$_4$ is robust enough to endure high-temperature heat treatments during industrial manufacturing.[103]
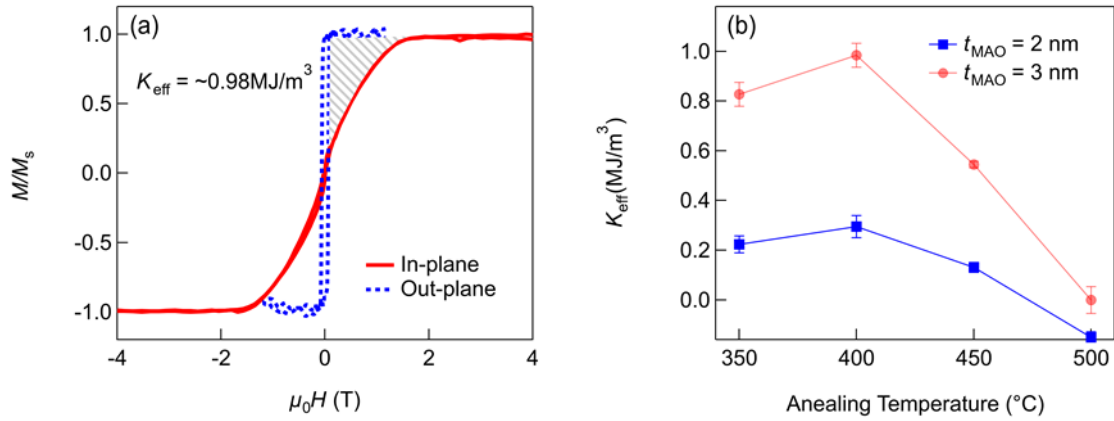
Figure 4.5 (a) **M-H** loops at RT for sample of Fe (0.7 nm)/MgAl$_2$O$_4$ (3 nm) annealed at 400°C. Shadow area indicates the effective PMA energy density (K_{eff}). Positive K_{eff} indicates PMA. (b) Annealing temperature dependence of K_{eff} for Fe (0.7 nm)/MgAl$_2$O$_4$ (2 or 3 nm).

4.3.2 Robustness of PMA
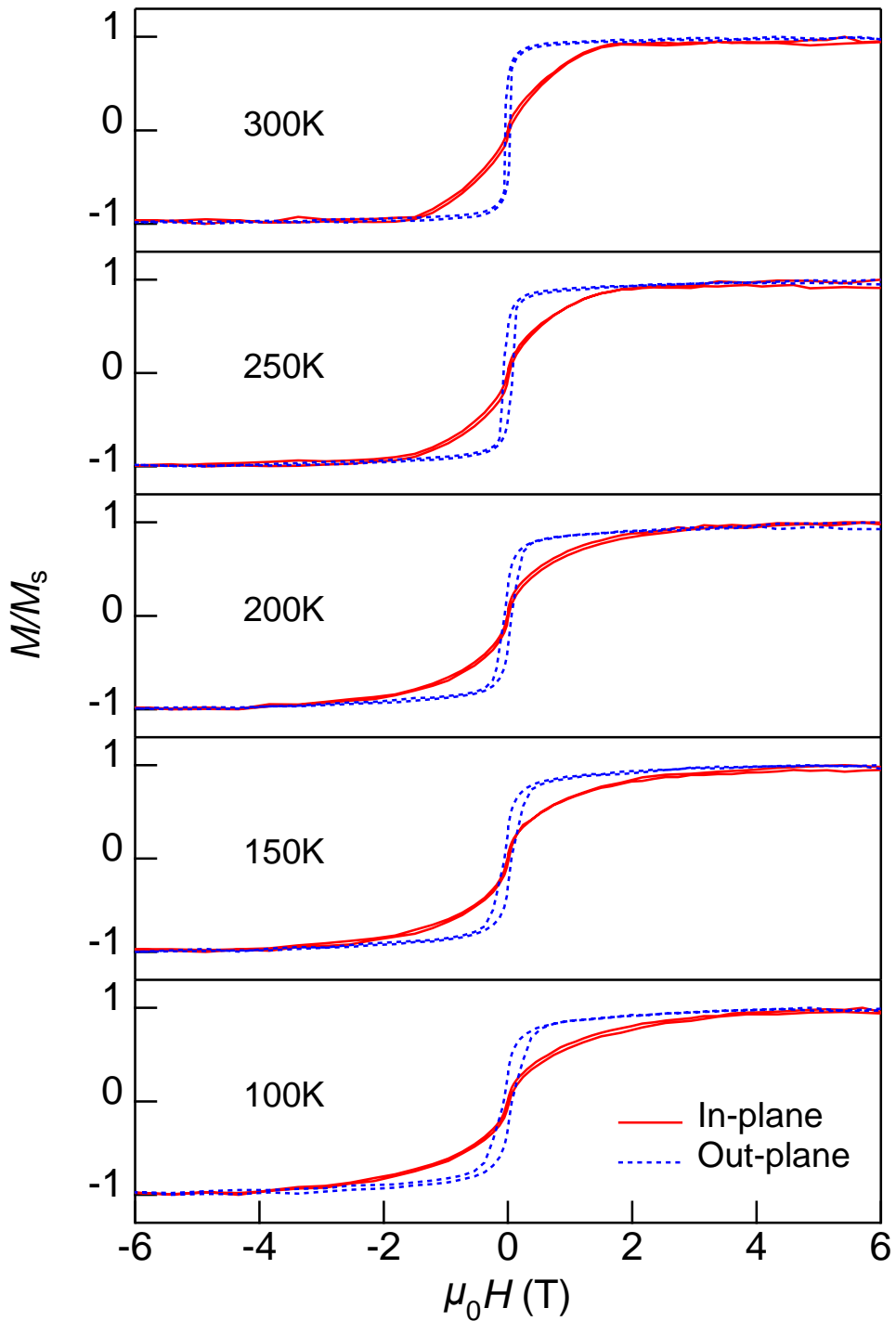
Figure 4.6 Normalized *M-H* loops under different measurement temperatures.

In addition to the magnitude of K_{eff}, weak temperature dependence of K_{eff} is also favorable for practical use of PMA heterostructures. To evaluate the temperature dependence of K_{eff}, the *M-H* loops of Fe (0.7 nm)/MgAl$_2$O$_4$ (3 nm) were investigated at different measurement temperatures between 300 K (RT) and 100 K, as shown in Figure 4.6. It is found that the shape of the in-plane (hard-axis) loops is significantly temperature

dependent. The anisotropy field of the in-plane loops (H_k) increases with decreasing temperature, indicating the enhancement of K_{eff} at low temperatures. To analyze the temperature dependence of magnetic properties, we firstly fitted the saturation magnetization M_s by Bloch's law: [104]

$$M_s(T) = M_s(0) \left[1 - \left(\frac{T}{T_c} \right)^{1.5} \right]$$

4.1

where $M_s(0)$ is M_s at 0 K, T is the absolute temperature, and T_c is the Curie temperature.
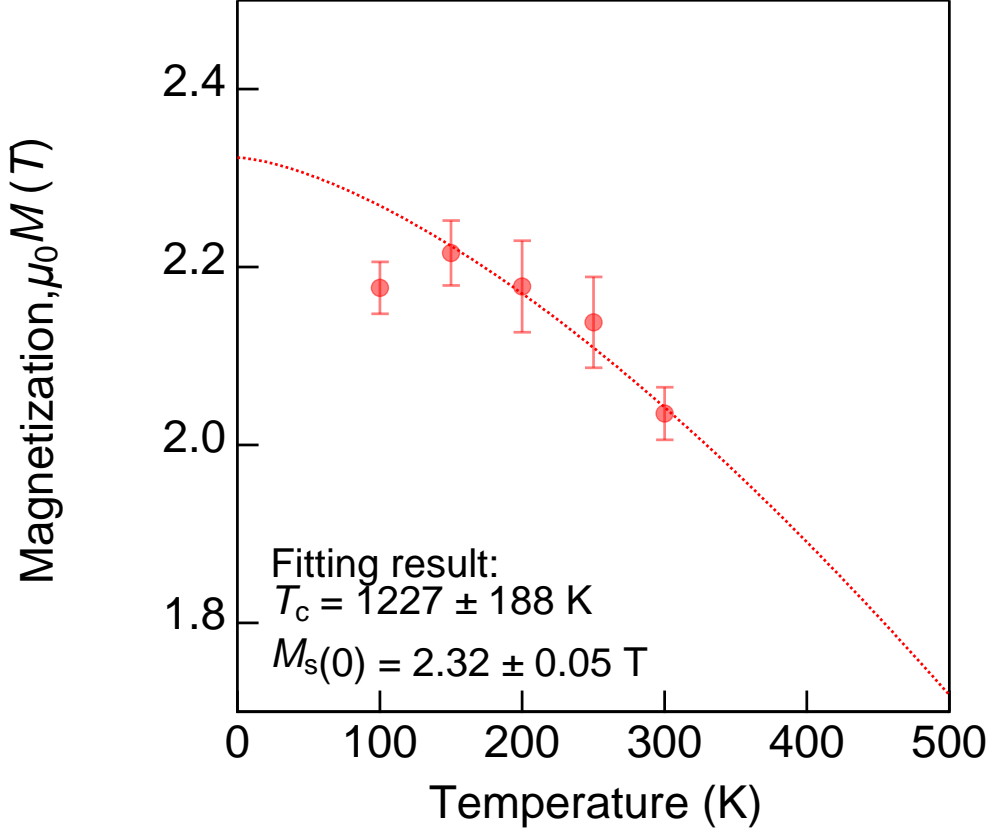
Figure 4.7 Temperature dependence of Magnetization. The dash line indicates the fitting using Equation 4.1.

The temperature dependence of M_s is plotted in Figure 4.7 with the fitting curve using Equation 4.1. The fitting results of T_c and $M_s(0)$ are 1227 ± 188 K and is 2.32 ± 0.05 T, respectively. They are close to the values in bulk Fe, i.e., 1043 K and 2.19 T, respectively. Although Bloch's law is not applicable to the temperature range close to T_c, the result indicates that T_c of Fe in ultrathin-Fe/MgAl$_2$O$_4$ is not significantly reduced. This is in contrast to the previous reports of ultrathin-Fe on Ag[105] or thin Ni and Co on Cu.[106,107] For K_{eff}, we assumed the following simple equation:[47]

$$K_{eff} = \frac{K_i}{t_{Fe}} - 2\pi M_s^2 + K_v$$

4.2

where K_i, $-2\pi M_s^2$, and K_v are the interface, shape, and volume anisotropy energy densities, respectively. Here, we assumed $K_v = 0$ for simplicity, and $K_i = t_{Fe} \cdot (K_{eff} + 2\pi M_s^2)$ was plotted as a function of T in Figure 4.8. The difference in K_i between 100 and 300 K (~2.0 mJ/m^2 at 100 K, ~1.7 mJ/m^2 at 300 K) appears to be small, compared to that of CoFeB/MgO (~1.9 mJ/m^2 at 100 K, ~1.45 mJ/m^2 at 300 K)[79], which may be attributed to the high T_c of the Fe layer. Moreover, we fit the K_i by a power law of $M_s(T)$: [79]

$$K_i(T) = K_i(0) \left(\frac{M_s(T)}{M_s(0)} \right)^{\gamma}$$

4.3

where the $K_i(0)$ is K_i at 0 K. The exponent $\gamma = 1.91 \pm 0.24$ obtained by fitting is close to the values reported in CoFeB/MgO (~2.18 and ~2.16).[79,108] It is worth noting that according to the Callen-Callen law[109] for uniaxial anisotropy, the exponent $\gamma = 3$ is expected; i.e., $K(T)/K(0) = (M_s(T)/M_s(0))^3$, where K is the anisotropy energy.[109] A reduced exponent was theoretically predicted in the presence of large spin-orbit coupling (SOC) materials that contribute to the PMA,[110–113] and consistent with experiment results in FePt[114]. However, further systematic investigation is required by talking into consideration of K_v and higher order anisotropy for better understanding.
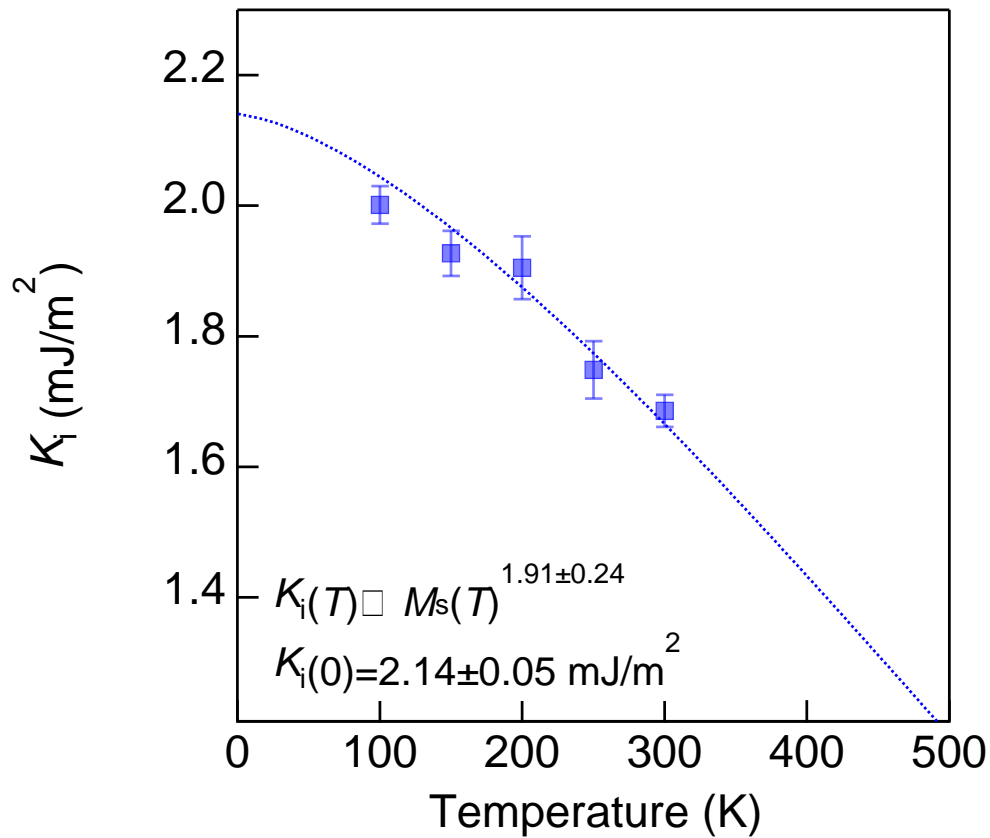
Figure 4.8 Temperature dependence of Magnetization. The dash line indicates the fitting using Equation 4.3.

4.3.3　Magnetic damping constant
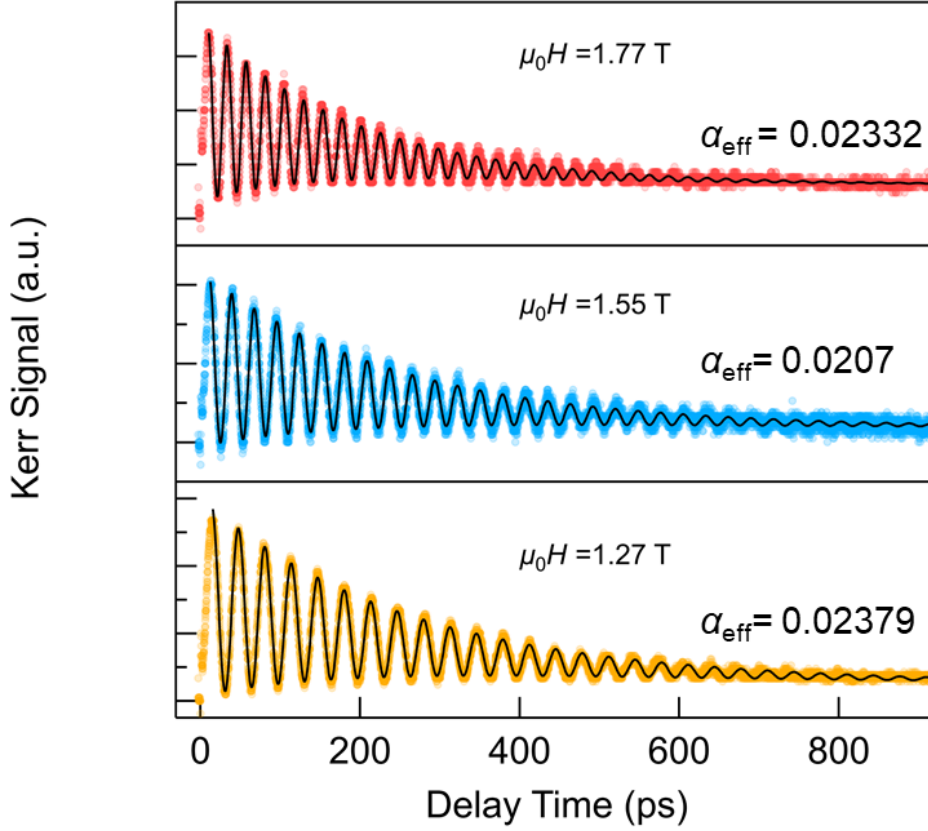
Figure 4.9 Time-dependent signal (scattered data points) of Fe (0.7 nm)/MgAl$_2$O$_4$ (3 nm) under an external bias magnetic field (μ_0H) with different strengths and their best fit using Equation 4.4(solid black lines). The calculated effective damping constant α_{eff} is annotated.

We also evaluated the damping constant (α_{eff}) of the ultrathin Fe layer using TR-MOKE method, since damping constants are likely to have positive correlations with the magnitude of PMA.[115] Such a correlation can be interpreted by the fact that both PMA and magnetic damping originate from spin orbit interaction. Furthermore, PMA and magnetic damping can roughly be discussed based on the density of states; small damping constants are expected to be obtained for the system with a small density of states around the Fermi level,[116] while large PMA due to the so-called Bruno mechanism hardly appears.[117] Figure 4.9 shows the oscillatory magnetization precessional signals of the Fe (0.7 nm)/MgAl$_2$O$_4$ (3 nm) sample with varying μ_0H. α_{eff} is determined by fitting the TR-MOKE signal with a phenomenological fitting function[118]:

$$G(t) = Ae^{-tt_1} + B\sin(2\pi ft - \varphi)e^{-\frac{t}{\tau}} + C, \qquad\qquad 4.4$$

where f corresponds to the precessional resonance frequency, $\tau = \frac{1}{2\pi f\alpha_{eff}}$ is the relaxation time, and φ is the initial phase of oscillation. A and B denote the amplitudes of oscillations. C and t_1 are the offset and the decay rate of demagnetization, respectively. We obtained α_{eff} = 0.0233, 0.0207, and 0.0238 at μ_0H = 1.77 T, 1.55 T, and 1.27 T, respectively, as shown in Figure 4.9, with the lowest α_{eff} obtained ~0.0207. Here, the α_{eff} is not an intrinsic value and only gives the upper limit of true α.[119] It is theoretically predicted that α of very

thin Fe films, to which the interface effect of Fe contributes most, can be much larger than that of the bulk one, although it is unclear at present whether the theoretical prediction is applicable to our experiment.[120] A similar enhancement has also been observed in ultrathin Fe deposited on Ag, where the damping constant for a 0.4 nm Fe film is ~9 times larger than that for thick Fe films.[121]

4.4 Summary

In summary, we prepared epitaxial ultrathin-Fe/MgAl$_2$O$_4$ heterostructures by EB-evaporation. A large PMA energy density up to 1.0 MJ/m^3 was obtained for the 0.7 nm-Fe/3 nm-MgAl$_2$O$_4$ heterostructure annealed at 400°C, which is in good agreement with the theoretical predictions. The PMA sustained even after post-annealing at 500°C, and the changes in the M_s and PMA energy between 100 and 300 K were relatively small. In addition, the areal PMA energy density K_i is found to be proportional to nearly the square of M_s, suggesting that the induced PMA at the Fe/MgAl$_2$O$_4$ interfaces arises from the strong interface SOC. The lowest effective damping constant was estimated to be 0.0207. This study demonstrates robust interface PMA in the ultrathin-Fe/MgAl$_2$O$_4$ useful for p-MTJ applications.

Chapter 5　Spin-dependent resonant tunnel effect in Cr/Fe/MgAl₂O₄ quantum well

5.1　Introduction

Tunnel magnetoresistance (TMR) is the key phenomenon to achieve high-performance spintronic devices[122,123], e.g. magnetic random access memory (MRAM), which is of growing importance for a variety of next generation information processing technologies. Magnetic tunnel junctions (MTJs) consisting of Fe electrodes and an oxide barrier are regarded as an ideal model heterostructure for both fundamental and applied spintronics owing to the simple structure[11,12,24,30,34,35,124]. One of the remarkable transport properties found in the Fe-based MTJs is interplay of TMR effect and resonant tunneling through quantum well (QW) states.[42,125,40,37,126,41,38,39,127,128,43,129,102] Which can be realized by double barrier structure or simply by metallic layer with symmetry dependent band structure. For the ultrathin-Fe/Oxide with (001) crystallographic orientation structure combined with a Cr buffer layer, spin-dependent QW states are formed for the $\Delta_1\uparrow$ symmetry electronic states in Fe, in which the "quasi" QW potential arises from the band mismatch between Cr Δ_1 and Fe $\Delta_1\uparrow$[39,40,43,127,128]. It was theoretically predicted that the introduced QWs can generate resonant states at well-defined energy levels, giving rise to giant modulation of TMR[40]. This is well known as spin dependent resonant tunneling (SDRT) effect that can develop new functionalities. However, the experimental results reported for Cr/Fe/MgO/Fe "quasi" QW-MTJs so far have suggested only a slight sign of the enhanced TMR at resonant bias voltages (V_{bias})[39]. Even for Fe/MgO/Fe/MgO/Au double-barrier MTJs, the enhanced TMR was observed only at very low temperature[38].
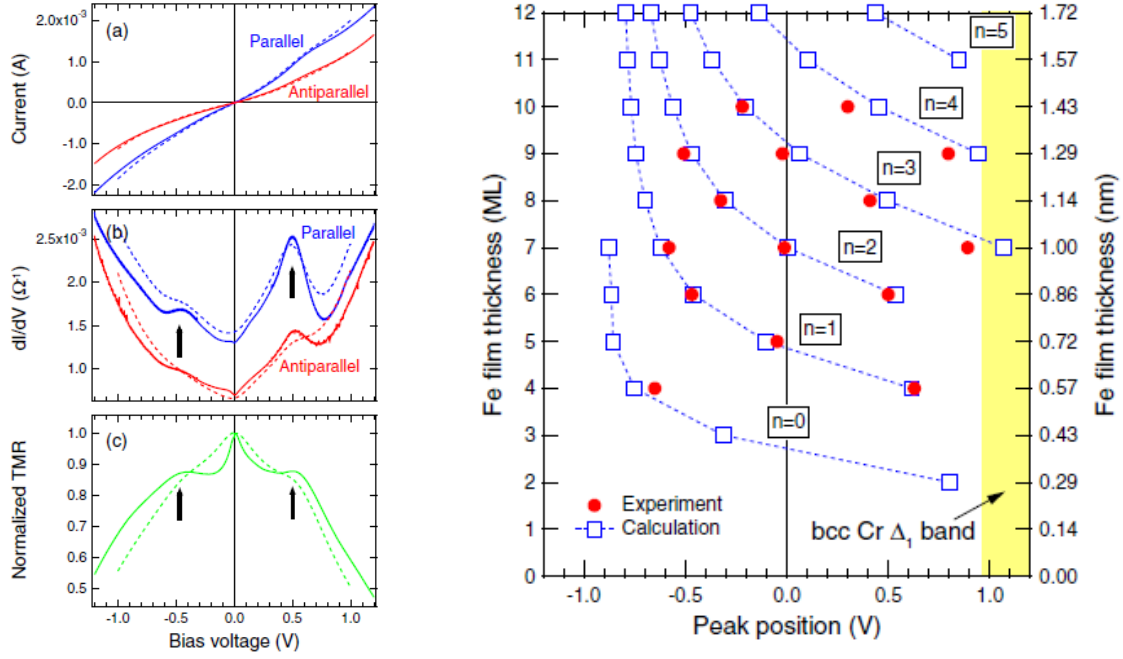
Figure 5.1 SDRT effect in Cr/Fe/MgO. a) current, b) differential conductance and c) normalized TMR with applied bias. d) is the summary of the peak position comparing with theoretical calculation. Reprinted with permission from [39]. ©2008 by the American Physical Society.

In this study, Cr/ultrathin-Fe/MgAl$_2$O$_4$/Fe based MTJs are prepared with precise control of the ultrathin Fe layer thickness t_{Fe}, i.e., the QW width. Owing the exact Fe layer thickness and almost perfect lattice match between Fe and MgAl$_2$O$_4$[supply], the ultrathin-Fe layer exhibit perfect two interfaces to form quantum well. Hence, the SDRT effect dominating the coherent tunneling process of Δ_1-state electrons was clearly observed with a strong modification of TMR at room temperature (RT). The TMR ratio at resonant V_{bias}, at which the $\Delta_{1\uparrow}$ channels are localized, is definitely larger than that at zero bias. In addition, due to the $\Delta_{1\uparrow}$ states localized at specific energy levels, i.e., the formation of well-defined QWs, it was possible to distinguishably observe the T dependence of tunneling conductance through the $\Delta_{1\uparrow}$-QW channels, where the dependences are opposite when located in or out of the resonant bias range.

Besides the fundamental understanding of and the enhanced TMR, it is also important to achieve improved high-bias performance of MTJs, i.e., large voltage output V_{out} (= $V_{bias} \times (R_{AP} - R_P)/R_{AP}$), particularly for magnetic sensing applications. In fact, conventional MTJs are likely to face a serious problem of the TMR degradation at high V_{bias}. For example, while a large RT TMR ratio around 250% near zero bias in CoFeB/MgO based perpendicularly-magnetized MTJs (p-MTJs) was reported, it drastically drops to ~70% at V_{bias} = 0.5 V[130]. The present study offers a possible prescription to this problem.

5.2   Experiment

A fully epitaxial MgO (5 nm)/Cr (30 nm)/Fe-QW (tFe: 0.45−1.25 nm)/MgAl$_2$O$_4$ (2 nm)/Fe (10 nm)/Ru (15 nm) was prepared on a single crystalline MgO (001) substrate. All the layers, except Ru capping layer were deposited by electron beam evaporation under base pressure of less than 1×10−8 Pa. The substrate was first annealed at 800°C for degassing and cleaning surface. Then the 5 nm MgO was deposited on substrate at 450°C as a seeding layer. Then the Cr, QW-Fe, and MgAl$_2$O$_4$ layers were deposited at 150°C wherein the post annealing was performed at 800°C, 250°C, and 400°C respectively. The wedge-shaped Fe layer was deposited with a step of around 0.02 nm using a linear motion shutter equipped between the Fe source and substrate. The top Fe reference layer was deposited at RT without post-annealing to prevent the formation of perpendicular anisotropy at the MgAl$_2$O$_4$/Fe interface. Finally, the stacks were capped with Ru layer via RF magnetron sputtering with the process pressure of 0.4 Pa at RT without post-annealing. The prepared film was patterned into ellipse junctions of 5×10 μm2 in size by conventional micro-fabrication method using Ar ion etching and photolithography as Figure 5.2 shows.
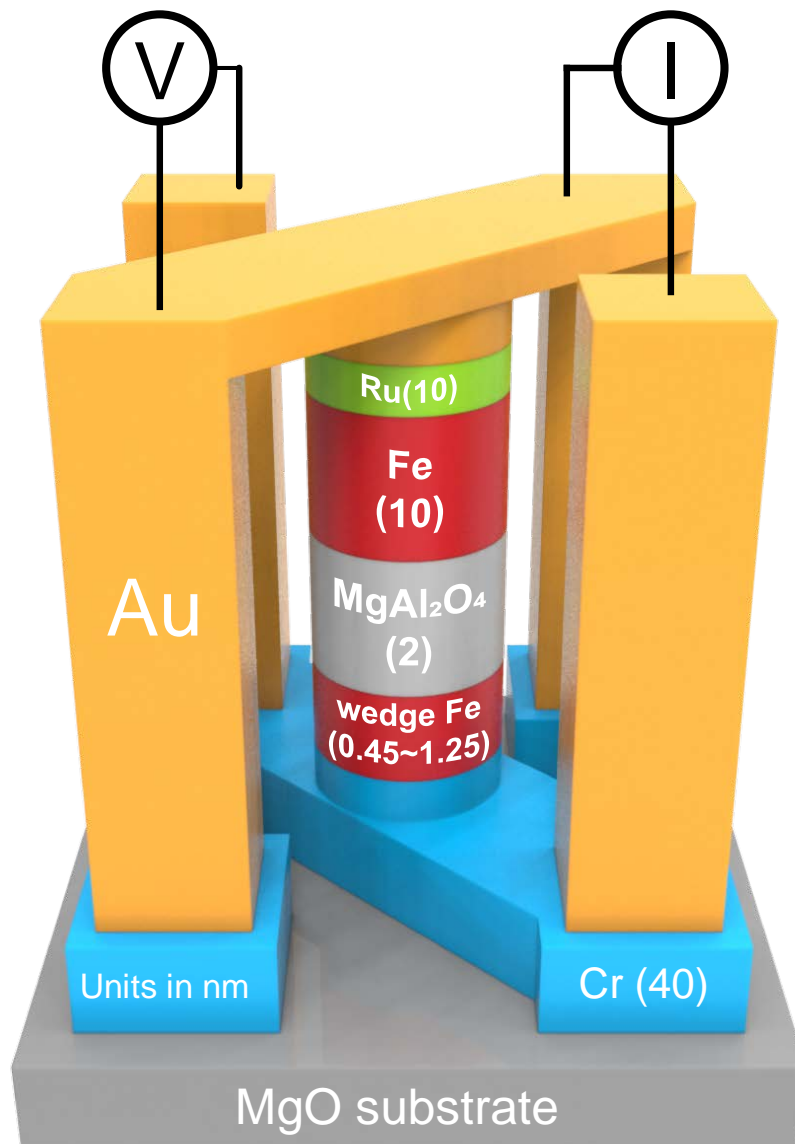
Figure 5.2 Illustration of MTJ used in this experiment.

The junctions then were measured for magnetoresistance (MR) and the current-voltage (I-V) curves using a dc 4-probe method, with bias voltage up to ±1 V. The magnetic field up to 2T is applied perpendicular to the film surface for RT measurement. A low temperature measurement was also performed using physical property measurement system (PPMS). The differential conductance (dI/dV) spectra were mathematic calculated from the I-V curves.
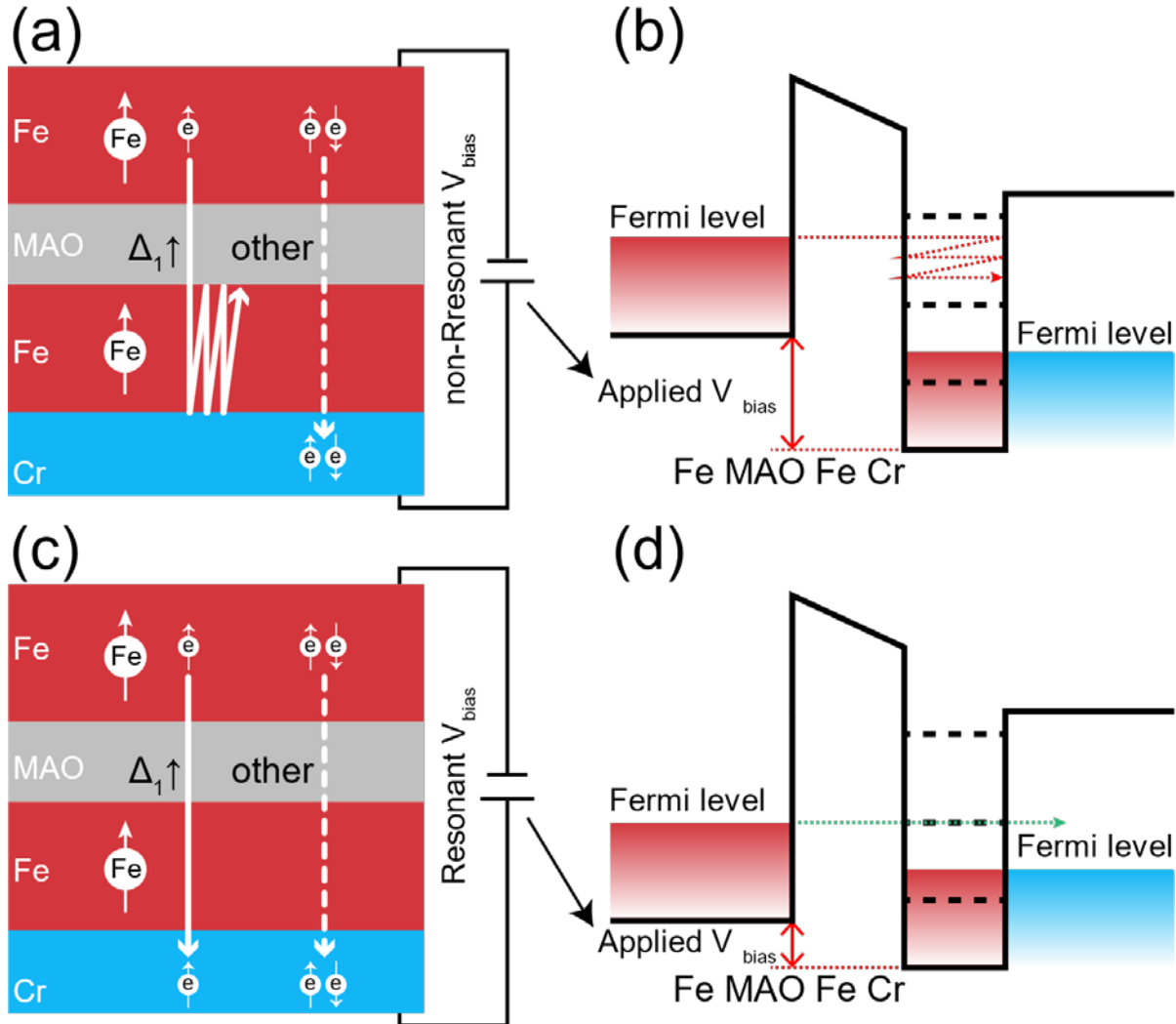
Figure 5.3 (a) (b) Non-resonant and (c) (d) resonant bias voltages, with the potential profile for Δ1↑ electrons.

Figure 5.3 illustrates the concept of SDRT via Fe QWs. To simplify the MTJ structure, MgO (001) single crystalline substrate (sub.)/Cr (40)/Fe (t_{Fe})/MgAl$_2$O$_4$ (2)/Fe (10) stacks (units in nm; t_{Fe} = 0.45 − 1.25) were prepared without pinning and magnetically coupled layers. Further, no post-annealing was performed for the top Fe layer to keep it a general free layer and to limit the QW occurring only in the bottom ultrathin-Fe layer. As well known, the dominant states of the electron transport in epitaxial MTJs with crystalline barrier consisting of MgO or MgAl$_2$O$_4$ possess the Δ_1 (spd-like) symmetry, while tunneling probabilities of other states, i.e., Δ_5 (pd-like), Δ_2 (d-like) and $\Delta_{2'}$ (d-like) states, rapidly decay with increasing the barrier thickness[30,34,35]. This is because electron coherence can be maintained in the tunneling process across the crystalline barrier with the Δ_1 symmetry, resulting in the symmetry filtering. Thus, only Δ_1 symmetry electrons need to be considered for these MTJs. In addition, the TMR effect is a resistance change depending on the relative angle of magnetization of the electrodes, and therefore the TMR ratio is given by the effective spin polarization of Δ_1 electrons in the Fe electrodes. Since there is no Δ_1 states near the Fermi level (E_F) in Cr,

74

even the metallic Cr layer can be regarded as a potential barrier in the present heterostructure of Cr/ultrathin-Fe/MgAl$_2$O$_4$/Fe, leading to a pseudo double-barrier structure for the formation of QW states of Δ_1 symmetry electrons (see Figure 5.4 (b) and (c)). Consequently, the transport properties substantially depend on the applied V_{bias} via the energy levels of QWs. When V_{bias} is far from the resonant position, even the Δ_1 symmetry electrons hardly contribute to the transport, as shown in Figure 5.3 (c) and (d).On the other hand, when V_{bias} coincides with the resonant position, the Δ_1 electrons can pass through the corresponding QW state, as shown in Figure 5.4 (c). In fact, considering that the effective spin polarization of Δ_1 electrons in Fe near its E_{F}, the pseudo double-barrier structure acts like a "spin filter" that efficiently enhances the spin polarization for the Δ_1 symmetry electrons, as theoretically treated in Ref. [40] for Fe/MgO system. While, in this study, QW-SDRT effect in MgAl$_2$O$_4$ is considered similar as in MgO case, since the QW-SDRT originate from imaginary band dispersion within the band gap, where the MgAl$_2$O$_4$ share nearly the same band gap with MgO. More importantly, the disordered spinel structure obtained in this work can be approximate to be the MgO structure as discussed in previous study[93].

5.3 Results and discussion

5.3.1 Layer number dependence of quantum well states
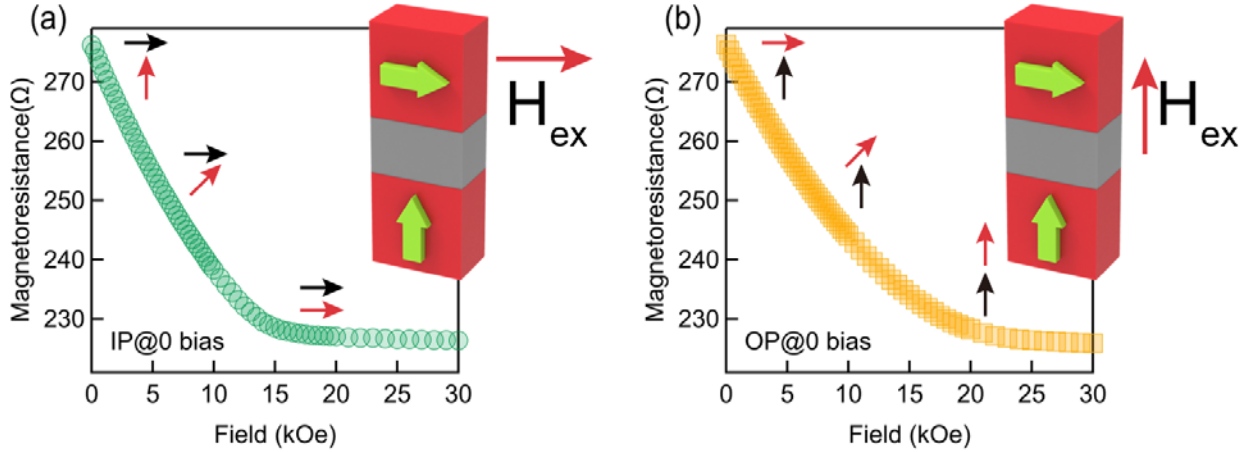
Figure 5.4 (a) schematic illustration of the MTJ and a dc 4-probe measurement setup. Illustration of tunnel behavior at the (b) non-resonant and (c) resonant bias voltages, with the potential profile for $\Delta_1\uparrow$ electrons. (d) Out-of-plane field (H_{ex}) magnetoresistance curve for a MTJ (t_{Fe} = 5 ML) with the orthogonal magnetization configuration. Green arrows in the inset of (d) indicate the magnetization directions.

In this study, due to the interface effect of Fe/MgAl$_2$O$_4$[97,131], the ultrathin Fe layer interface shows large perpendicular magnetic anisotropy (PMA), which leads to an orthogonal configuration of the easy axes of two Fe electrodes as shown in Figure 5.4. The bottom ultrathin-Fe layer possesses an out-of-plane easy axis, while the shape magnetic anisotropy with an in-plane easy axis is dominant in the top Fe electrode. Therefore, TMR was measured with an out-of-plane magnetic field, aligning the magnetization of top free Fe layer to the fixed bottom ultrathin Fe, as shown in Figure 5.4 (d). The TMR ratio of MTJs was defined as $(R_{90} - R_P)/R_P \times$ 100 (%), where R_P and R_{90} are the tunnel resistance at saturation (i.e., parallel (P) magnetization configuration) and zero magnetic fields, respectively. Meanwhile, due to the orthogonal configuration at zero field, the observed TMR is smaller than the conventional TMR that is calculated as $(R_{AP} - R_P)/R_P \times 100$ (%), where R_{AP} is the tunnel resistance of antiparallel (AP) magnetization configurations. Since R_{AP} can be calculated from the relation of $G_{90} = (G_P + G_{AP})/2$[132], where $G_{P(AP)} = 1/R_{P(AP)}$, the Conventional TMR ratios are also calculated for comparison with the related results reported so far. We also investigated the differential conductance (dI/dV) spectra of the MTJs, since the resonant states show up as peak structures in the dI/dV spectra, as discussed in previous reports. [37,39,42,43,127,128]

To prepare the MTJs with an exact integer number of Fe atomic layers, a wedge-shaped Fe layer was deposited with the designed thickness from 0.45 nm to 1.45 nm using a linear motion shutter. This gradually increasing t_{Fe} ensured that MTJs with an integer number of Fe atomic layers existed in a certain part of the sample. Transport properties were measured for all the MTJs with different t_{Fe}, and then the dI/dV spectra were summarized as a conductance map onto V_{bias} and t_{Fe} as Figure 5.5 shows, in which the peak structures clearly represent the formation of QW states oscillational with variation of t_{Fe}. Here, it is considered that t_{Fe} at the peak

positions correspond to integer numbers of Fe atomic layers. Due to shadow effect of linear shutter, possible intermixing at the Cr/Fe interface and/or formation of FeO layer at the Fe/Oxide interface[43], the effective Fe layer thickness, i.e., the QW width, may be smaller than t_{Fe}. Based on theoretical calculations of QWs in Cr/Fe/MgO case[40], the effective Fe layer thickness can be calibrated by the resonant peak positions (black points in Figure 5.5(a)), which is represented by the number of Fe atomic layers n_{Fe}. Note that $t_{Fe} \neq \underline{n}_{Fe}d_{Fe}$ due to discussion above, where $d_{Fe} \sim 0.143$ nm is the thickness of a single Fe atomic layer, i.e., monolayer (ML). We attribute the peaks of $t_{Fe} = 0.81$, 1.02 and 1.22 nm to $n_{Fe} = 5$, 6, and 7 MLs in this study.
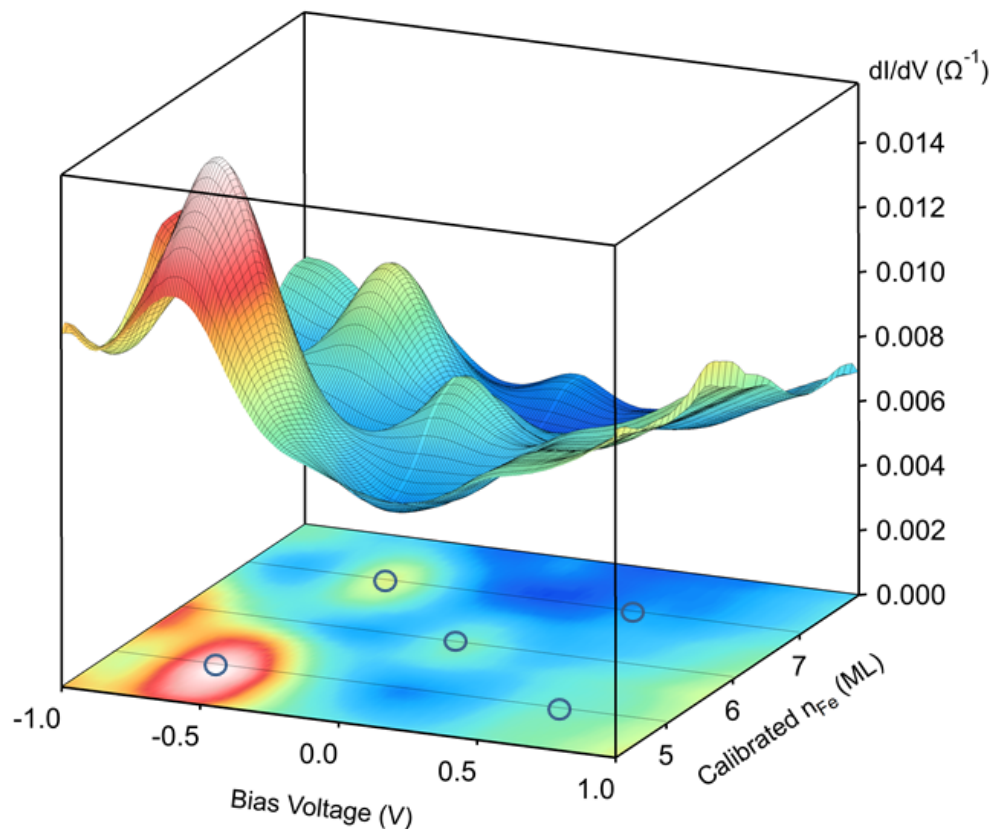
Figure 5.5 Conductance spectrum with Fe thickness and applied bias voltage. The circle indicated the peak positions.

With the thickness of Fe calibrated, a TEM observation is performed to obtain the interlayer structure of the prepared stacks. As the sample is prepared by a wedge Fe, the position where Fe should be 5ML is selected to make the TEM specimen. Figure 5.6 is the obtained TEM image, with the EDS mapping and RHEED pattern. Combining with these techniques, it is confidently to say perfect interfaces are prepared for Cr/Fe, Fe/MgAl$_2$O$_4$. And the EDS mapping also indicating that the position where calibrated as 5-ML is indeed 5-ML of Fe atoms.
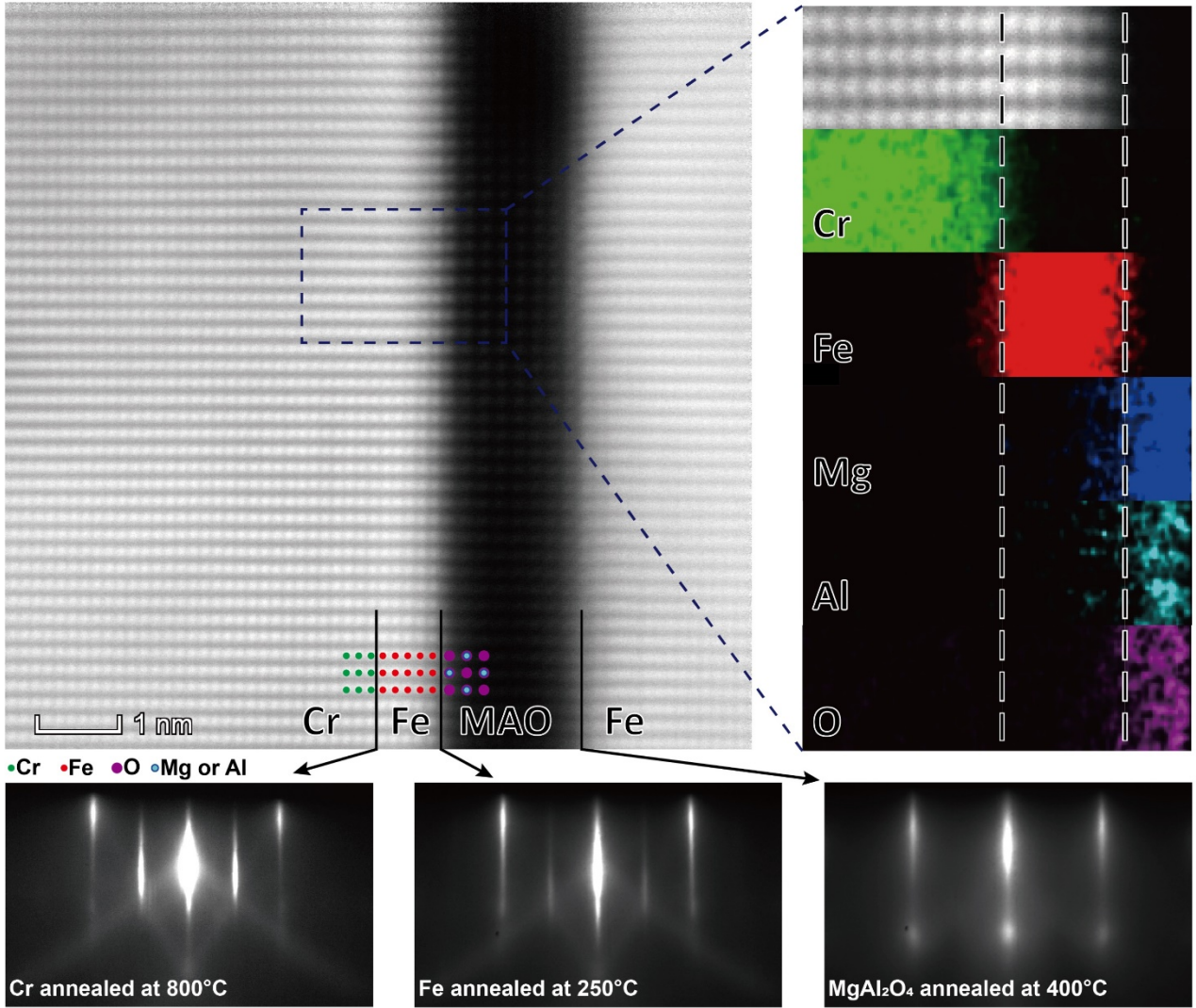
Figure 5.6 TEM image taken for Fe/MgO/Fe multilayer structure where the position correlated to t_{Fe}= 5 ML.

5.3.2 Significant enhancement of TMR through QWs

The TMR ratios are also summarized in same format as shown in Figure 5.7. Comparing with the peak structures in the conductance map, these in TMR ratio map shows the same period, which also indicates clearly that the TMR peaks originate from the SDRT effect. To discuss the SDRT in detail, bias voltage dependences of TMR ratio (observed and conventional), dI/dV, resistance (R), and current for n_{Fe} = 5, 6 and 7 MLs are compared in Figure 5.8. In the dI/dV spectra, the even and odd n_{Fe} samples show clear difference, i.e., two resonant peaks arise away from zero bias for odd n_{Fe}, while a single resonant peak arises at around zero bias for the even n_{Fe}. For n_{Fe} = 5 MLs, the resonant peak positions are around V_{bias} = −0.58 V and +0.55 V, as indicated with the dot lines. The corresponding TMR peaks are observed at V_{bias} a little larger than those for dI/dV. The shift is presumably due to the fact that TMR at a given V_{bias} is calculated from the R values. The most important finding in Figure 5.8 is that the TMR peak of ~24% at the resonant V_{bias} of −0.58 V is even higher than that of ~22% at zero bias. This TMR enhanced behavior is in contrast to MgO-based QW-MTJs: TMR at resonant V_{bias} is 0.8 (~0.6) times as large as that at zero bias at RT in Cr/Fe/MgO/Fe MTJ [39] (Fe/MgO/Fe/MgO/Fe-double-barrier QW-MTJ) at RT[129]. Only at very low temperature, a huge

78

enhancement of TMR was reported so far[38]. Moreover, since the resonant peak is existing at a high V_{bias} for odd n_{Fe}, the TMR becomes less bias sensitive: TMR vary from ~0.9 to ~1.1 of its zero-bias value within [-1 V, 0 V], which hardly found in conventional MTJs.
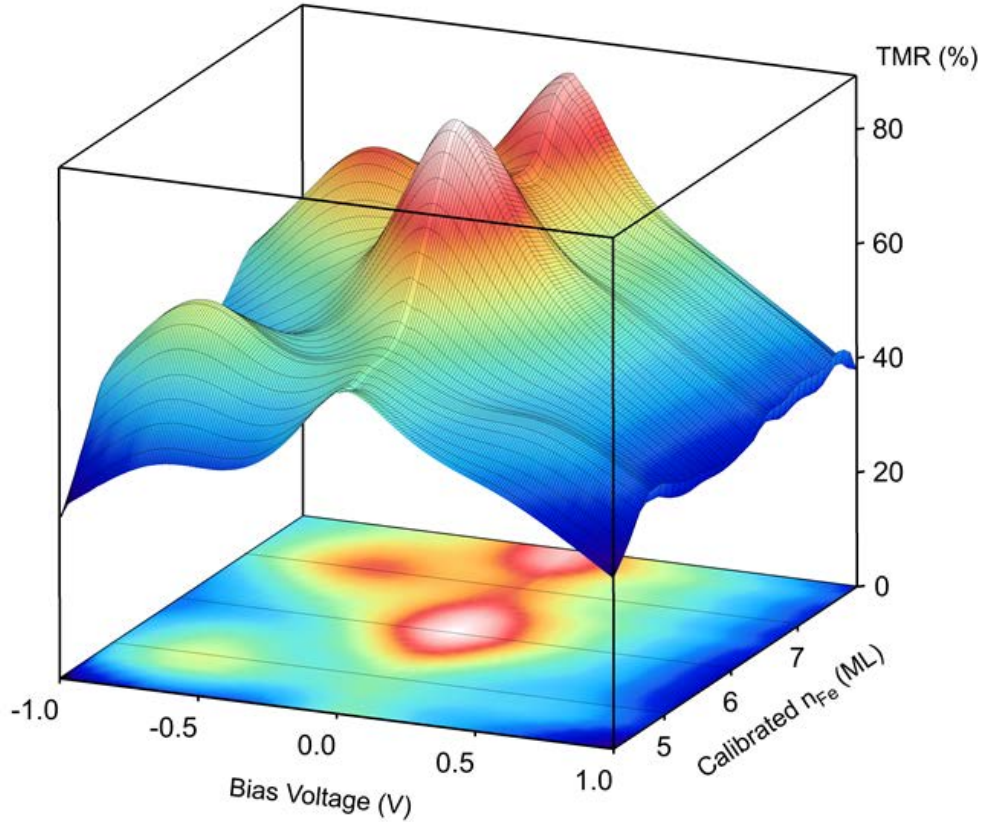
Figure 5.7 TMR map with Fe thickness and applied bias voltage.

As mentioned above, completely different behavior was observed in the MTJs with an even n_{Fe}, showing a single TMR peak as normal MTJs. It is because the resonant bias just located near zero bias, where the intrinsic TMR peak normally located. For $n_{Fe} = 5$ MLs, the TMR at $V_{bias} = 0$ is around 32%.

As mentioned above, the measured TMR ratios are smaller than true value due to the orthogonal configuration. Hence, dI/dV, and R in the AP state are also deduced from those in the parallel (P) and 90° states to investigate the conventional TMR ratio. As shown in Figure 5.8, the SDRT effect on dI/dV in the AP states is much weakened, compared with in P states, which agrees well with the theoretical prediction mentioned above. To explore the possible performance in practical p-MTJs, the conventional TMR calculated from R in the P and AP states is also plotted in Figure 5.8. For $n_{Fe} = 5$ MLs, the TMR ratios at resonant and zero bias are 65% and 55%, respectively. For $n_{Fe} = 6$ MLs, the TMR ratio at zero bias reaches 92%, which is comparable to the highest value in Fe based p-MTJ[97]. Since the top Fe electrode is not optimized at all in the present study, much higher TMR ratios are believed to be obtained for practical p-MTJs made with optimization in the stack structure and preparation processes. In the case of non-integer n_{Fe}, e.g., 5.5 MLs and 6.5 MLs, the peak structures in dI/dV and TMR behave as a simple sum of those with neighboring integer numbers of n_{Fe} as

Figure 5.9 shows. This suggests that it is possible to modulate the TMR behavior between single-peak (for even n_{Fe} cases) type and multi-peaks (odd n_{Fe} cases) type simply by adjusting the Fe coverage.

It is believed the significant enhancement of TMR at resonant bias, compared to previous study, is contributed from two major factors: improved structure coherent owing to $MgAl_2O_4$ and enhanced QW effect owing atomic flat ultrathin Fe. The former one supplies a much-improved high bias performance as previous work suggested[36]. For the later one, both the TEM image[supply] and the giant PMA observed in these films indicate the atomic flat Fe/Oxide interface[51]. Besides, the thinner Fe thickness, e.g. effective QW width, is natural leading the enhancement of QW formation.
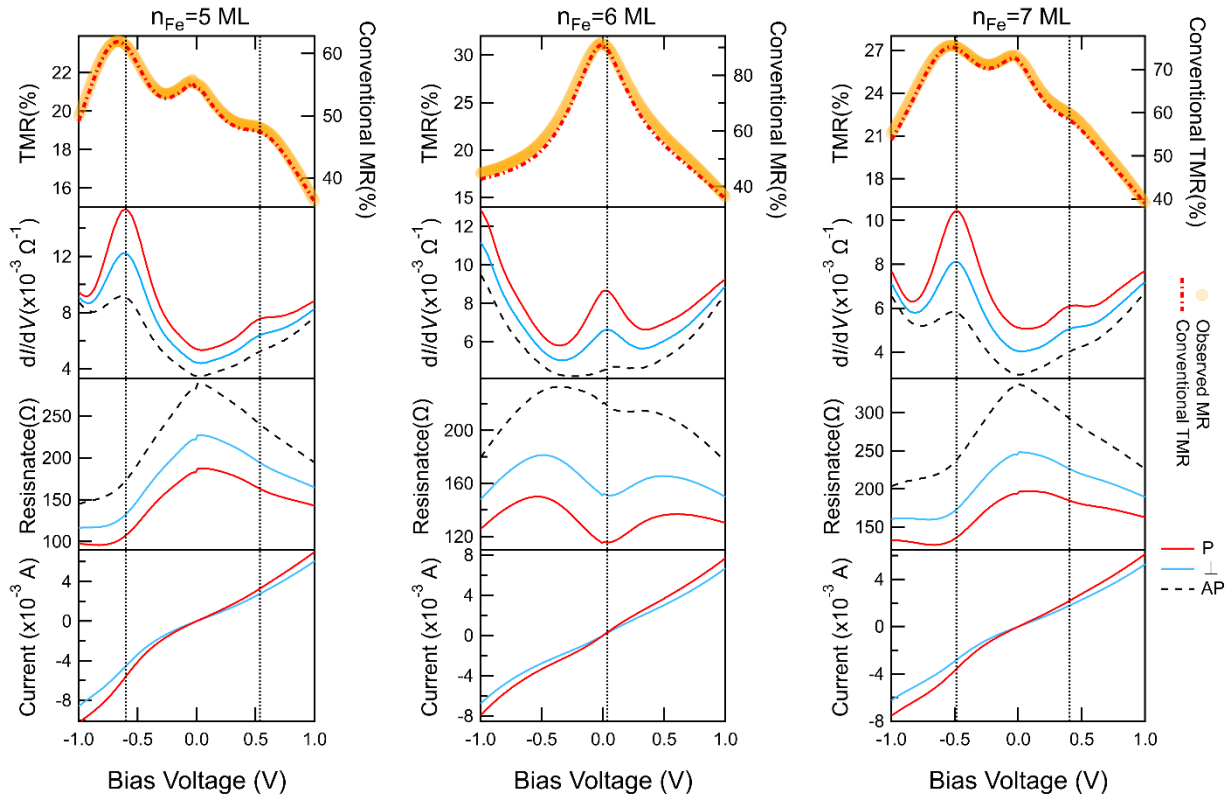
Figure 5.8 TMR, dI/dV and resistance with bias for 5,6 and 7 ML Fe samples. The dash lines indicate calculated conventional related parameters.
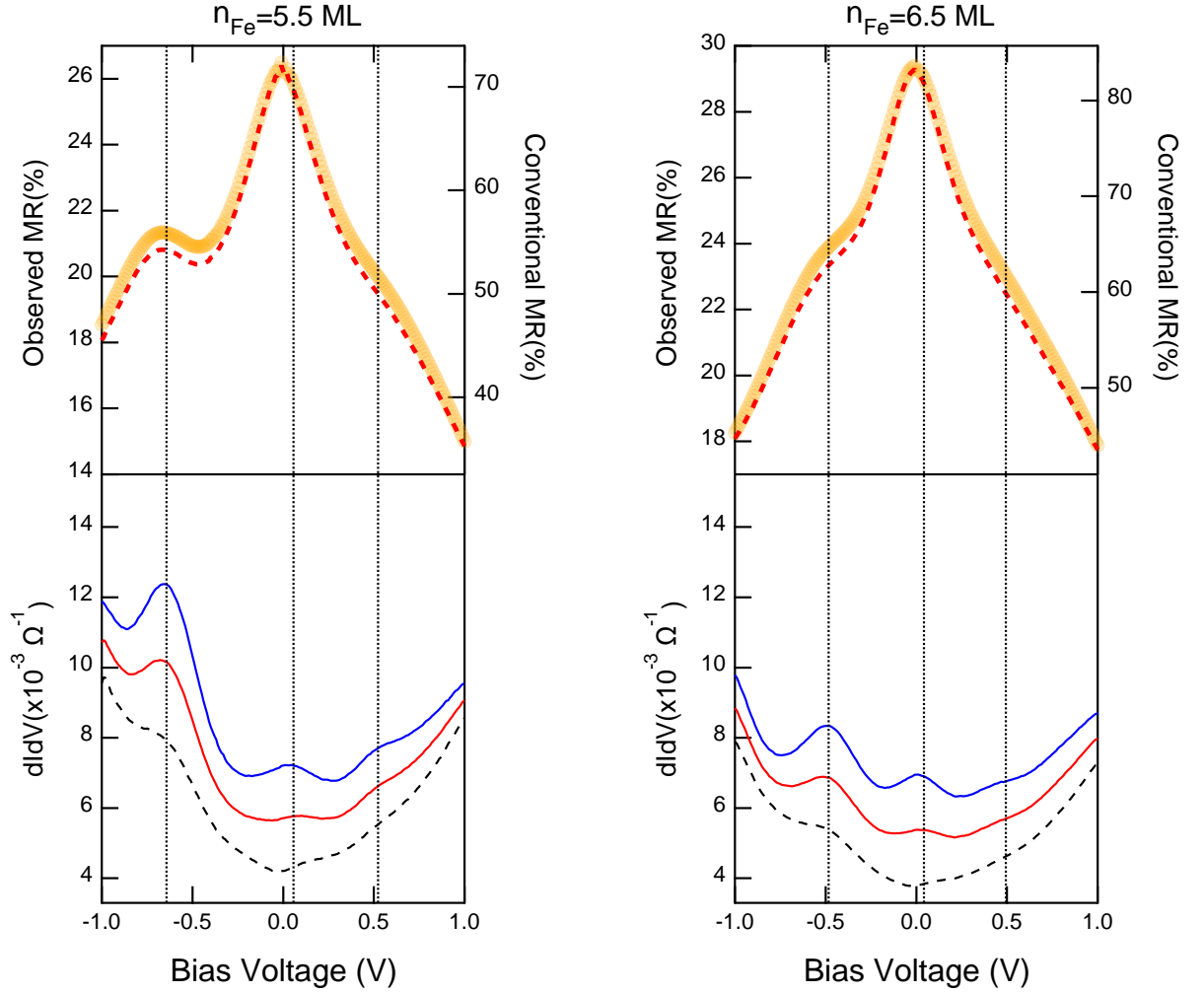
Figure 5.9 TMR and conductance spectrum for.5.5-ML and 6.5-ML samples. The features are consisted from the neighboring integer layer number samples such as 5.5-ML comes from 5- and 6-ML samples.

5.3.3 Temperature dependence of Δ_1 transport

The observed TMR enhancement also suggests the Δ_1 is successfully localized at the specific energy levels, which provides a chance to evaluate the specific T dependence of coherent tunneling effect through the conductance with magnetization parallel aligned, i.e. G_p, where the tunneling effect dominate the transport. The observed T dependence of ΔG_P (= G_P - $G_{P@5K}$) and ΔG_{AP} (= G_{AP} - $G_{AP@5K}$) is plotted in Figure 5.10 for both 5-ML and 6-ML samples. It is clearly observed the G_p has different T dependence regarding to within or without confined states, meanwhile, the difference for AP states is not so significant. Here, I focus on the 5-ML sample where the confined states far from zero bias to avoid the anomaly conductance observed near zero bias.[37] The 5-ML related P states conductance is plotted as Figure 5.11 shows. The dash line indicating the resonant bias, near which the blue region suggests the G_P significant decrease with T increase, while the red or white region suggests the G_P increases or shows relatively small dependence with T increase. To specialize the T dependence, normalized G_P at 3 different bias voltages, i.e. -0.915V, -0.790V and -0.585V, are plotted in (b), where G_P give increase, unchanged and decrease with temperature increasing, respectively.
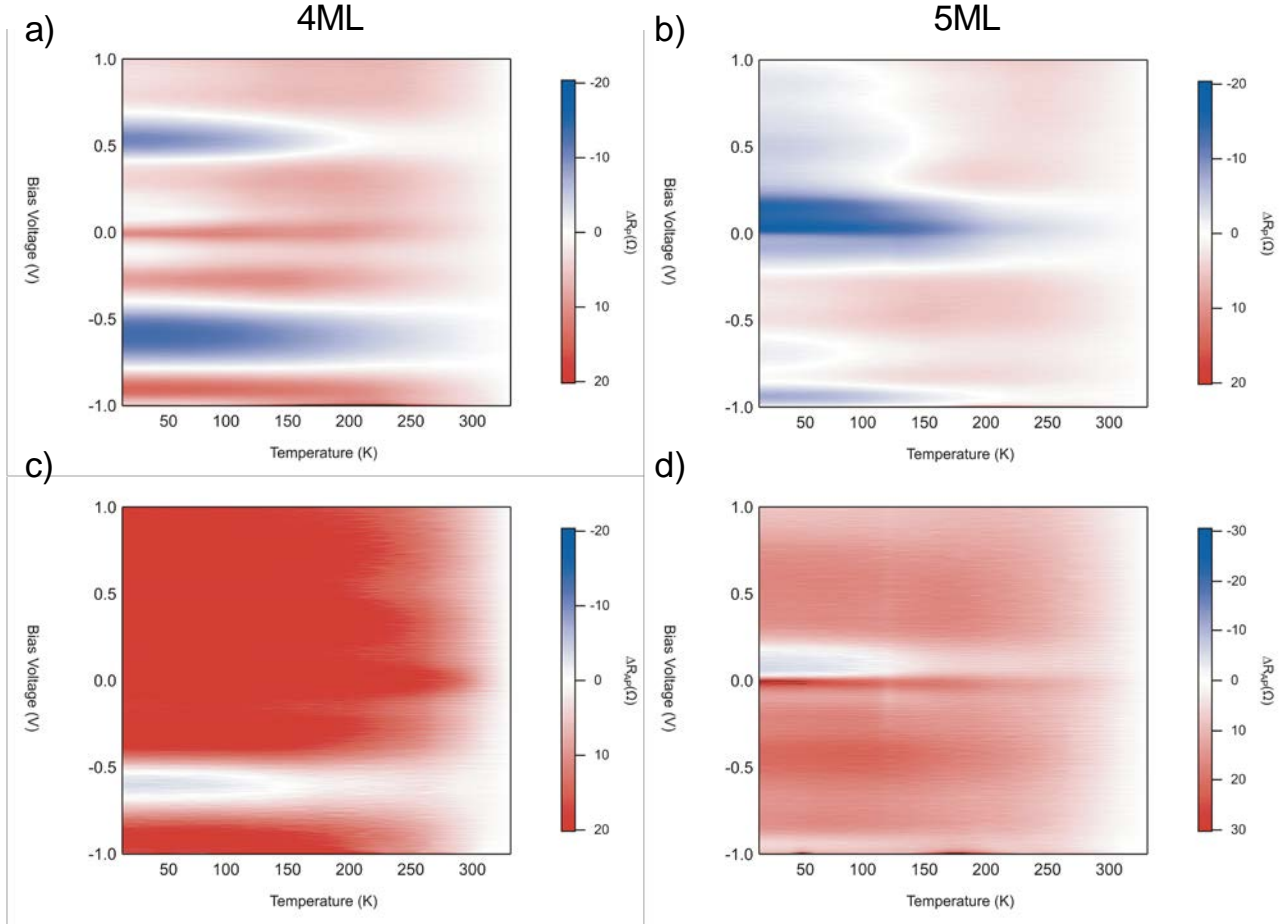
Figure 5.10 Temperature dependence of differential conductance.

To discuss the temperature feature of the tunneling transport, there are two widely discussed major models, i.e. *Zhang* model[133] and *Shang* model[134]. Generally, the *Shang* model only considered spin-conserving elastic tunneling while the *Zhang* model considered the spin-flip inelastic tunneling either. Thus, when discussing increasing temperature, the *Zhang* model predicts an increase G_P, on the contrast the *Shang* model suggests a decrease. The increased G_P has been observed in many epitaxial MTJs and comparable less reports[11,95] of decreased G_P. Some increased G_P is well explained by *Zhang* model while there is no clear understanding for increased G_P. And recently, an extend *Zhang* model[135] successfully explained both increased and decreased G_P, which suggested the inelastic tunneling provide an increase G_P and elastic tunneling provide a decrease G_P with T increase. However, these discussions are based on free electrons, the models are no longer applicable for confined system at finite bias. Here, we only assume the understanding of positive or negative contribution to G_P from inelastic or elastic tunneling applicable for finite bias without numerical meaning. In the extend *Zhang* model, it also suggested that large spin-polarization suggested a large negative contribution from elastic tunneling. In this sense, the observed decrease G_P indicated a well localized Δ_1 through the well-formed QW, showing the elastic tunneling feature. And the increase G_P is just like other normal MTJs, and the unchanged G_P can be regarded as the result of competition between elastic and inelastic features.
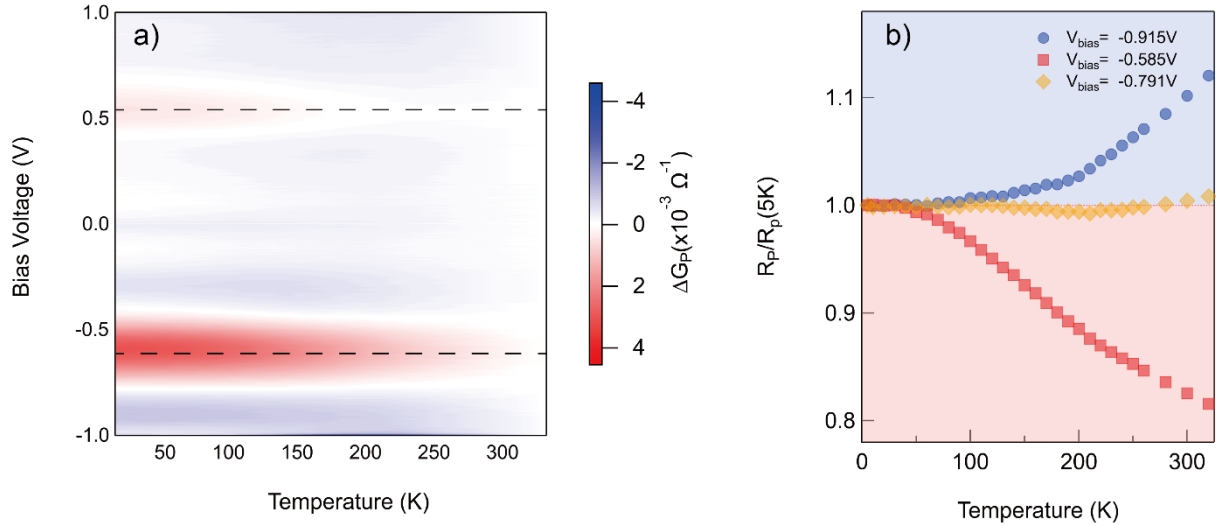
Figure 5.11 Selected dI/dV temperature dependence of 5ML sample and associated TCR.

The tunneling transport of Δ_1 symmetry electrons can be characterized by TCR. In fact, tunneling transport normally shows negative TCR, whereas positive TCR in the P state has been observed for high-quality Fe/MgO (MgAl$_2$O$_4$) based MTJs in which the Δ_1 electron transport should be dominant [Yuasa, Mohamed the positive TCR is likely related to the dominance of the Δ_1 preferential transport through Fe electrodes. Figure 3 shows dI/dV and R as a function of V_{bias} for $n_{Fe} = 5$ and 6 MLs at different temperature. As the color scale from 5 K (blue) to 320 K (red) shows, unconventional positive TCR specific for the Δ_1 electron transport is observed for $n_{Fe} = 6$ MLs in the whole range of V_{bias}. On the other hand, it is found that the sign of TCR changes when $|V_{bias}|$ exceeds the resonant positions shown by red arrows ($V_{bias} < -0.58$ V and $V_{bias} > +0.52$ V, as the blue arrows indicate). This phenomenon of TCR can be interpreted as follows: In the well-defined QW-MTJs, the Δ_1 transport channels are highly localized around the resonant V_{bias}, as suggested by the enhanced TMR appearing at the resonant V_{bias}. As mentioned above, R at a given V_{bias} is given as the integration of the inverse dI/dV from 0 bias to the V_{bias}, so that R at V_{bias} reflects dI/dV ranging from 0 bias to V_{bias}. Therefore, for $n_{Fe} = 5$ ML, R hardly includes the Δ_1 electron character below the resonant V_{bias}, whereas above the resonant V_{bias}, R turns to the resistance dominated by the Δ_1 states, changing the sign of TCR. Positive TCR is always observed for $n_{Fe} = 6$ MLs, since the resonant V_{bias} is around 0 V.
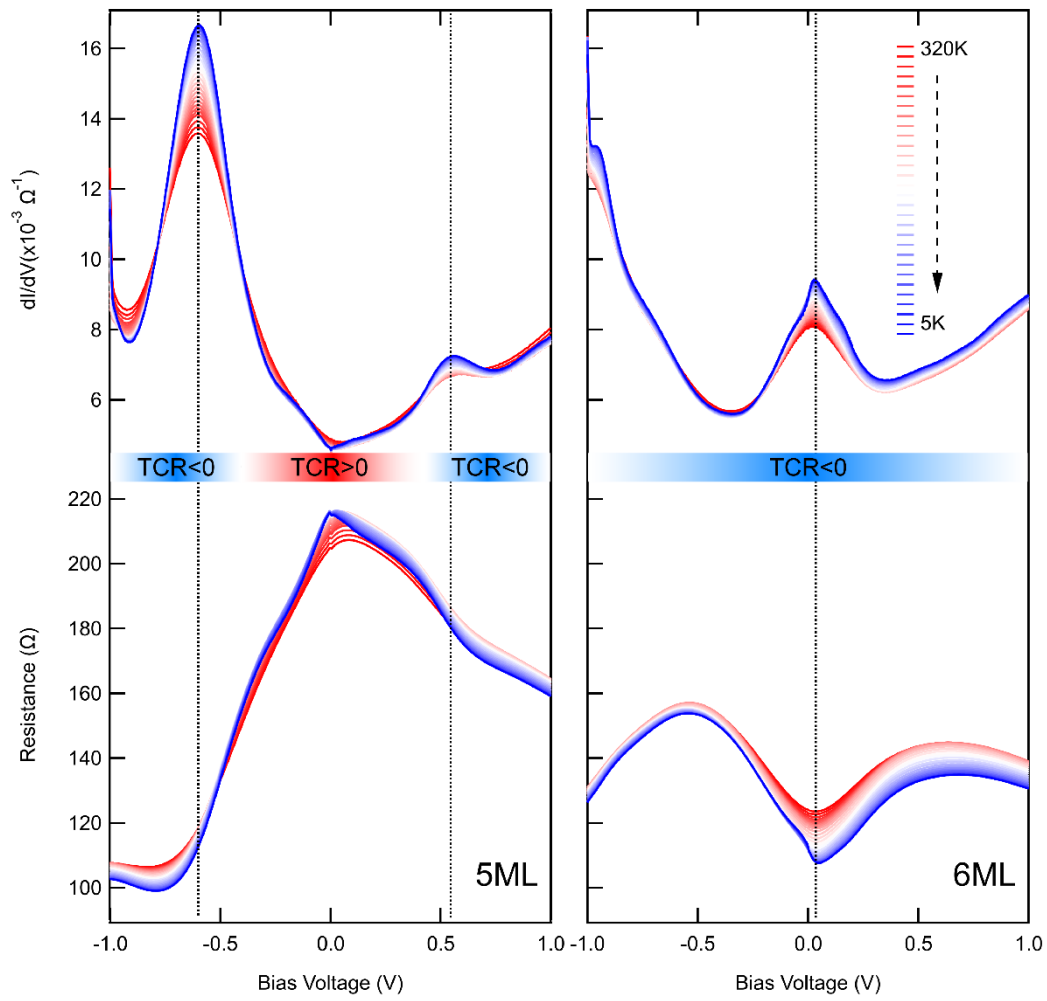
Figure 5.12 TCR for 5 and 6 ML samples.

5.4 Summary

In summary, we demonstrate the enhanced TMR by modifying the Δ_1 electron tunneling transport via QWs that are definitely created in Cr/ultrathin-Fe/MgAl$_2$O$_4$/Fe MTJs. TMR at resonant V_{bias} is even higher than that at 0 bias at RT, while the behavior of dI/dV and TMR strongly depends on whether n_{Fe} is an even or odd number, suggesting that the SDRT through QWs is useful to achieve a large TMR, exclusively at high bias-voltages. In addition, the sign change in TCR was discovered for the present MTJs, as evidence for the formation of well-defined QWs.

Chapter 6 Voltage-controlled magnetic anisotropy in Cr/Fe/MgAl₂O₄ quantum well

6.1   Introduction

The voltage-controlled magnetic anisotropy (VCMA) effect is supposed to be a key factor to realize low-power, high performance and long endurance spintronics devices in the future.[15,56,59,62,66–84] This technology can help to realize low-power magnetization switching in devices, which is a key to next generation magnetic random access memories (MRAMs). These years, remarkable progress has been achieved in this area. Giant anisotropy change in FeX/MgO system[15,77,84], ultrafast pulse-based switch[57,85,86], voltage-assisted Spin-transfer torque(STT) switch[58,60] and non-linear behavior of the VCMA[77,92,84,87].

Cr-buffered Fe/MgO heterostructures are of particular importance in perpendicular magnetic anisotropy (PMA) and relevant studies, and Nozaki *et al*. have recently achieved a remarkable progress in the VCMA study using magnetic tunnel junctions (MTJs) with the Cr/Fe/MgO structure [72]. First, a very large interface PMA was predicted for the Cr/Fe/MgO structure by *ab initio* calculations[136], followed by an experimental demonstration of PMA of ~1.4 MJ/m^3 (~1000 μJ/m^2 for areal energy density) in previous studies[51,89] . Then, The VCMA coefficient obtained in this kind of heterostructures reached 290 fJ/Vm.[84,87] With Cr doped at Fe/MgO interface, the VCMA coefficient and be further enhanced.[137]

Nevertheless, VCMA is not the only factor people should care about. As there are three major switch methods related to VCMA: pulse switch, VCMA+STT and VCMA+SOT, one important issue is the real current required to switch the magnetization has to be reduced. However, current progress of VCMA has some serious problem. For STT and SOT associated switch method, the required current to switch can be only reduced by one direction, and this is the problem caused by the linearity of the VCMA. For the poly-crystal CoFeB/MgO based VCMA research, linear VCMA is most common and with a not so large VCMA coefficient around 100 fJ/Vm.
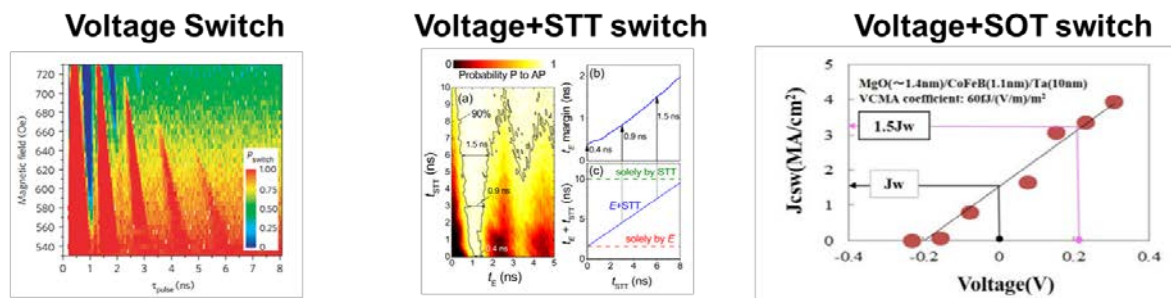
Figure 6.1 Three major methods to switch magnetization trough VCMA effect. a) By voltage puls to switch, reprinted from [57] ©2012 with permission from Springer Nature. b) Combined with voltage and STT switching, reproduced from

[60], with the permission of AIP Publishing. c) Combined with voltage and SOT switching, reproduced with permission from [61] ©2016 IEEE.
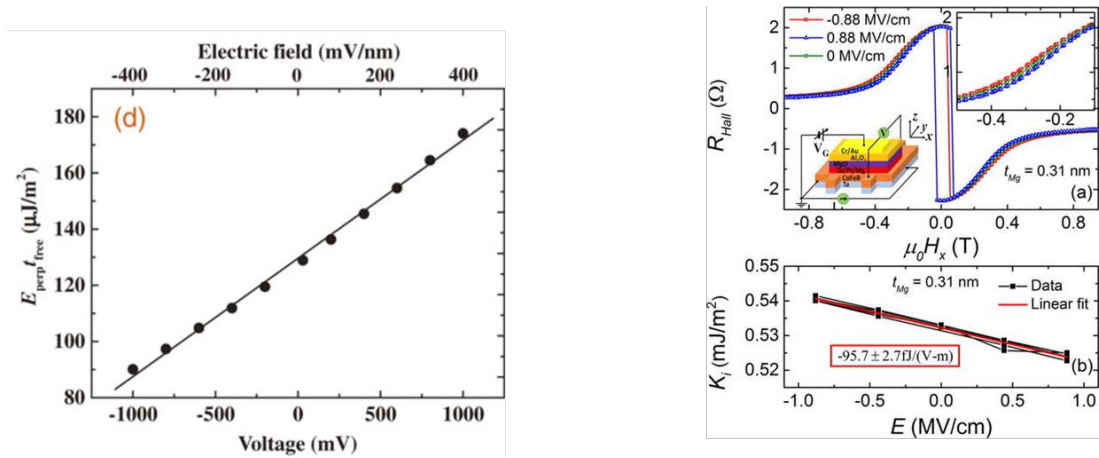
Figure 6.2 VCMA with linear characteristics with VCMA coefficient around 100 fJ/Vm. (a) Reproduced with permission from [78]. ©2014 The Japan Society of Applied Physics. (b) Reproduced from [138], with the permission of AIP Publishing.

However, there is a problem with the obtained large VCMA coefficient: the VCMA exhibits nonlinearity when applied with positive voltage. It causes a problem that the PMA can't be reduced when apply positive voltage while could be enhanced when applying negative voltage. One solution is doping heavy metal to the Fe/MgO interface, successfully obtained reduced PMA at positive voltage, where VCMA shows linearity.[139]
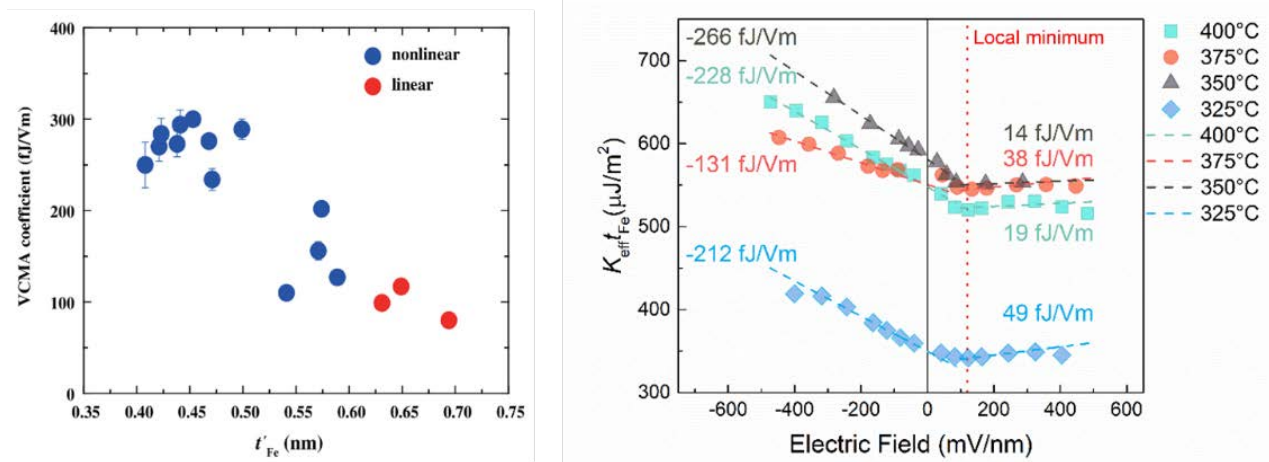
Figure 6.3 Large VCMA with un-favored non-linearity behavior. Reprinted with permission from.[84] ©2016 by the American Physical Society.

Even though, the linear VCMA is still not the final preferred style, which can only realize one-direction switch. An "A" shape VCMA is the most preferred for real switch method or combination with STT switch. With the "A" shape VCMA, one can realize two-direction switch of the magnetization by current only.
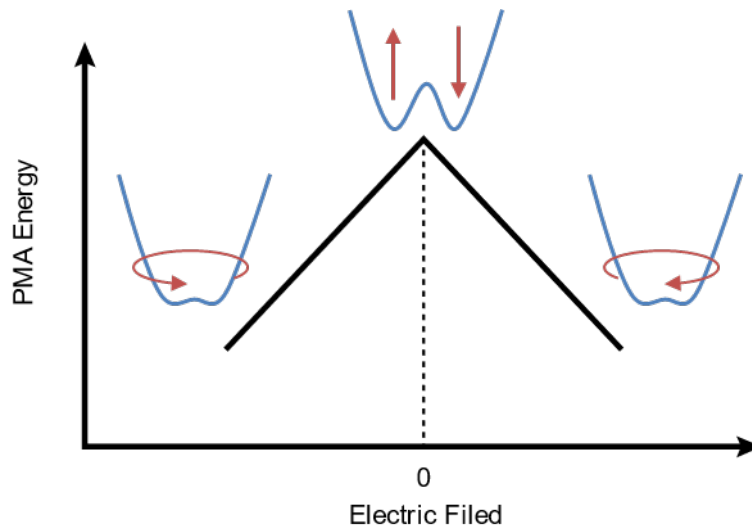
Figure 6.4 favored "A" shape VCMA behavior

In this experiment, a quantum well is introduced inside the ultra-thin Fe electrode to modify the DOS. With the resonant states introduced by the QWs near zero bias, "A" shape VCMA curve is successfully obtained, which means PMA can be reduced at both directions of applied voltages.
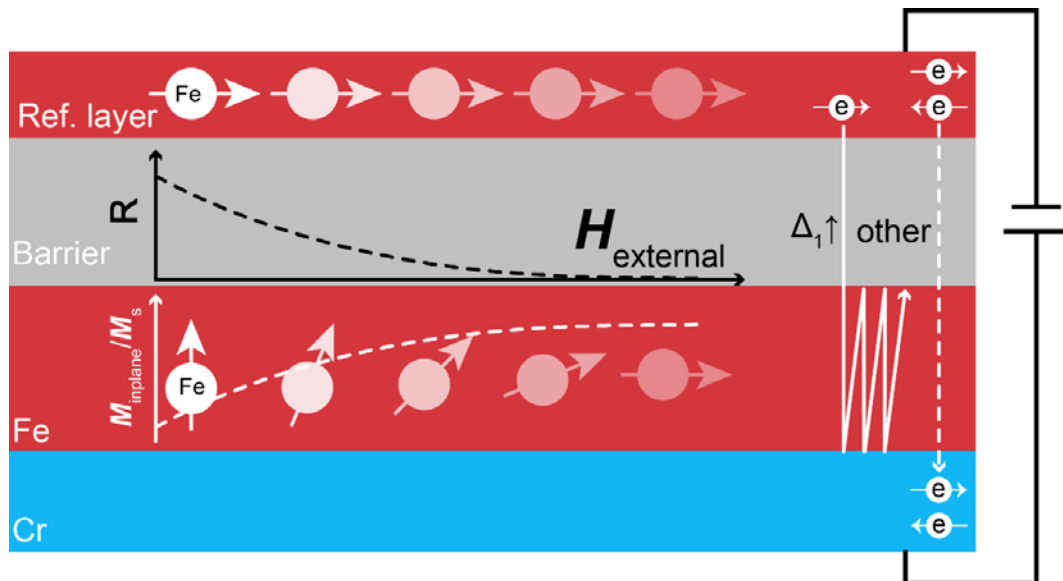
Figure 6.5 Illustration of the magnetization modification in external field.

6.2 Experiment

Two series samples are prepared in this study. Series A samples were designed to examine the Fe thickness dependence and associated SDRT effect. Series B sample were designed to evaluate VCMA effect

Series A is same as the MTJs used in Chapter 5, as Figure 5.2 shows. A fully epitaxial MgO (5 nm)/Cr (30 nm)/Fe-QW (tFe: 3−7 ML)/MgAl$_2$O$_4$ (2 nm)/Fe (10 nm)/Ru (15 nm) prepared on a single crystalline MgO (001) substrate. Series B is a fully epitaxial MgO (5 nm)/Cr (30 nm)/Fe-QW (t_{Fe}=5, 6 and 7 ML)/MgAl$_2$O$_4$ (2 nm)/CoFeB (5 nm)/Ru (15 nm) prepared on a single crystalline MgO (001) substrate. The MgO Cr, QW-Fe and MgAl$_2$O$_4$ layers were deposited by electron beam evaporation under base pressure of less than $1\times10-8$ Pa. The substrate was first annealed at 800°C for degassing and cleaning surface. Then the 5 nm MgO was deposited on substrate at 450°C as a seeding layer. Then the Cr, QW-Fe, and MgAl$_2$O$_4$ layers were deposited at 150°C wherein the post annealing was performed at 800°C, 250°C, and 400°C respectively. The wedge-shaped Fe layer was deposited with a step of around 0.02 nm using a linear motion shutter equipped between the Fe source and substrate. The top Fe reference layer was deposited at RT without post-annealing to prevent the formation of perpendicular anisotropy at the MgAl$_2$O$_4$/Fe interface. Then stacks were capped with Ru layer via RF magnetron sputtering with the process pressure of 0.4 Pa at RT without post-annealing.

Series B is a fully epitaxial MgO (5 nm)/Cr (30 nm)/Fe-QW (t_{Fe}=5, 6 and 7 ML)/MgAl$_2$O$_4$ (2 nm)/CoFeB (5 nm)/Ru (15 nm) prepared on a single crystalline MgO (001) substrate. The major difference is here an integer layer number of Fe layer is designed, thus it can be evaluated by SQUID to detect the accurate magnetic properties. The MgO Cr, QW-Fe and MgAl$_2$O$_4$ layers were deposited by electron beam evaporation under base pressure of less than $1\times10-8$ Pa. The substrate was first annealed at 800°C for degassing and cleaning surface. Then the 5 nm MgO was deposited on substrate at 450°C as a seeding layer. Then the Cr, QW-Fe, and MgAl$_2$O$_4$ layers were deposited at 150°C wherein the post annealing was performed at 800°C, 250°C, and 400°C respectively. The top CoFeB reference layer and capping Ru layer were deposited at RT without post-annealing to prevent the formation of perpendicular anisotropy at the MgAl$_2$O$_4$/Fe interface via RF magnetron sputtering with the process pressure of 0.4 Pa at RT without post-annealing.

The prepared films were patterned into ellipse junctions of 5×10 μm^2 in size by conventional micro-fabrication method using Ar ion etching and photolithography. The junctions then were measured for magnetoresistance (MR) and the current-voltage (I-V) curves using a dc 4-probe method, with bias voltage up to ±1 V. The magnetic field up to 2T is applied in-plane to the film surface for RT measurement. A low temperature measurement was also performed using physical property measurement system (PPMS). The differential conductance (dI/dV) spectra were mathematic calculated from the I-V curves.
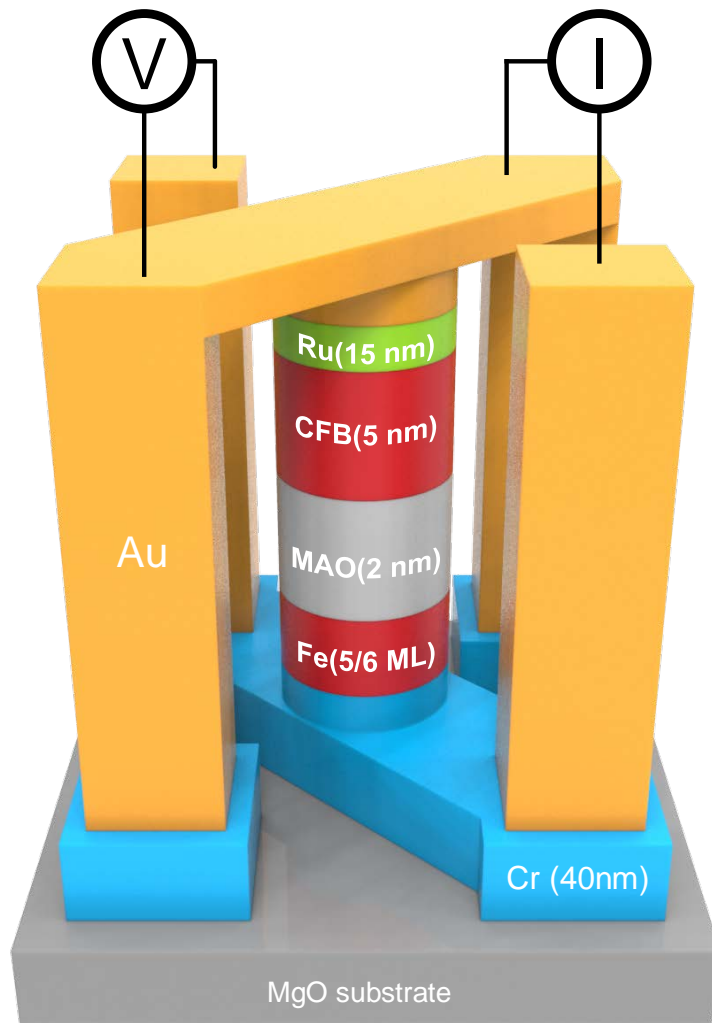
Figure 6.6 MTJ structure in this study.

6.3 Results and discussion

Series A samples were designed to examine the Fe thickness dependence and associated SDRT effect. Series B sample were designed to evaluate VCMA effect

6.3.1 Thickness dependence of PMA

In this study, to examine the accuracy of MR method for PMA evaluation[84], SQUID-VSM method is also used for un-patterned thin films for comparison. Here, series B sample are used due to its fixed Fe thickness.

Figure 6.7 are *M-H* curves for series B samples using SQUID-VSM. The applied magnetic field is in-plane, thus, the easy axis is supplied by CoFeB reference layer, while the thin Fe layers provide perpendicular easy axis. The 5 and 6 ML samples show large PMA, with H_k ~1.7T and 2T respectively.
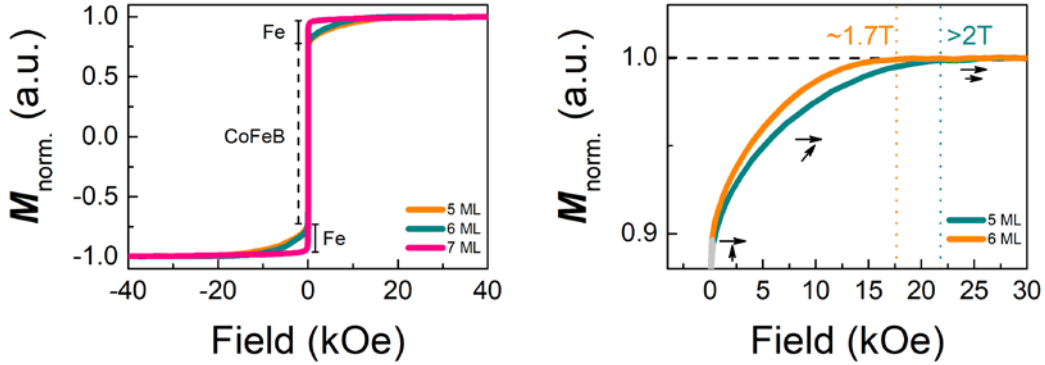
Figure 6.7 a) *M-H* curve for the whole MTJs. The easy axis comes from reference CoFeB, b) subtracted *M-H* from bottom thin Fe layer.

Figure 6.8 shows the result from MR method. Figure 6.8 a) and c) are normalized MR curves measured using 4 prober DC method, with field applied in-plane. The polarity of applied voltage is determined relative to the top reference layer, where, positive and negative application inducing electron accumulation and depletion at ultrathin-Fe/MgAl$_2$O$_4$ interface. Since the tunnel resistance is given by the relative angle between the magnetizations of the free and reference magnetic layers. Thus, the maximum resistance occurs at the 90° configurations (R_{90} at $H_{ex} = 0$), while the minimum resistance does in the parallel configuration (R_p at $H_{ex} = H_k$). The resistance at a given relative angle θ is expressed as:

$$R(\theta) = \frac{R_{90}R_p}{R_p + (R_{90} - R_p) \cdot \cos\theta}$$

6.1

Since the magnetization direction of the top Fe layer is considered to be parallel to H_{ex} (i.e., in-pane direction), the ratio of the in-plane component of the magnetization $M_{in\text{-plane}}$ to its saturation magnetization M_s in the bottom ultrathin Fe layer can be determined as:

$$\frac{M_{in-plane}}{M_s} = \cos\theta = \frac{R_{90} - R(\theta)}{R(\theta)} \frac{R_p}{R_{90} - R_p}$$

6.2

The $M_{in\text{-plane}}/M_s$ calculated are shown as Figure 6.8 b) and d), with the shadow area representing PMA energy density. As comparison, the dash lines are results from the SQUID-VSM method. It is clearly confirmed

that the MR method can measure PMA property correctly as SQUID-VSM.
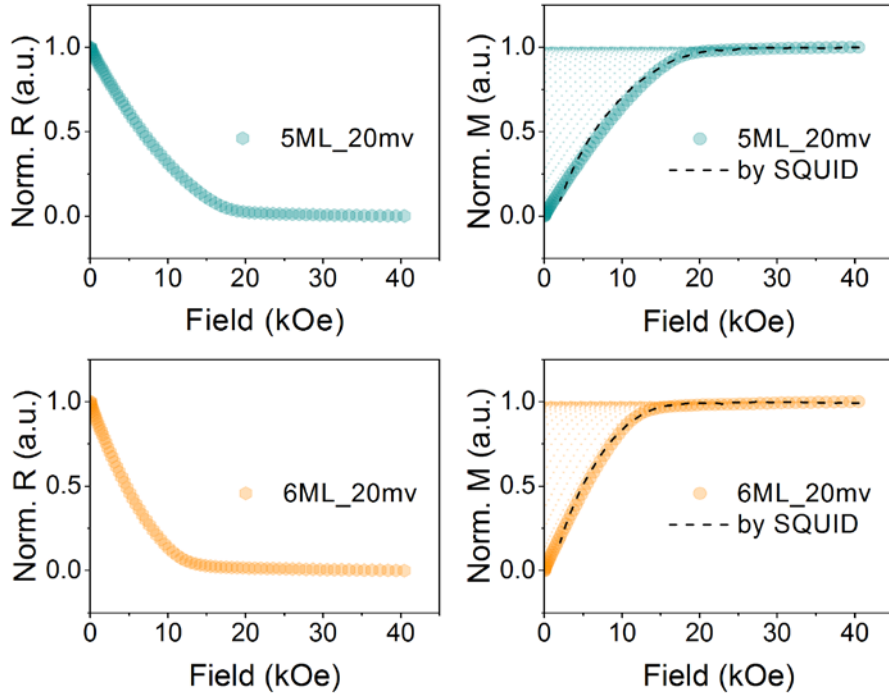
Figure 6.8 MR curves for 5 and 6 ML Fe sample and converted *M-H* curve with comparison with SQUID measurement results.

Using MR method, the PMA properties with different Fe thickness was evaluated. Figure 6.9 shows *M-H* curves with typical Fe thickness, with t_{Fe} increasing, the PMA decreased a lot.
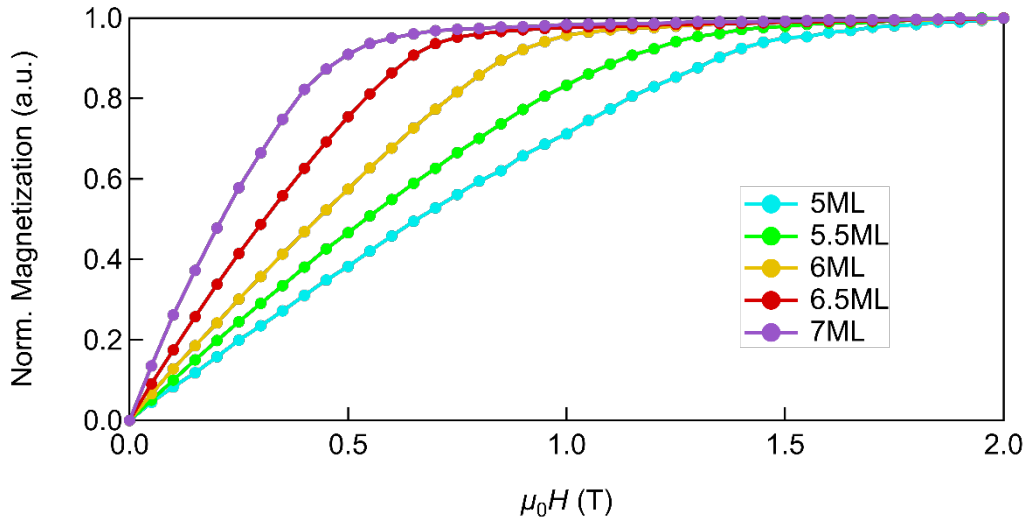
Figure 6.9 *M-H* curves for different Fe thickness

The PMA energies with different t_{Fe} were summarized in Figure 6.10, where we assume the PMA energy following a simple equation as:[47]

$$K_{eff} = \frac{K_i}{t_{Fe}} - 2\pi M_s^2 + K_v$$

6.3

where K_i, $-2\pi M_s^2$, and K_v are the interface, shape, and volume anisotropy energy densities, respectively.

Here, K_i is calculated around 1.86 mJ/m².
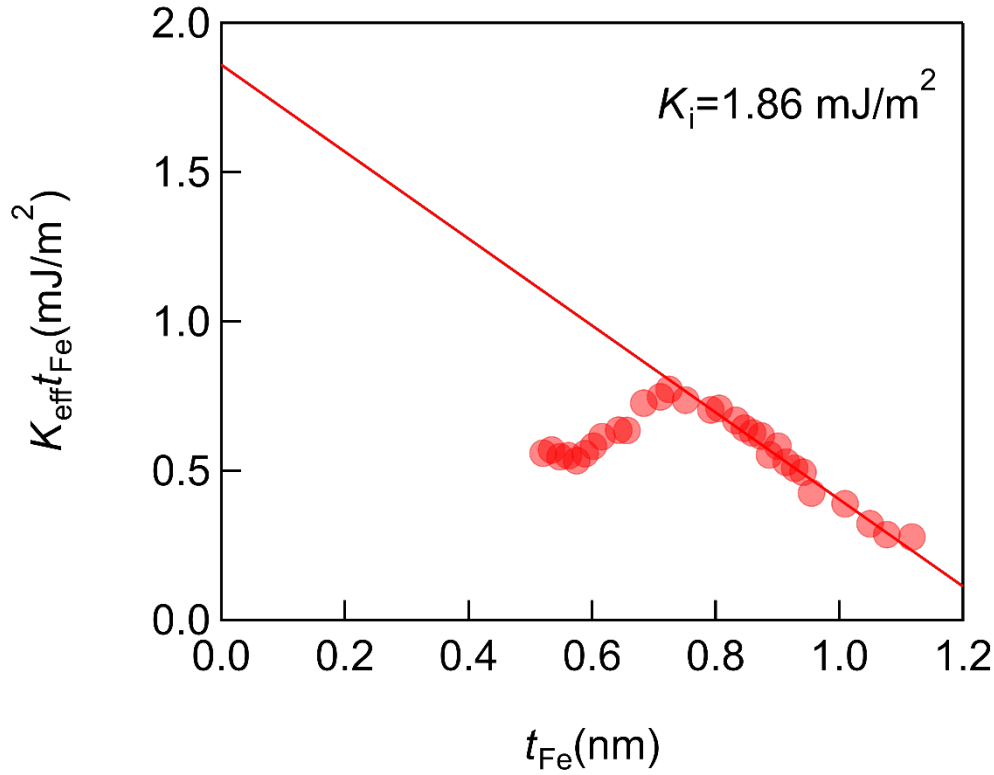
Figure 6.10 $K_{eff}t_{Fe}$ as a function of t_{Fe}

6.3.2 Anomaly modulated VCMA in QW

As discussed in Chapter 5, QWs can be formed in the ultrathin-Fe layer due to the band mismatch of Δ_1 in Fe and Cr. In The conductance spectrum of Series B sample are first examined to confirm the existence of QWs as Figure 6.11 shows. Note that at 0 field, the magnetization in two electrodes are perpendicular to each other while at saturation field, are parallel to each other. Ideally, the SDRT effect is strongest at P states, while for orthogonal and AP states are weakened and totally blocked. For 5 ML sample, there should be no resonant peak near 0 bias, however, a small peak can be observed in Figure 6.11 a), which indicates the thickness shift due to sample preparation.
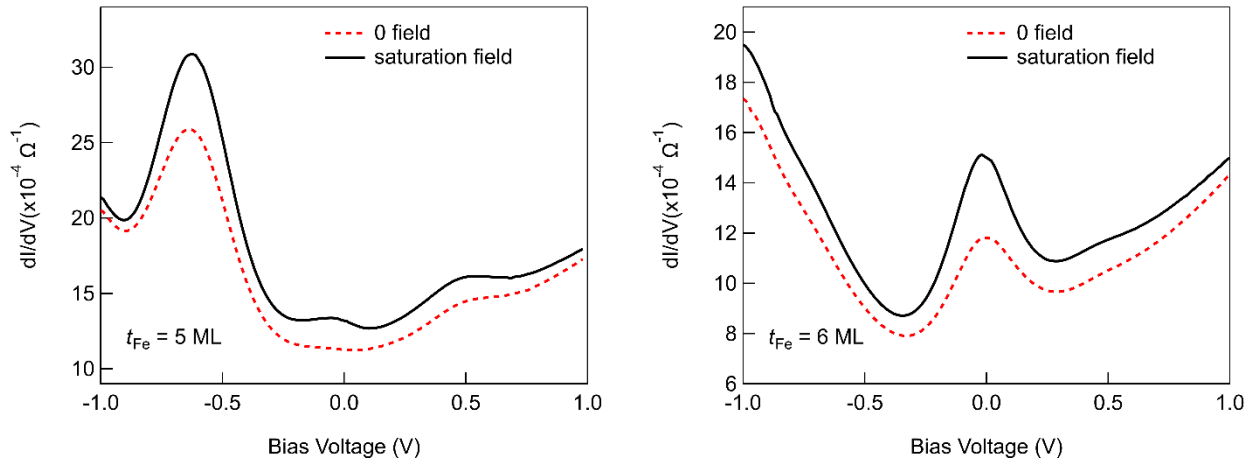
Figure 6.11 Conductance spectrum of sample with t_{Fe} = 5 and 6 ML.

And then the VCMA measurement are carried out using 5- and 6-ML samples. The MR curves are measured under different applied voltage for samples with 5- and 6-ML Fe as Figure 6.12 shows. It is clearly observed that saturation field is modified due to different applied voltage. Generally, negative applications of bias voltage cause increases of PMA while positive application cause decreases.
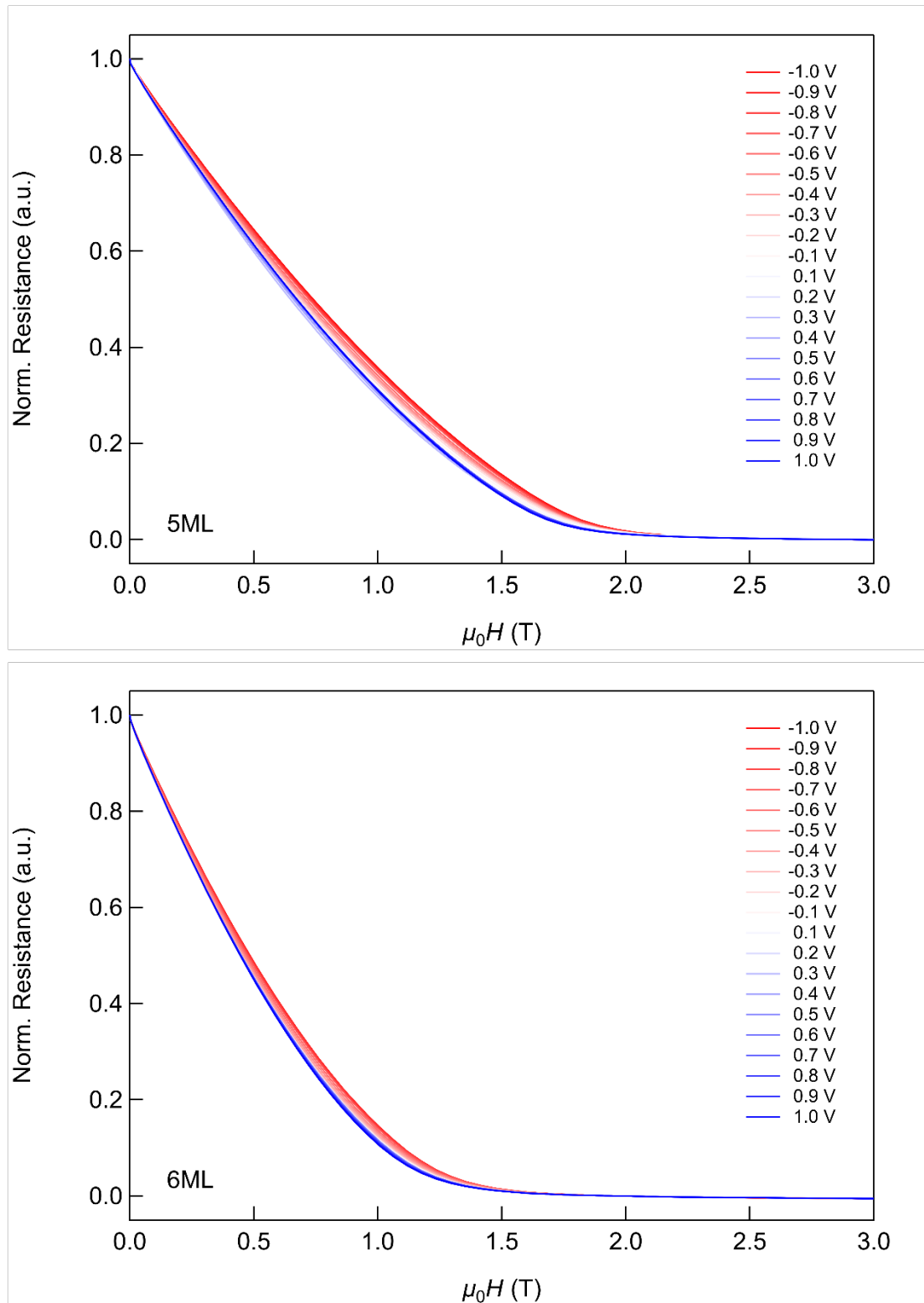
Figure 6.12 typical R-H loops with different applied voltage for samples with 5- and 6-ML Fe

By converting R-H loops into *M-H* loops using equation 6.2, the areal PMA energy density, $K_{eff}t_{Fe}$ is collected with bias dependence. As the applied bias step is set to 10 mV, very high resolution VCMA curves are obtained as Figure 6.13 shows. Owing to this high-resolution measurement, fine structure of VCMA curves are observed, which, show the influence from the DOS modified by QWs inside ultrathin-Fe.
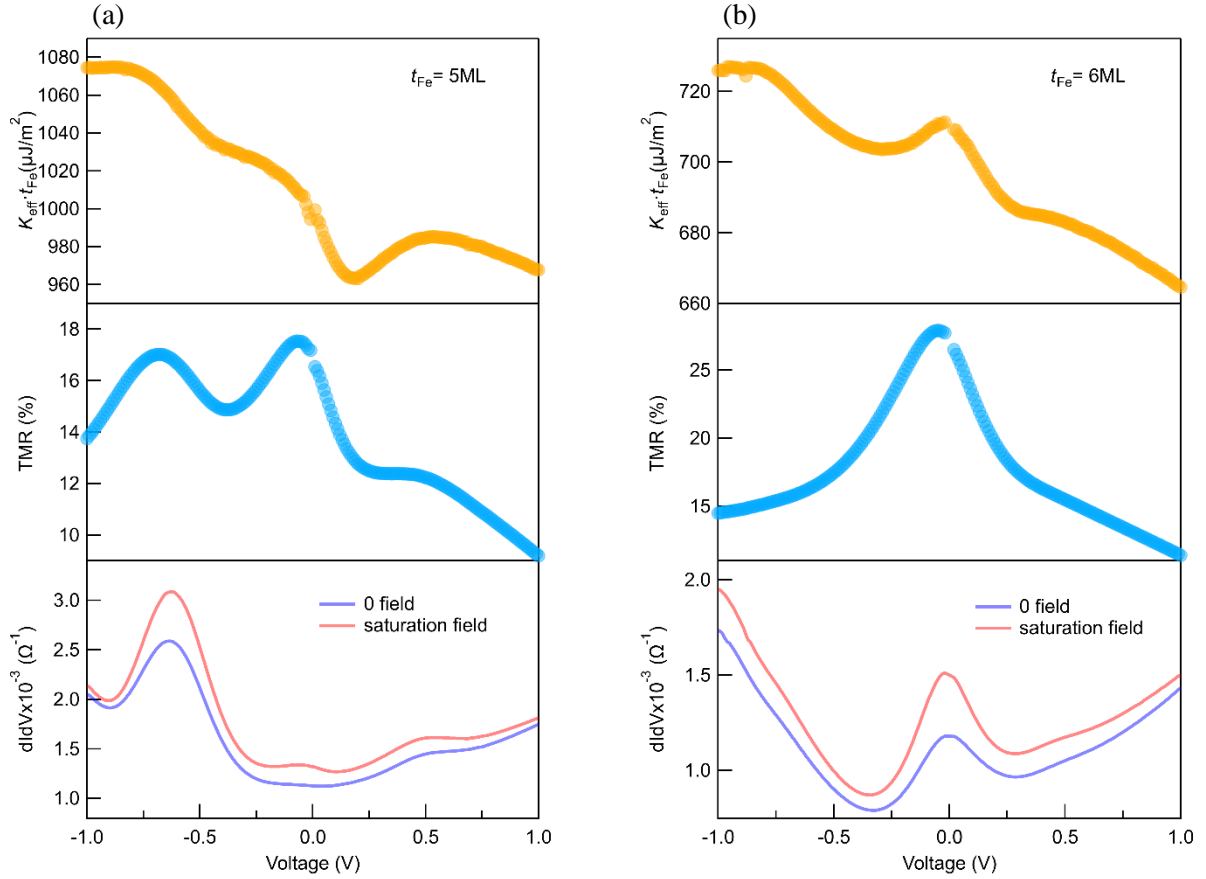
Figure 6.13 VCMA, TMR and dI/dV spectrum for 5- and 6-ML samples

For 5-ML sample, the resonant biases are around ± 0.5V as Figure 6.13 (a) shows. Both TMR and dI/dV spectrum show peak structure near the resonant biases. From the DOS view, the majority will show peak structure near the resonant voltage. When Fermi level is moved to resonant energy level, the SDRT effect occurs showing as enhancement of conductance and TMR ratio. Benefit from the majority enhancement by QWs, the PMA energy can also be enhanced by the spin-flip from majority to minority, which contribute positive to the total MAE of thin Fe film. Owing to the SDRT effect, the PMA energy show consist enhancement as well as TMR and conductance. Note that this kind PMA enhancement will be more obviously for positive bias voltage since the electrons are accumulated at Fe/MgAl$_2$O$_4$ interface when positive bias applied.

Another important character of SDRT effect is that sensitivity to QW width. From calculation, the odd layer QW width will give a high bias resonant position while for even layer QW, the resonant bias located near 0 bias. Considering this, in 6-ML Fe sample, we successfully demonstrate "A" shape VCMA curve near zero bias, where, once bias voltage applied, the PMA energy will drop, as Figure 6.13 (b) shows.

6.3.3   Exclusion the conductance effect

As the VCMA is evaluated by MR method, it is necessary to exclude the influence from the conductance, which also show bias dependence. To clarify the VCMA shape modification came from the bias dependence instead of conductance bias dependence, the sample were measured with magnetic field applied out-plane of the films, which means, the anisotropy energy of the top reference layer was investigated with the same

conductance bias dependence.
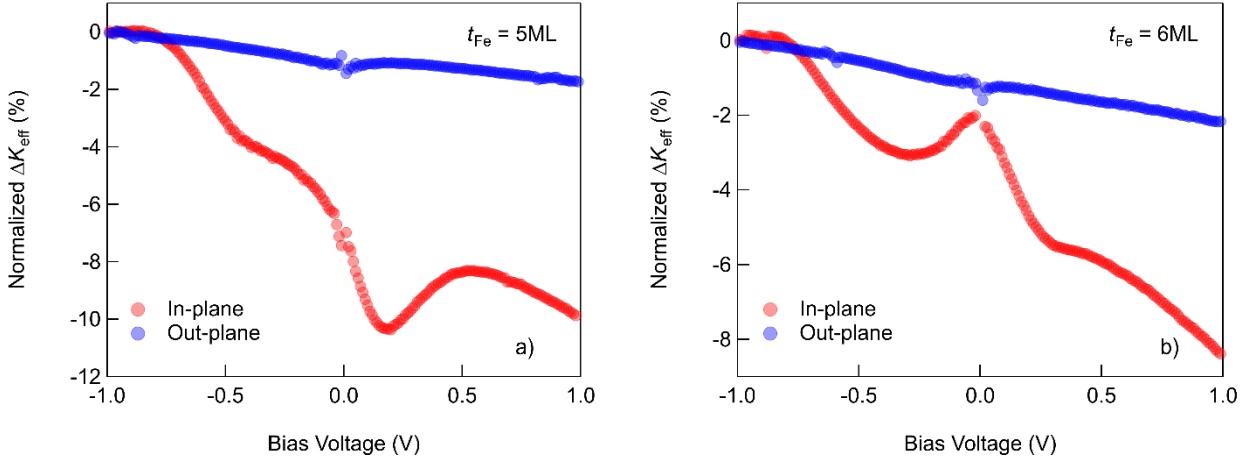
Figure 6.14 Comparison of normalized ΔK_{eff} with magnetic field applied in-plane and out-plane for a) 5- and b) 6-ML samples.

The results are shown in Figure 6.14. The normalized ΔK_{eff} is defined as:

$$\text{Normalized } \Delta K_{eff} = \frac{\left[K_{eff}(V) - K_{eff}(-1V)\right]}{K_{eff}(-1V)} \times 100\% \qquad 6.4$$

Thus, one can compare how much the magnetic anisotropy energy modified by applied bias, with magnetic field applied in-plane direction corresponding to PMA energy density of bottom ultrathin-Fe, and out-plane to top reference Fe layer. Ignoring the amplitudes, the most important difference is that the fine structure only occurs when bottom ultrathin-Fe layer is modified. It suggests that the conductance feature, has no effect on the final output of the VCMA curves. The fine structure comes from the modified DOS of ultrathin-Fe by introduction of QWs.

6.3.4 Anisotropy field fitting trial

Except checking the reference layer from out-plane direction. Another numerical fitting to find the possible anisotropy field from *M-H* curves are executed to verify the observe behavior. If one considering many kinds of effects may modifying the *M-H* curves, most significant effect comes from the relative angel between magnetization and field, which, once the magnetization saturated, will not change anymore. Inspired by this kind of consideration, I try to describe the *M-H* curve using the following equation:

$$\text{M}(H) = \begin{cases} K_0 \times H + k_1 \times sin\left(\frac{\pi H}{2H_k}\right) + k_2 \times sin\left(\frac{2\pi H}{2H_k}\right) + k_3 \times sin\left(\frac{3\pi H}{2H_k}\right) + k_4 \times sin\left(\frac{4\pi H}{2H_k}\right), \ x < H_k \\ K_0 \times H_k + K_1 - K_3 = a, \ x = H_k \\ \frac{1-a}{20-hk} \times x + (1 - \frac{1-a}{20-hk} \times 20), \ x > H_k \end{cases} \qquad 6.5$$

where, H is applied field, a and K_n is numerical parameter, Hk is anisotropy field which equals to saturation field. The basic idea is only when the applied field is smaller than Hk, the M will show angel dependence, and once it is saturated, the M will be a simple constant or linear function to the external field due to other effects.

The fitting is performed to the measured *M-H* curves under various applied field. Figure 6.15 shows an

example from 6-ML sample at bias of 20mV. The fitting **M-H** agrees well with the measured results. And this fitting finally returns to the Hk value, which determined the PMA energy density.
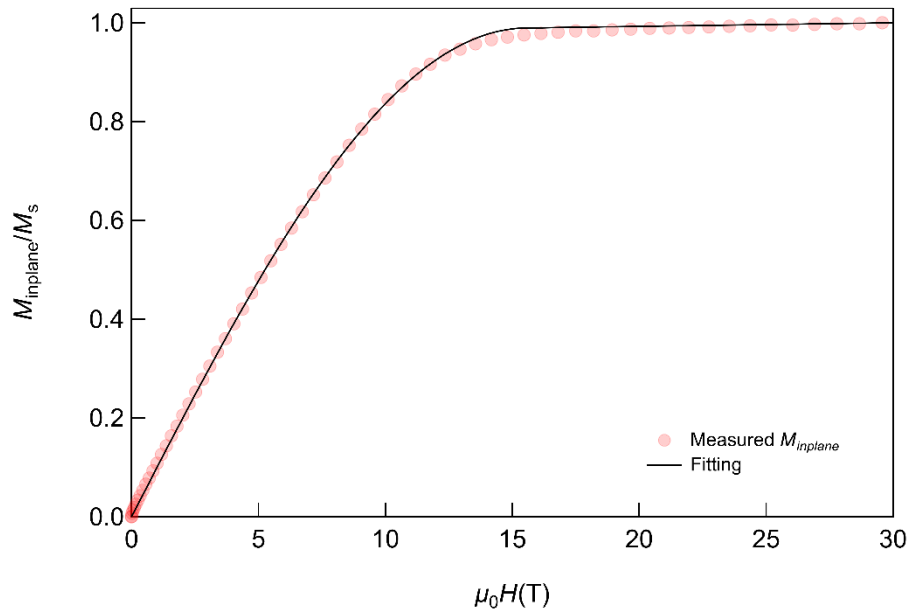
Figure 6.15 Fitting trial using experience equation

With collecting the fitting H_k under various applied voltage, the K_{eff} is also calculated using simple $M_sH_k/2$, where M_s taken as 1500 emu/cc for simplicity. Then comparison from measured K_{eff}, fitting H_k and fitting K_{eff} is made as Figure 6.16 shows.

The fitting result perfectly reproduced the measured results. Here, since the fitting K_{eff} is simply product of fitting H_k and giving M_s, the value is slightly higher than the measured results. However, the importance is that all the features of the captures are well reproduced, which means, the obtained fine structure, is mainly related to the anisotropy field rather than other unexpected factors.
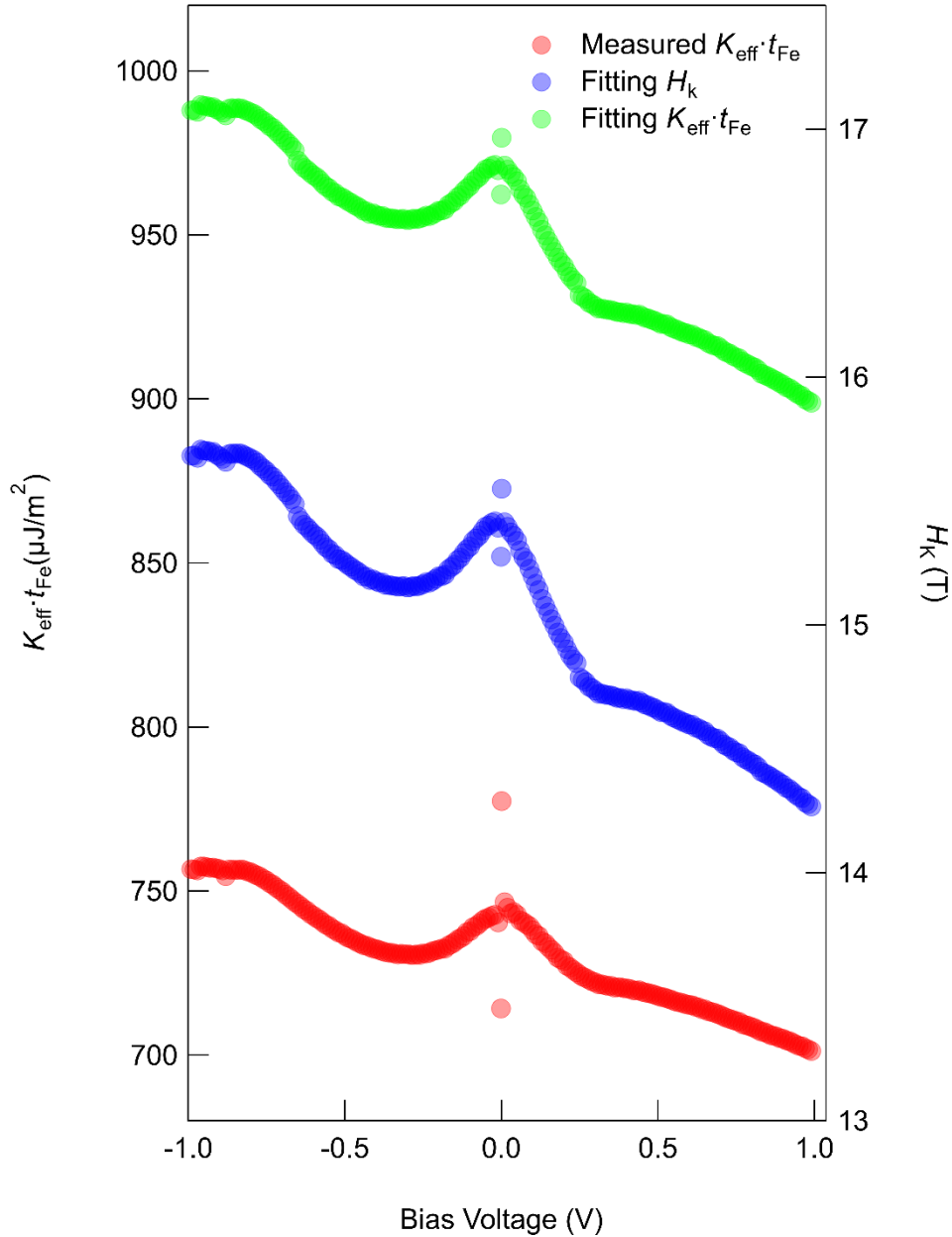
Figure 6.16 The comparison between fitting H_k, measured K_{eff} and fitting K_{eff}.

6.3.5   Barrier thickness dependence

As mentioned at the beginning. The idea to anomaly modulate the VCMA is related to the DOS modification by the SDRT effect. However, a further theoretical calculation is required to convince it. Here, I design a simple experiment to prove the effect is related to potential at the interface rather than to electron accumulation/depletion at the interface, thus, I can somehow attribute the origin to the DOS as the DOS is potential related feature rather than electric field related feature.

In this part, a different sample series is prepared with wedge barrier. As the interface of $Fe/MgAl_2O_4$ is critical for the PMA, the first 1 nm $MgAl_2O_4$ adjacent on Fe is deposited by EB-evaporation, then a wedge $MgAl_2O_4$ is deposited on EB-$MgAl_2O_4$ with sputtering technique.
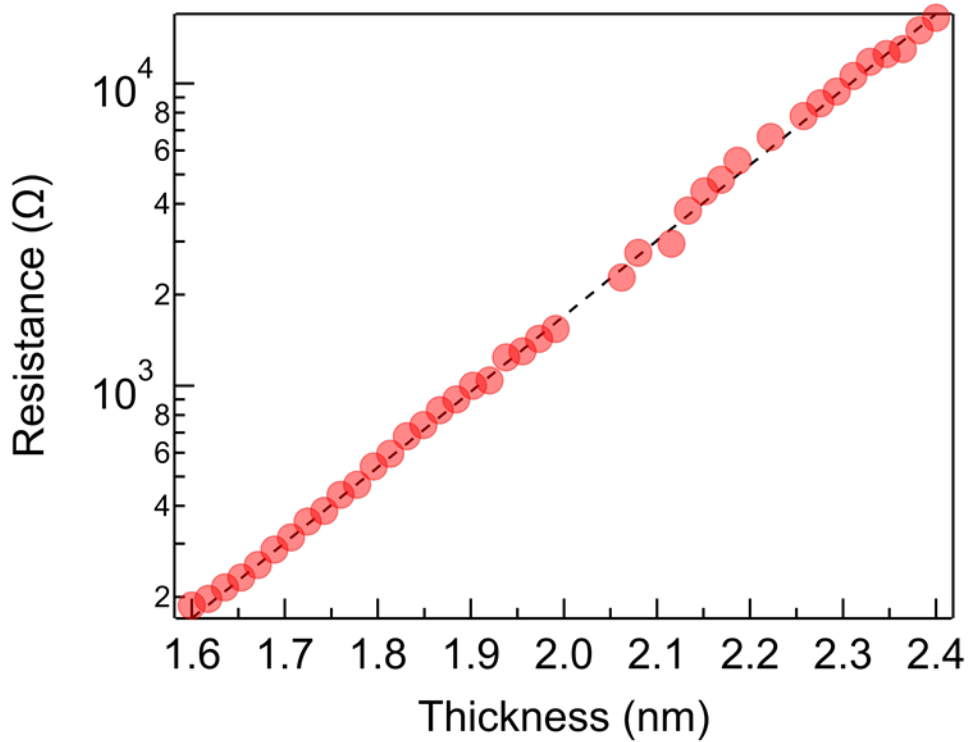
Figure 6.17 MgAl$_2$O$_4$-thickness (t_{MAO})-dependence of resistance in parallel magnetic state (P state) at RT for epitaxial Fe/MgAl$_2$O$_4$/Fe MTJ. Dash lines are least-squares fitting to $c \cdot e^{(\alpha \cdot t_{barrier})}$, where C and α are fitting parameters.

As Figure 6.17 shows, the resistance shows a typical exponential relation with the barrier thickness as:

$$R = c \cdot e^{(\alpha t_{barrier})}$$

6.6

This suggested the two-step barrier deposition technique provide a good layer-adjacent ability as one-step deposition. Then, these junctions are measured for the VCMA as Figure 6.18 shows. The VCMA is separately evaluated regarding to applied voltage or electric field. The former is more related to the energy levels in the DOS, and the latter one is more related to electron accumulation/depletion at the interface.

It is clear observed that, if the VCMA is considering for potential, the features of the capture for various barrier thickness show interesting similarity. It reveals that no matter how thick the barrier, how much the electron passes through this interface, the VCMA gives a same response with same applied voltage. It indicates that the VCMA obtained here, is more related to the potential, i.e. the energy levels at the interface. For more clear comparison, the VCMA coefficient for the range near 0 bias is evaluated also for various barrier thickness.

The VCMA coefficient(ξ_{VCMA}) is plotted as itself or divide by barrier thickness. As the barrier thickness is different, then the electric field applied at the interface is also different with the same applied voltage. Thus, the summarized data shows an interesting conclusion. If we evaluated the VCMA coefficient by voltage, then the different barrier thickness sample provide a same VCMA coefficient. However, if the VCMA coefficient is evaluated by electric field, then it increases with increasing barrier thickness. From this point of view, it looks like the hypothesis that the VCMA obtained in this study only has potential sensitivity rather than electric field sensitivity.
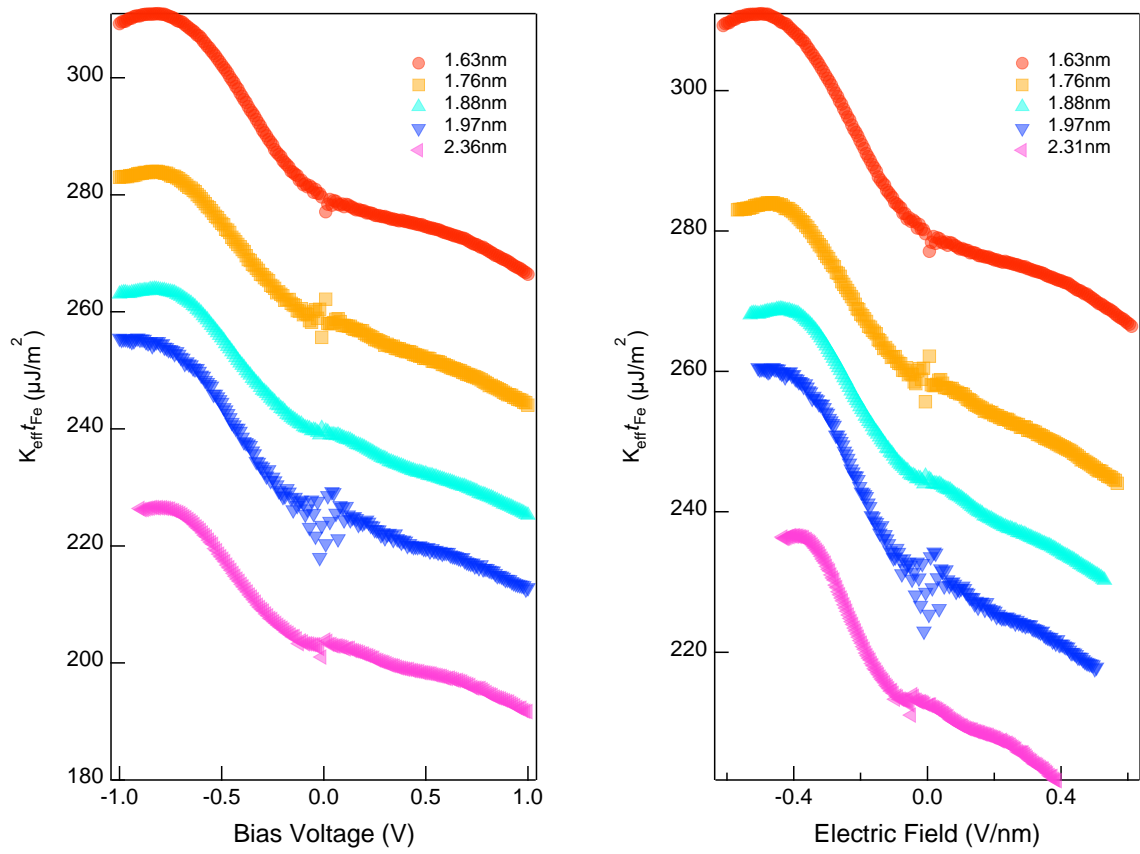
Figure 6.18 The $K_{eff}t_{Fe}$ as a function of applied bias voltage and electric field.
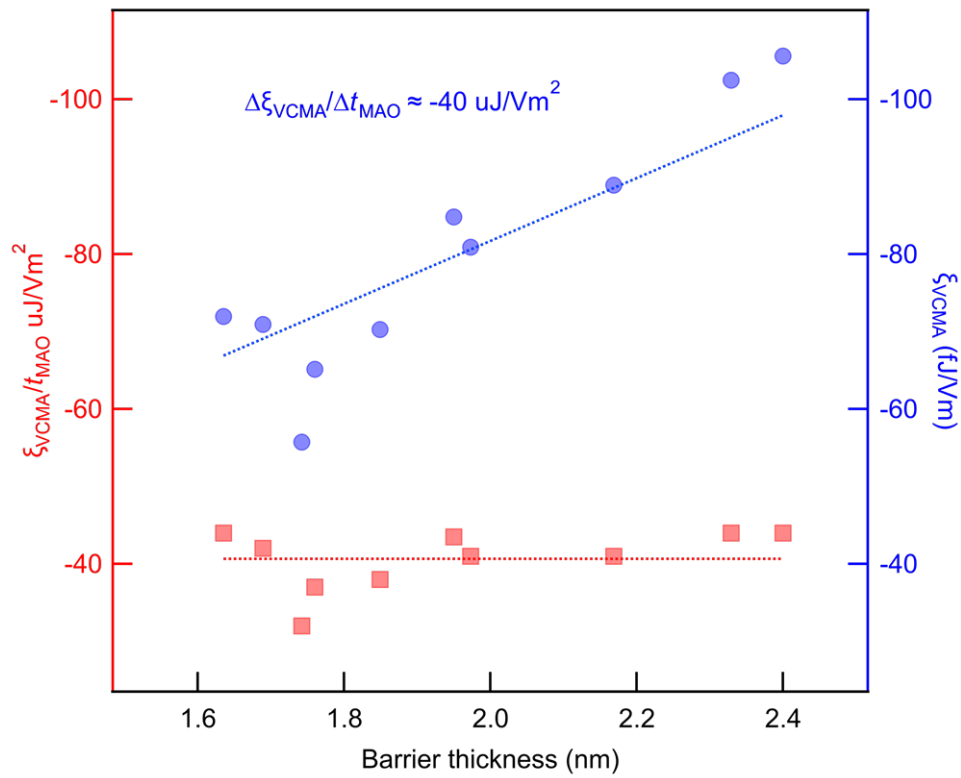
Figure 6.19 VCMA coefficient and VCMA coefficient/$t_{Barrier}$ as a function of $t_{Barrier}$.

6.4   Summary

In this experiment, Cr/ultrathin-Fe/MgAl$_2$O$_4$/Fe(CoB) MTJs are evaluated the VCMA with the existence of QWs in ultrathin-Fe layer. The PMA energy density is evaluated up to 1.4 MJ/m^3 with K_i around 1.86 mJ/m^2. The QWs is confirmed by the conductance spectrum and the VCMA is observe by anomalous modulated by the SDRT effect. The largest VCMA coefficient is up to 390 fJ/Vm. It is believed that the anomalous VCMA originated from the DOS modification near the interface by the SDRT effect. A barrier thickness dependence experiment is performed to confirm the observed VCMA effect is related to the potential rather than electrical field. The anomalous VCMA also provide the possibility to obtain "A" shape VCMA curve, with the resonant state confined near 0 bias, which can realize two direction switches by current only.

Chapter 7   Summary

In development of magnetic memories, PMA, TMR and writing methods are the three major aspects to research with. In this study, the VCMA, which is crucial for next-generation writing technique, is evaluated for a Fe/oxide interface. Meanwhile, the PMA and TMR properties are also investigated as they are the important issues for applications.

1. As Fe/MgO is a typical structure for coherent MTJs, a VCMA evaluation if performed to an epitaxial Cr/Fe/MgO/Fe MTJs. A large interfacial PMA is obtained at the Fe/MgO interface with H_k larger than 2T. Different post-annealing temperatures are performed to the Fe/MgO interface to modify the interface conditions. A clear PMA energy density difference is observed for different annealing temperature, which indicates the interface conditions modified. The largest VCMA coefficient obtained is around -270 fJ/Vm. The most interesting observation is a local minimum around 100 mV, independent from annealing temperatures. Same evaluation is performed for various measurement temperatures with the local minimum survived. It indicated the obtained nonlinear VCMA originated from the electronic structures which independent from the interface conditions.

2. For better understanding the VCMA, a better interface with perfect lattice match is expected to reach the ideal interface used in theoretical calculation. Thus, a $MgAl_2O_4$ is used to replace MgO which has less than 1% lattice mismatch from Fe electrode. Epitaxial Fe/ $MgAl_2O_4$ heterostructures are prepared by direct EB-evaporation. A maximum PMA energy up to 1 MJ/m^3 is obtained for optimized conditions. And the obtained PMA is evaluated for various temperatures which shows only ~15% fluctuance of K_i regarding temperature from 100K to 300K. Meanwhile, a damping constant is evaluated around 0.02.

3. Regarding the ultrathin-Fe sandwiched by Cr and oxide barrier structure, quantum well is supposed established within ultrathin-Fe, attributing spin-dependent resonant tunneling effect to the tunneling process. As the $MgAl_2O_4$ is perfect matching with Fe, a Cr/Fe/$MgAl_2O_4$ can create a perfect quantum well structure as there no dislocations or defects. A significant enhanced TMR is observed due to the SDRT. When the resonant bias locating far from zero bias, the TMR at the position is even higher than zero bias value. Comparing the enhancement of TMR at zero bias with and without resonant, a 1.5 times difference can be observed. A temperature dependence measurement is also performed to prove the Δ_1 transport is confined at the resonant bias, where a reversed TCR is observed for resonant position from non-resonant positions.

4. With large PMA obtained in Fe/$MgAl_2O_4$, and QWs is well established inside Fe layer, an anomalous VCMA is observed. In this experiment, Cr/ultrathin-Fe/$MgAl_2O_4$/Fe(CoB) MTJs are evaluated the VCMA with the existence of QWs in ultrathin-Fe layer. The PMA energy density is evaluated up to 1.4 MJ/m^3 with K_i around 1.86 mJ/m^2. The QWs is confirmed by the conductance spectrum and the VCMA is observe by anomalous modulated by the SDRT effect. The largest VCMA coefficient is up to 390 fJ/Vm. It is believed that the anomalous VCMA originated from the DOS modification near the interface by the SDRT effect. A barrier thickness dependence experiment is performed to confirm the observed VCMA effect is related to the potential rather than electrical field. The anomalous VCMA also provide the possibility to obtain "A" shape VCMA curve, with the resonant state confined near 0 bias, which can realize two direction switches by current only.

Reference

[1]   W. Pauli, Z. Für Phys. 31 (1925) 765–783.

[2]   G.E. Uhlenbeck, S. Goudsmit, Naturwissenschaften 13 (1925) 953–954.

[3]   L.H. Thomas, Nature 117 (1926) 514.

[4]   P.A.M. Dirac, Proc. R. Soc. Math. Phys. Eng. Sci. 117 (1928) 610–624.

[5]   M.N. Baibich, J.M. Broto, A. Fert, F.N. Van Dau, F. Petroff, P. Etienne, G. Creuzet, A. Friederich, J. Chazelas, Phys. Rev. Lett. 61 (1988) 2472–2475.

[6]   G. Binasch, P. Grünberg, F. Saurenbach, W. Zinn, Phys. Rev. B 39 (1989) 4828–4830.

[7]   T. Miyazaki, N. Tezuka, J. Magn. Magn. Mater. 139 (1995) L231–L234.

[8]   J.S. Moodera, L.R. Kinder, T.M. Wong, R. Meservey, Phys. Rev. Lett. 74 (1995) 3273–3276.

[9]   J.C. Slonczewski, J. Magn. Magn. Mater. 159 (1996) L1–L7.

[10]   M. Tsoi, A.G.M. Jansen, J. Bass, W.-C. Chiang, M. Seck, V. Tsoi, P. Wyder, Phys. Rev. Lett. 80 (1998) 4281–4284.

[11]   S. Yuasa, T. Nagahama, A. Fukushima, Y. Suzuki, K. Ando, Nat. Mater. 3 (2004) 868–871.

[12]   S.S.P. Parkin, C. Kaiser, A. Panchula, P.M. Rice, B. Hughes, M. Samant, S.-H. Yang, Nat. Mater. 3 (2004) 862–867.

[13]   Y.K. Kato, R.C. Myers, A.C. Gossard, D.D. Awschalom, Science 306 (2004) 1910–1913.

[14]   K. Uchida, S. Takahashi, K. Harii, J. Ieda, W. Koshibae, K. Ando, S. Maekawa, E. Saitoh, Nature 455 (2008) 778–781.

[15]   T. Maruyama, Y. Shiota, T. Nozaki, K. Ohta, N. Toda, M. Mizuguchi, A.A. Tulapurkar, T. Shinjo, M. Shiraishi, S. Mizukami, Y. Ando, Y. Suzuki, Nat. Nanotechnol. 4 (2009) 158–161.

[16]   S. Ikeda, K. Miura, H. Yamamoto, K. Mizunuma, H.D. Gan, M. Endo, S. Kanai, J. Hayakawa, F. Matsukura, H. Ohno, Nat. Mater. 9 (2010) 721–724.

[17]   L. Liu, C.-F. Pai, Y. Li, H.W. Tseng, D.C. Ralph, R.A. Buhrman, Science 336 (2012) 555–558.

[18]   W. Thomson, Proc. R. Soc. Lond. 8 (1857) 546–550.

[19]   T. McGuire, R. Potter, IEEE Trans. Magn. 11 (1975) 1018–1038.

[20]   N.F. Mott, Proc R Soc Lond A 153 (1936) 699–717.

[21]   P. Grünberg, R. Schreiber, Y. Pang, M.B. Brodsky, H. Sowers, Phys. Rev. Lett. 57 (1986) 2442–2445.

[22]   S.S.P. Parkin, N. More, K.P. Roche, Phys. Rev. Lett. 64 (1990) 2304–2307.

[23]   S.S.P. Parkin, R. Bhadra, K.P. Roche, Phys. Rev. Lett. 66 (1991) 2152–2155.

[24]   B. Dieny, V.S. Speriosu, S.S.P. Parkin, B.A. Gurney, D.R. Wilhoit, D. Mauri, Phys. Rev. B 43 (1991) 1297–1300.

[25]   M. Julliere, Phys. Lett. A 54 (1975) 225–226.

[26]   E.Y. Tsymbal, I. Zutic, Handbook of Spin Transport and Magnetism, CRC press, 2011.

[27]   T. Miyazaki, T. Yaoi, S. Ishio, J. Magn. Magn. Mater. 98 (1991) L7–L9.

[28]   T. Miyazaki, N. Tezuka, J. Magn. Magn. Mater. 139 (1995) L231–L234.

[29]   D. Wang, C. Nordman, J.M. Daughton, Z. Qian, J. Fink, IEEE Trans. Magn. 40 (2004) 2269–2271.

[30] W.H. Butler, X.-G. Zhang, T.C. Schulthess, J.M. MacLaren, Phys. Rev. B 63 (2001) 054416.

[31] X. Zhang, W. Butler, in: Y. Xu, D.D. Awschalom, J. Nitta (Eds.), Handb. Spintron., Springer Netherlands, Dordrecht, 2016, pp. 3–69.

[32] D.D. Djayaprawira, K. Tsunekawa, M. Nagai, H. Maehara, S. Yamagata, N. Watanabe, S. Yuasa, Y. Suzuki, K. Ando, Appl. Phys. Lett. 86 (2005) 092502.

[33] S. Ikeda, J. Hayakawa, Y. Ashizawa, Y.M. Lee, K. Miura, H. Hasegawa, M. Tsunoda, F. Matsukura, H. Ohno, Appl. Phys. Lett. 93 (2008) 082508.

[34] Y. Miura, S. Muramoto, K. Abe, M. Shirai, Phys. Rev. B 86 (2012) 024426.

[35] J. Zhang, X.-G. Zhang, X.F. Han, Appl. Phys. Lett. 100 (2012) 222401.

[36] H. Sukegawa, H. Xiu, T. Ohkubo, T. Furubayashi, T. Niizeki, W. Wang, S. Kasai, S. Mitani, K. Inomata, K. Hono, Appl. Phys. Lett. 96 (2010) 212505.

[37] T. Nozaki, N. Tezuka, K. Inomata, Phys. Rev. Lett. 96 (2006).

[38] A. Iovan, S. Andersson, Y.G. Naidyuk, A. Vedyaev, B. Dieny, V. Korenivski, Nano Lett. 8 (2008) 805–809.

[39] T. Niizeki, N. Tezuka, K. Inomata, Phys. Rev. Lett. 100 (2008) 047207.

[40] Z.-Y. Lu, X.-G. Zhang, S.T. Pantelides, Phys. Rev. Lett. 94 (2005) 207210.

[41] F. Greullet, C. Tiusan, F. Montaigne, M. Hehn, D. Halley, O. Bengone, M. Bowen, W. Weber, Phys. Rev. Lett. 99 (2007) 187202.

[42] T. Nagahama, S. Yuasa, Y. Suzuki, E. Tamura, Appl. Phys. Lett. 79 (2001) 4381–4383.

[43] P. Sheng, F. Bonell, S. Miwa, T. Nakamura, Y. Shiota, S. Murakami, D.D. Lam, S. Yoshida, Y. Suzuki, Appl. Phys. Lett. 102 (2013) 032406.

[44] J.M.D. Coey, Magnetism and Magnetic Materials, Cambridge University Press, Cambridge, 2010.

[45] L. Néel, J. Phys. Radium 15 (1954) 225–239.

[46] U. Gradmann, J. Müller, Phys. Status Solidi B 27 (1968) 313–324.

[47] M.T. Johnson, P.J.H. Bloemen, F.J.A. den Broeder, J.J. de Vries, Rep. Prog. Phys. 59 (1996) 1409–1458.

[48] F.J.A. den Broeder, W. Hoving, P.J.H. Bloemen, J. Magn. Magn. Mater. 93 (1991) 562–570.

[49] S. Monso, B. Rodmacq, S. Auffret, G. Casali, F. Fettar, B. Gilles, B. Dieny, P. Boyer, Appl. Phys. Lett. 80 (2002) 4157–4159.

[50] A. Manchon, C. Ducruet, L. Lombard, S. Auffret, B. Rodmacq, B. Dieny, S. Pizzini, J. Vogel, V. Uhlíř, M. Hochstrasser, G. Panaccione, J. Appl. Phys. 104 (2008) 043914.

[51] J.W. Koo, S. Mitani, T.T. Sasaki, H. Sukegawa, Z.C. Wen, T. Ohkubo, T. Niizeki, K. Inomata, K. Hono, Appl. Phys. Lett. 103 (2013) 192401.

[52] H.X. Yang, M. Chshiev, B. Dieny, J.H. Lee, A. Manchon, K.H. Shin, Phys. Rev. B 84 (2011) 054401.

[53] W. Jones, N.H. March, Perfect Lattices in Equilibrium, Wiley-Interscience, London, New York, 1973.

[54] A.V. Khvalkovskiy, D. Apalkov, S. Watts, R. Chepulskii, R.S. Beach, A. Ong, X. Tang, A. Driskill-Smith, W.H. Butler, P.B. Visscher, D. Lottis, E. Chen, V. Nikitin, M. Krounbi, J. Phys. Appl. Phys. 46 (2013) 074001.

[55] S. Methfessel, IEEE Trans. Magn. 1 (1965) 144–155.

[56] M. Weisheit, S. Fähler, A. Marty, Y. Souche, C. Poinsignon, D. Givord, Science 315 (2007)

349–351.

[57]   Y. Shiota, T. Nozaki, F. Bonell, S. Murakami, T. Shinjo, Y. Suzuki, Nat. Mater. 11 (2012) 39–43.

[58]   W.-G. Wang, M. Li, S. Hageman, C.L. Chien, Nat. Mater. 11 (2012) 64–68.

[59]   Y. Shiota, T. Maruyama, T. Nozaki, T. Shinjo, M. Shiraishi, Y. Suzuki, Appl. Phys. Express 2 (2009) 063001.

[60]   S. Kanai, Y. Nakatani, M. Yamanouchi, S. Ikeda, H. Sato, F. Matsukura, H. Ohno, Appl. Phys. Lett. 104 (2014) 212406.

[61]   H. Yoda, N. Shimomura, Y. Ohsawa, S. Shirotori, Y. Kato, T. Inokuchi, Y. Kamiguchi, B. Altansargai, Y. Saito, K. Koi, H. Sugiyama, S. Oikawa, M. Shimizu, M. Ishikawa, K. Ikegami, A. Kurobe, in: IEEE, 2016, pp. 27.6.1-27.6.4.

[62]   Y. Shiota, S. Murakami, F. Bonell, T. Nozaki, T. Shinjo, Y. Suzuki, Appl. Phys. Express 4 (2011) 043005.

[63]   Wikipedia (2017).

[64]   M. Ohring, Materials Science of Thin Films Deposition and Structure, Elsevier, Amsterdam, 2002.

[65]   Quantum Des. Website (n.d.).

[66]   S.-S. Ha, N.-H. Kim, S. Lee, C.-Y. You, Y. Shiota, T. Maruyama, T. Nozaki, Y. Suzuki, Appl. Phys. Lett. 96 (2010) 142512.

[67]   T. Zhou, S.H. Leong, Z.M. Yuan, S.B. Hu, C.L. Ong, B. Liu, Appl. Phys. Lett. 96 (2010) 012506.

[68]   M. Endo, S. Kanai, S. Ikeda, F. Matsukura, H. Ohno, Appl. Phys. Lett. 96 (2010) 212503.

[69]   F. Bonell, S. Murakami, Y. Shiota, T. Nozaki, T. Shinjo, Y. Suzuki, Appl. Phys. Lett. 98 (2011) 232510.

[70]   T. Seki, M. Kohda, J. Nitta, K. Takanashi, Appl. Phys. Lett. 98 (2011) 212505.

[71]   K. Kita, D.W. Abraham, M.J. Gajek, D.C. Worledge, J. Appl. Phys. 112 (2012) 033919.

[72]   T. Nozaki, Y. Shiota, M. Shiraishi, T. Shinjo, Y. Suzuki, Appl. Phys. Lett. 96 (2010) 022506.

[73]   W. Skowroński, P. Wiśniowski, T. Stobiecki, S. Cardoso, P.P. Freitas, S. van Dijken, Appl. Phys. Lett. 101 (2012) 192401.

[74]   P.K. Amiri, P. Upadhyaya, J.G. Alzate, K.L. Wang, J. Appl. Phys. 113 (2013) 013912.

[75]   A. Rajanikanth, T. Hauet, F. Montaigne, S. Mangin, S. Andrieu, Appl. Phys. Lett. 103 (2013) 062402.

[76]   Y. Shiota, F. Bonell, S. Miwa, N. Mizuochi, T. Shinjo, Y. Suzuki, Appl. Phys. Lett. 103 (2013) 082410.

[77]   T. Nozaki, K. Yakushiji, S. Tamaru, M. Sekine, R. Matsumoto, M. Konoto, H. Kubota, A. Fukushima, S. Yuasa, Appl. Phys. Express 6 (2013) 073005.

[78]   T. Nozaki, H. Arai, K. Yakushiji, S. Tamaru, H. Kubota, H. Imamura, A. Fukushima, S. Yuasa, Appl. Phys. Express 7 (2014) 073002.

[79]   J.G. Alzate, P. Khalili Amiri, G. Yu, P. Upadhyaya, J.A. Katine, J. Langer, B. Ocker, I.N. Krivorotov, K.L. Wang, Appl. Phys. Lett. 104 (2014) 112410.

[80]   V.B. Naik, H. Meng, J.X. Xiao, R.S. Liu, A. Kumar, K.Y. Zeng, P. Luo, S. Yap, Appl. Phys. Lett. 105 (2014) 052403.

[81]   A. Sonntag, J. Hermenau, A. Schlenhoff, J. Friedlein, S. Krause, R. Wiesendanger, Phys. Rev. Lett. 112 (2014).

[82]   W. Skowroński, T. Nozaki, D.D. Lam, Y. Shiota, K. Yakushiji, H. Kubota, A. Fukushima, S. Yuasa, Y. Suzuki, Phys. Rev. B 91 (2015).

[83]   W. Skowroński, T. Nozaki, Y. Shiota, S. Tamaru, K. Yakushiji, H. Kubota, A. Fukushima, S. Yuasa, Y. Suzuki, Appl. Phys. Express 8 (2015) 053003.

[84]   T. Nozaki, A. Kozioł-Rachwał, W. Skowroński, V. Zayets, Y. Shiota, S. Tamaru, H. Kubota, A. Fukushima, S. Yuasa, Y. Suzuki, Phys. Rev. Appl. 5 (2016) 044006.

[85]   T. Nozaki, Y. Shiota, S. Miwa, S. Murakami, F. Bonell, S. Ishibashi, H. Kubota, K. Yakushiji, T. Saruya, A. Fukushima, S. Yuasa, T. Shinjo, Y. Suzuki, Nat. Phys. 8 (2012) 492–497.

[86]   J. Zhu, J.A. Katine, G.E. Rowlands, Y.-J. Chen, Z. Duan, J.G. Alzate, P. Upadhyaya, J. Langer, P.K. Amiri, K.L. Wang, I.N. Krivorotov, Phys. Rev. Lett. 108 (2012) 197203.

[87]   Q. Xiang, Z. Wen, H. Sukegawa, S. Kasai, T. Seki, T. Kubota, Koki Takanashi, S. Mitani, J. Phys. Appl. Phys. 50 (2017) 40LT04.

[88]   K. Nakamura, R. Shimabukuro, Y. Fujiwara, T. Akiyama, T. Ito, A.J. Freeman, Phys. Rev. Lett. 102 (2009) 187201.

[89]   C.-H. Lambert, A. Rajanikanth, T. Hauet, S. Mangin, E.E. Fullerton, S. Andrieu, Appl. Phys. Lett. 102 (2013) 122410.

[90]   M. Tsujikawa, T. Oda, Phys. Rev. Lett. 102 (2009) 247203.

[91]   K.D. Belashchenko, J. Velev, E.Y. Tsymbal, Phys. Rev. B 72 (2005) 140404.

[92]   D. Yoshikawa, M. Obata, Y. Taguchi, S. Haraguchi, T. Oda, Appl. Phys. Express 7 (2014) 113005.

[93]   H. Sukegawa, Y. Miura, S. Muramoto, S. Mitani, T. Niizeki, T. Ohkubo, K. Abe, M. Shirai, K. Inomata, K. Hono, Phys. Rev. B 86 (2012) 184401.

[94]   T. Scheike, H. Sukegawa, K. Inomata, T. Ohkubo, K. Hono, S. Mitani, Appl. Phys. Express 9 (2016) 053004.

[95]   M. Belmoubarik, H. Sukegawa, T. Ohkubo, S. Mitani, K. Hono, Appl. Phys. Lett. 108 (2016) 132404.

[96]   T. Seki, S. Mitani, K. Yakushiji, K. Takanashi, Appl. Phys. Lett. 89 (2006) 172504.

[97]   J. Koo, H. Sukegawa, S. Mitani, Phys. Status Solidi RRL – Rapid Res. Lett. 8 (2014) 841–844.

[98]   H. Sukegawa, J.P. Hadorn, Z. Wen, T. Ohkubo, S. Mitani, K. Hono, Appl. Phys. Lett. 110 (2017) 112403.

[99]   K. Masuda, Y. Miura, ArXiv180310428 Cond-Mat (2018).

[100]   K. Lee, S.H. Kang, IEEE Trans. Magn. 46 (2010) 1537–1540.

[101]   Jian-Gang Zhu, Proc. IEEE 96 (2008) 1786–1798.

[102]   B.S. Tao, H.X. Yang, Y.L. Zuo, X. Devaux, G. Lengaigne, M. Hehn, D. Lacour, S. Andrieu, M. Chshiev, T. Hauet, F. Montaigne, S. Mangin, X.F. Han, Y. Lu, Phys. Rev. Lett. 115 (2015) 157204.

[103]   Y. Fukumoto, H. Numata, K. Suemitsu, K. Nagahara, N. Ohshima, M. Amano, Y. Asao, H. Hada, H. Yoda, S. Tahara, Jpn. J. Appl. Phys. 45 (2006) 3829.

[104]   N.W. Ashcroft, N.D. Mermin, Solid State Physics., Saunders college, Philadelphia, Pa., 1976.

[105]   Z.Q. Qiu, J. Pearson, S.D. Bader, Phys. Rev. Lett. 70 (1993) 1006–1009.

[106]   L.H. Tjeng, Y.U. Idzerda, P. Rudolf, F. Sette, C.T. Chen, J. Magn. Magn. Mater. 109 (1992) 288–292.

[107]   C.M. Schneider, P. Bressler, P. Schuster, J. Kirschner, J.J. de Miguel, R. Miranda, Phys. Rev. Lett. 64 (1990) 1059–1062.

[108] A. Okada, S. He, B. Gu, S. Kanai, A. Soumyanarayanan, S.T. Lim, M. Tran, M. Mori, S. Maekawa, F. Matsukura, H. Ohno, C. Panagopoulos, Proc. Natl. Acad. Sci. 114 (2017) 3815–3820.

[109] H.B. Callen, E. Callen, J. Phys. Chem. Solids 27 (1966) 1271–1285.

[110] J.B. Staunton, S. Ostanin, S.S.A. Razee, B.L. Gyorffy, L. Szunyogh, B. Ginatempo, E. Bruno, Phys. Rev. Lett. 93 (2004) 257204.

[111] R. Skomski, O.N. Mryasov, J. Zhou, D.J. Sellmyer, J. Appl. Phys. 99 (2006) 08E916.

[112] J.B. Staunton, L. Szunyogh, A. Buruzs, B.L. Gyorffy, S. Ostanin, L. Udvardi, Phys. Rev. B 74 (2006) 144411.

[113] Á. Buruzs, P. Weinberger, L. Szunyogh, L. Udvardi, P.I. Chleboun, A.M. Fischer, J.B. Staunton, Phys. Rev. B 76 (2007) 064417.

[114] S. Okamoto, N. Kikuchi, O. Kitakami, T. Miyazaki, Y. Shimada, K. Fukamichi, Phys. Rev. B 66 (2002) 024413.

[115] S. Mizukami, S. Iihama, Y. Sasaki, A. Sugihara, R. Ranjbar, K.Z. Suzuki, J. Appl. Phys. 120 (2016) 142102.

[116] A. Sakuma, J. Phys. Appl. Phys. 48 (2015) 164011.

[117] P. Bruno, Phys. Rev. B 39 (1989) 865–868.

[118] Y.K. Takahashi, Y. Miura, R. Choi, T. Ohkubo, Z.C. Wen, K. Ishioka, R. Mandal, R. Medapalli, H. Sukegawa, S. Mitani, E.E. Fullerton, K. Hono, Appl. Phys. Lett. 110 (2017) 252409.

[119] S. Mizukami, S. Iihama, N. Inami, T. Hiratsuka, G. Kim, H. Naganuma, M. Oogane, Y. Ando, Appl. Phys. Lett. 98 (2011) 052501.

[120] E. Barati, M. Cinal, D.M. Edwards, A. Umerski, Phys Rev B 90 (2014) 014420.

[121] B. Heinrich, K.B. Urquhart, A.S. Arrott, J.F. Cochran, K. Myrtle, S.T. Purcell, Phys. Rev. Lett. 59 (1987) 1756–1759.

[122] S.A. Wolf, D.D. Awschalom, R.A. Buhrman, J.M. Daughton, S. Von Molnar, M.L. Roukes, A.Y. Chtchelkanova, D.M. Treger, Science 294 (2001) 1488–1495.

[123] C. Chappert, A. Fert, F.N. Van Dau, Nat. Mater. 6 (2007) 813–823.

[124] J. Camarero, T. Graf, J.J. de Miguel, R. Miranda, W. Kuch, M. Zharnikov, A. Dittschar, C.M. Schneider, J. Kirschner, Phys. Rev. Lett. 76 (1996) 4428–4431.

[125] S. Yuasa, T. Nagahama, Y. Suzuki, Science 297 (2002) 234–237.

[126] Y. Wang, Z.-Y. Lu, X.-G. Zhang, X.F. Han, Phys. Rev. Lett. 97 (2006) 087210.

[127] D. Bang, T. Nozaki, Y. Suzuki, J. Appl. Phys. 109 (2011) 07C719.

[128] P. Sheng, D. Bang, T. Nozaki, S. Miwa, Y. Suzuki, Solid State Commun. 152 (2012) 273–277.

[129] R.S. Liu, S.-H. Yang, X. Jiang, X.-G. Zhang, C. Rettner, L. Gao, T. Topuria, P.M. Rice, W. Zhang, C.M. Canali, S.S.P. Parkin, Phys. Rev. B 87 (2013) 024411.

[130] N. Tezuka, S. Oikawa, I. Abe, M. Matsuura, S. Sugimoto, K. Nishimura, T. Seino, IEEE Magn. Lett. 7 (2016) 1–4.

[131] Q. Xiang, R. Mandal, H. Sukegawa, Y.K. Takahashi, S. Mitani, Appl. Phys. Express 11 (2018) 063008.

[132] J.C. Slonczewski, Phys. Rev. B 39 (1989) 6995–7002.

[133] S. Zhang, P.M. Levy, A.C. Marley, S.S.P. Parkin, Phys. Rev. Lett. 79 (1997) 3744–3747.

[134] C.H. Shang, J. Nowak, R. Jansen, J.S. Moodera, Phys. Rev. B 58 (1998) R2917.

[135] B. Hu, K. Moges, Y. Honda, H. Liu, T. Uemura, M. Yamamoto, J. Inoue, M. Shirai, Phys. Rev. B 94 (2016).

[136] K. Nakamura, T. Akiyama, T. Ito, M. Weinert, A.J. Freeman, Phys. Rev. B 81 (2010).

[137] A. Kozioł-Rachwał, T. Nozaki, K. Freindl, J. Korecki, S. Yuasa, Y. Suzuki, Sci. Rep. 7 (2017) 5993.

[138] X. Li, K. Fitzell, D. Wu, C.T. Karaba, A. Buditama, G. Yu, K.L. Wong, N. Altieri, C. Grezes, N. Kioussis, S. Tolbert, Z. Zhang, J.P. Chang, P. Khalili Amiri, K.L. Wang, Appl. Phys. Lett. 110 (2017) 052401.

[139] T. Nozaki, A. Kozioł-Rachwał, M. Tsujikawa, Y. Shiota, X. Xu, T. Ohkubo, T. Tsukahara, S. Miwa, M. Suzuki, S. Tamaru, H. Kubota, A. Fukushima, K. Hono, M. Shirai, Y. Suzuki, S. Yuasa, NPG Asia Mater. 9 (2017) e451.

Appendix　Table of figures

Achievements

Publications:

Q. Xiang, Z. Wen, H. Sukegawa, S. Kasai, T. Seki, T. Kubota, K. Takanashi and S. Mitani
Nonlinear electric field effect on perpendicular magnetic anisotropy in Fe/MgO interfaces,
J. Phys. D: Appl. Phys. 50 40LT04, 2017

Q. Xiang, R. Mandal, H. Sukegawa, Y. Takahashi and S. Mitani
Large perpendicular magnetic anisotropy in epitaxial Fe/MgAl$_2$O$_4$(001) heterostructures
Appl. Phys. Express 11 063008, 2018

Q. Xiang, H. Sukegawa, M. Belmoubarik, M. Al-Mahdawi, T. Scheike, S. Kasai, Y. Miura and S. Mitani
Enhanced tunnel magnetoresistance via quantum well states in Cr/Fe/MgAl2O4/Fe(001) junctions
Submitted.

Q. Xiang, Z. Wen, M. Al-Mahdawi, M. Belmoubarik, S. Kasai, Y. Sakuraba, H. Sukegawa, S. Mitani and K. Hono
Voltage-controlled magnetic anisotropy in quantum wells
in preparation

M. Al-Mahdawi, Q. Xiang, M. Belmoubarik, K. Masuda, H. Sukegawa, Y. Miura, S. Mitani
Controlled enhancement of tunneling anisotropic magnetoresistance in spin-dependent metallic quantum wells of Cr/Fe/MgAl$_2$O$_4$
in preparation

Awards:

JSAP Young Scientist Presentation Award
65th JSAP Spring Meeting, 2018

English Presentation Award of JSAP's Professional Group of Spintoronics
65th JSAP Spring Meeting, 2018

Best Poster Award
3rd ImPACT International Symposium on Spintronic Memory, Circuit and Storage Award

Invited talk

Q. Xiang, H. Sukegawa, M. Al-Mahdawi, M. Belmoubarik, S. Kasai, Y. Sakuraba, S. Mitani and K. Hono

Voltage control of perpendicular magnetic anisotropy in Fe/MgAl2O4 heterostructures
The 65th JSAP Spring Meeting, Tokyo, Japan, Mar.2018

S. Mitani, Q. Xiang, J. Koo, Z. Wen, H. Sukegawa
Interface perpendicular magnetic anisotropy in ferromagnetic metal/oxide heterostructures and magnetic tunnel junctions
The 14th IUMRS-ICAM, Jeju, Korea, Oct.2016

Oral and poster presentation

Q. Xiang, H. Sukegawa, M. Al-Mahdawi, M. Belmoubarik, S. Kasai, Y. Sakuraba, S. Mitani and K. Hono
Atomic layer number dependence of voltage-controlled magnetic anisotropy in $Cr/Fe/MgAl_2O_4$ heterostructure
Intermag 2018, Singapore, Apr.2018

Q. Xiang, M. Al-Mahdawi, H. Sukegawa, M. Belmoubarik, S. Kasai, Y. Sakuraba, S. Mitani and K. Hono
Perpendicular magnetic anisotropy at $Fe/MgAl_2O_4$ interfaces and its voltage effect
The 41st Annual Conference on MAGNETICS in Japan, Fukuoka, Japan, Sep.2017

Q. Xiang, H. Sukegawa, M. Al-Mahdawi, M. Belmoubarik, S. Kasai, Y. Sakuraba, S. Mitani and K. Hono
Voltage control of Perpendicular magnetic anisotropy in Fe/MgAl2O4 heterostructures
The 78th JSAP Autumn Meeting 2017, Fukuoka, Japan, Sep.2017

Q. Xiang, H. Sukegawa, S. Kasai,and S. Mitani
Perpendicular magnetic anisotropy and its electric field effect in Fe/Mg-based oxide interfaces
The 77th JSAP Autumn Meeting 2017, Niikata, Japan, Sep.2016

Q. Xiang, H. Sukegawa, M. Al-Mahdawi, M. Belmoubarik, S. Kasai, Y. Sakuraba, S. Mitani and K. Hono
Voltage control of perpendicular magnetic anisotropy in Fe/MgAl2O4 heterostructures: significant effect of the Fe atomic layer numbers
The 3rd ImPACT International Symposium on Spintronic Memory, Circuit and Storage, Sendai, Japan, Sep.2017

Q. Xiang, Z. Wen, H. Sukegawa, S. Kasai, T. Seki, T. Kubota, K. Takanashi and S. Mitani
Specific nonlinearity of voltage controlled magnetic anisotropy in Fe/MgO layered structures
The 28th Magnetic Recording Conference, Tsukuba, Japan, Sep.2017
Q. Xiang, H. Sukegawa, S. Kasai and S. Mitani
Electric field effect on perpendicular magnetic anisotropy in Fe/MgO interfaces annealed at different temperatures
The 61st Annual Conference on Magnetism and Magnetic Materials, New Orleans, USA, Oct. 2016